# Photo-magnonics in two-dimensional antidot lattices

## Dissertation

zur Erlangung des mathematisch-naturwissenschaftlichen Doktorgrades
„Doctor rerum naturalium”
der Georg-August-Universität Göttingen
—
im Promotionsprogramm ProPhys
der Georg-August University School of Science (GAUSS)

vorgelegt von

**Benjamin Lenk**

aus Ilmenau

Göttingen, 2012

**Betreuungsausschuss:**
Prof. Dr. Markus Münzenberg, I. Physikalisches Institut
Prof. Dr. Christian Jooss, Institut für Materialphysik

**Mitglieder der Prüfungskommision:**

| | |
|---|---|
| Referent: | Prof. Dr. Markus Münzenberg, I. Physikalisches Institut |
| Korreferent: | Prof. Dr. Christian Jooss, Institut für Materialphysik |

**weitere Mitglieder der Prüfungskommission:**
Prof. Dr. Stefan Kehrein, Institut für Theoretische Physik
Prof. Dr. Hans-Ulrich Krebs, Institut für Materialphysik
Prof. Dr. Angela Rizzi, IV. Physikalisches Institut
Prof. Dr. Claus Ropers, Institut für Materialphysik

**Tag der mündlichen Prüfung: 12. Dezember 2012**

# Contents

1 **General introduction** **1**
Spin waves and magnons . . . . . . . . . . . . . . . . . . . . . . . . . 1
Manipulating waves with metamaterials . . . . . . . . . . . . . . . . 4
Magnonic crystals . . . . . . . . . . . . . . . . . . . . . . . . . . . 5

2 **Spin-wave population in nickel after femtosecond laser pulse excitation** **9**
2.1 Introduction . . . . . . . . . . . . . . . . . . . . . . . . . . 9
2.2 Experiment . . . . . . . . . . . . . . . . . . . . . . . . . . 12
2.3 Results and discussion . . . . . . . . . . . . . . . . . . . . 13
2.4 Conclusion . . . . . . . . . . . . . . . . . . . . . . . . . . . 20

3 **The building blocks of magnonics** **23**
3.1 Introduction . . . . . . . . . . . . . . . . . . . . . . . . . . 23
3.2 Computing with spin waves . . . . . . . . . . . . . . . . . . 25
3.2.1 What are spin-wave guides? . . . . . . . . . . . . . . . . 26
3.2.2 Spin waves on a chip: Reconfigurable mesh design . . . . . 28
3.2.3 Elements of spin-wave computing and logic . . . . . . . . . 29
3.3 Tailoring artificial materials . . . . . . . . . . . . . . . . . . 31
3.3.1 Bloch conditions and band structure: weak periodic potential 33
3.3.2 Electrons in a strong periodic potential . . . . . . . . . . . 34
3.3.3 Photonic crystals – photons in periodic potentials . . . . . 35
3.3.4 Novel functionalities of photonic crystals: slow photons . . 37
3.4 Magnonic crystals – spin waves in periodic potentials . . . . . . . 38
3.4.1 Spin-wave dispersion from nanometer to micron range . . . 38
3.4.2 Band structures of magnonic crystals . . . . . . . . . . . . 41
3.4.3 Periodic dipolar potential in structured films: micromagnetic simulations . . . . . . . . . . . . . . . . . . . . . . . . 47

    3.4.4 Micron and nanometer structuring for static and active magnonic crystals . . . 50
  3.5 Experiments with magnonic structures . . . 51
    3.5.1 Techniques . . . 52
    3.5.2 Localization effects in magnonic crystals . . . 60
    3.5.3 Bloch modes in magnonic crystals . . . 68
    3.5.4 Magnonic wave guides . . . 71
  3.6 Outlook: controlled spin-wave localization . . . 73

**4 Spin-wave modes and band structure of rectangular CoFeB antidot lattices 75**
  4.1 Introduction . . . 75
  4.2 Simulations . . . 76
  4.3 Experiments . . . 77
  4.4 Discussion and conclusions . . . 80

**5 General discussion 81**

**Bibliography 83**

**A Supplemental material of PRB 82, 134443 (2010) 97**
  A.1 Time-resolved data . . . 97
  A.2 Angle of the external field . . . 97
  A.3 Hysteresis . . . 98

**B Photo-magnonics 101**
  B.1 Introduction . . . 101
    B.1.1 Spin-wave modes in a thin ferromagnetic film . . . 102
  B.2 Samples and experiments . . . 103
    B.2.1 Thin-film magnetization dynamics . . . 104
  B.3 Bloch-like modes in CoFeB antidot lattices . . . 105
    B.3.1 Effects of antidot-lattice symmetry . . . 107
  B.4 Spin-wave spectra from plane-wave calculations . . . 108
  B.5 Localized modes in nickel antidot lattices . . . 109
  B.6 Outlook: Magnonic control over spin waves . . . 111

**C FIB preparation 113**
  Software for streamfile creation . . . 115

# List of Figures

1.1 Spin-wave schematic . . . . . . . . . . . . . . . . . . . . . . . . 3
1.2 Manipulation of waves with metamaterials . . . . . . . . . . . . 5

2.1 TRMOKE measurement and scheme of spin-wave modes . . . . . 10
2.2 Spin-wave power spectra of thin nickel films with $t = 80\text{-}180\,\mathrm{nm}$ . 14
2.3 Spin-wave modes at $\mu_0 H_{\mathrm{ext}} = 50\,\mathrm{mT}$ for varying thickness $t$ . . . . 16
2.4 Fourier linewidths and Damon-Eshbach wave vector . . . . . . . . 18
2.5 Fourier power spectra of Nickel for different pumping fluences $F = 5\text{-}70\,\mathrm{mJ\,cm^{-2}}$ with $t = 150\,\mathrm{nm}$ . . . . . . . . . . . . . . . . . . . . 19
2.6 Threshold behavior of the Fourier power $A^2_{\Delta\theta,\mathrm{Kittel}}$ of the Kittel mode 21

3.1 Comparison of optical and magnetic wave guides . . . . . . . . . . 27
3.2 Concepts and first realization of spin-wave based computation . . 29
3.3 CMOS technology scaling versus spin-wave based magnetic circuits 31
3.4 Schematic analogy of electrons, photons, and magnons in periodic potentials . . . . . . . . . . . . . . . . . . . . . . . . . . . . . 32
3.5 Electron band structures . . . . . . . . . . . . . . . . . . . . . . 34
3.6 Canonical tight binding $d$-band structure for fcc and bcc lattice along the main symmetry directions . . . . . . . . . . . . . . . . . 35
3.7 Photonic band structure calculated for an array of two-dimensional Al columns . . . . . . . . . . . . . . . . . . . . . . . . . . . . . 37
3.8 Photons entering a wave guide . . . . . . . . . . . . . . . . . . . . 38
3.9 Schematic spin-wave dispersion . . . . . . . . . . . . . . . . . . . 40
3.10 Schematic spin-wave dispersion for different length scales in the periodic zone scheme . . . . . . . . . . . . . . . . . . . . . . . . . 42
3.11 Band structure calculation for a CoFeB film for a two-dimensional square lattice . . . . . . . . . . . . . . . . . . . . . . . . . . . . . 47
3.12 Distribution of the spin-wave amplitudes at the point of high symmetry $X$, $X'$ and $M$ . . . . . . . . . . . . . . . . . . . . . . . . 48

3.13 Band structure calculation for a Ni film for a two-dimensional square lattice . . . 49
3.14 Calculation of the total internal field for a square (left) and a hexagonal (right) antidot structure . . . 50
3.15 Magnetic periodic structures on different length scales and by different methods . . . 52
3.16 Time-resolved wave-guide techniques: pulse-inductive microwave magnetometer (PIMM) . . . 54
3.17 Time and spatially resolved MOKE . . . 55
3.18 BLS setup with high spatial resolution . . . 56
3.19 Time-resolved pump-probe setup . . . 57
3.20 Spin-wave relaxation in all-optical experiments after laser excitation 59
3.21 Effect of an antidot lattice structure measured by all-optical spin-wave excitation and detection . . . 61
3.22 Spatially resolved Fourier power of resonant modes . . . 62
3.23 Effect of acoustic phonons . . . 63
3.24 Effect of the antidot lattice geometry measured by all-optical spin-wave excitation and detection . . . 64
3.25 Internal field and spin-wave localization . . . 65
3.26 Effect of the antidot lattice geometry measured by all-optical spin-wave excitation and detection . . . 66
3.27 Effect of the form factor in elliptical hole structures in a square lattice 67
3.28 Micromagnetic simulation of a one-dimensional magnonic crystal: Py stripe with alternating width . . . 68
3.29 Experimentally measured transmission of a one-dimensional magnonic crystal: Py stripe with alternating width . . . 69
3.30 Bloch modes in a CoFeB antidot lattice . . . 70
3.31 Dominant Bloch modes under 45° . . . 71
3.32 Spin-wave caustics . . . 72
3.33 Magnonic spin-wave guide . . . 73

4.1 Uniform mode analysis in rectangular antidot lattices . . . 77
4.2 Numerically calculated band structures for rectangular magnonic crystals in a CoFeB matrix . . . 78
4.3 Experiments on magnonic spin-wave modes in rectangular antidot lattices . . . 79

A.1 Time-resolved pump-induced change of the Kerr rotation at $t = 100\,\mathrm{nm}$ . . . 98

A.2 Influence of the canting angle of the external field . . . . . . . . . . 99
A.3 Hysteresis . . . . . . . . . . . . . . . . . . . . . . . . . . . . . . . 99

B.1 Experiment and reference data . . . . . . . . . . . . . . . . . . . . . 104
B.2 Fourier analysis of the time-resolved magnetization dynamics of a continuous CoFeB film . . . . . . . . . . . . . . . . . . . . . . . . . 105
B.3 Magnetization dynamics on structured CoFeB films . . . . . . . . . 106
B.4 Numerically calculated spin-wave band structures . . . . . . . . . . 109
B.5 Magnetization dynamics on a structured nickel film with $a = 3.5\,\mu\mathrm{m}$ and $d = 1\,\mu\mathrm{m}$ . . . . . . . . . . . . . . . . . . . . . . . . . . . . . 110

C.2 Singular (anti-)dot examples . . . . . . . . . . . . . . . . . . . . . . 114
C.3 Example lattices . . . . . . . . . . . . . . . . . . . . . . . . . . . . 115
C.4 Screenshot of LabVIEW program for streamfile creation . . . . . . . 116

## Chapter 1

# General introduction

Scientific understanding of dynamic phenomena in general and waves in particular forms the basis of numerous of today's technologies. Since Gauss and Weber have worked on the first transmission of information by electric signals, telecommunication through copper wires has evolved to GHz-frequencies. In parallel, the use of electro-magnetic radiation in wireless devices and fibre optical networks have been established. Together, these technologies for information *transfer* constitute the backbone of our handling of information: fast access from everywhere to the exponentially growing amount of data.

While the permanent *storage* of information remains unchanged in form of magnetic domains either on tape or hard disk drive, by contrast, information *processing* up to now relies on the electron charge. Hence, a combination of magnetic storage and magnetic processing may greatly increase the computational throughput in information technology. Even more so when considering the proximity of respective time scales: read/write cycles in hard disc drives have reached the sub-nanosecond regime and typical magnetic excitation frequencies account to several GHz.

In general, a thorough knowledge of the magnetic dynamic analogue to electrons is required, namely quasi-particle excitations in form of spin waves. The control over their properties in terms of frequency and wave vector is the basis for purely magnetism-based computing. The present (cumulative) thesis points out ways to the control over spin waves. Three peer-reviewed publications by the author are reprinted in the chapters 2–4, and in the following, the underlying physical concepts are introduced.

## Spin waves and magnons

Depending on the characteristic length scale, magnetization dynamics and their quanta of excitation are governed by two different interactions. On a macroscopical scale (> µm), dipolar coupling of magnetic moments is the dominant energy contribution. The individual moments add up to the magnetization vector $\boldsymbol{M}$

which – in equilibrium – is aligned with the effective magnetic field $\boldsymbol{H}_{\text{eff}}$ in the sample. If at some point in time $\boldsymbol{M}$ and $\boldsymbol{H}_{\text{eff}}$ are not parallel, a torque $\boldsymbol{M} \times \boldsymbol{H}_{\text{eff}}$ occurs and $\boldsymbol{M}$ is subject to the Landau-Lifshitz-Gilbert (LLG) equation of motion [BH05]

$$\frac{d\boldsymbol{M}}{dt} = -\gamma\mu_0 \boldsymbol{M} \times \boldsymbol{H}_{\text{eff}} + \frac{\alpha}{M_{\text{S}}}\left(\boldsymbol{M} \times \frac{d\boldsymbol{M}}{dt}\right).$$

Therein, the parameter $\alpha$ is the Gilbert damping constant and the respective summand describes the energy dissipation. Intrinsic to the LLG equation is the constancy of $|\boldsymbol{M}| \equiv M_{\text{S}}$ ($M_{\text{S}}$ being the saturation magnetization), ultimately stemming from the conservation of the spin.

Elementary excitations called spin waves are given by a constant phase relation between neighboring magnetic moments, as depicted in figure 1.1. Dipolar spin waves have comparably large wave lengths in the micron-range which allows for locally resolved studies. In that respect, a (ferrimagnetic) material of particular relevance is yttrium iron garnet (YIG), since its low intrinsic damping leads to spin-wave propagation lengths of up to centimeters [SCH10]. As a result, considerable research has been devoted to YIG, finally evolving to logic devices built from spin-wave cables [SSHK08].

However, potential devices require micro-to-nano-scale applications. When it comes to miniaturization, the energetical contribution of the exchange interaction dominates over the dipolar interaction. The above-quoted LLG equation remains valid for local electron spins. That is, it has to be reformulated for an individual electron spin $\boldsymbol{S} = (S_x, S_y, S_z)$, keeping in mind the concept of the magnetization $\boldsymbol{M}$ being an average over spins,

$$\boldsymbol{M} = \frac{g\mu_{\text{B}}}{\hbar}\langle \boldsymbol{S} \rangle.$$

On the microscopical, i.e. quantum-mechanical level, operators for creation and annihilation of spin waves can be formulated [GM96]. The corresponding minimum excitation energy is equal to the energy of a single reversed spin in an ensemble of otherwise parallel spins. In this picture, the quanta of excitation can be considered as quasi particles and are called magnons.

Both pictures of dipolarly coupled magnetic moments and exchange coupled electron spins are contained in the generic schematic in figure 1.1. For simplicity, the magnon wave vector $\boldsymbol{k}$ is assumed to be perpendicular to the external magnetic field $\boldsymbol{H}_{\text{ext}}$ which aligns the spins or moments to yield the magnetization vector. A spin wave is then characterized by its frequency $\omega = 2\pi f$ and

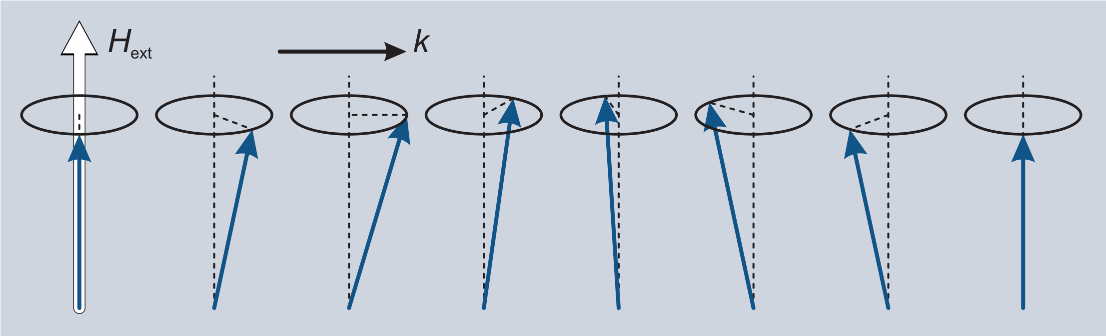

**Figure 1.1 – Spin-wave schematic.** Blue arrows represent electron spins or magnetic dipole moments aligned with an external field $H_{\mathrm{ext}}$. The wave vector $k$ of magnetic excitations existent at $T > 0\,\mathrm{K}$ can be of the order of $1\,\mathrm{mm}^{-1}$ up to $1\,\mathrm{nm}^{-1}$. In that respect, the predominant interaction is either the dipolar interaction between effective moments or the exchange interaction between electron spins. Both allow for a constant phase relation between neighboring moments or spins, respectively, leading to spin waves with frequencies in the GHz- to THz-regime.

wave length $\lambda = 2\pi\, k^{-1}$, and theoretical calculations yield the spin-wave modes and their dispersion $\omega(\boldsymbol{k})$. In the nano-regime, since the exchange interaction is isotropic, $\omega(\boldsymbol{k})$ is independent of the relative angle between $\boldsymbol{M}$ and $\boldsymbol{k}$ and takes a quadratic form $\omega \propto k^2$ [KH50].

By contrast, in the dipolar-dominated case, different geometries are possible and lead to anisotropic dispersions, where the two limiting cases $\boldsymbol{k} \parallel \boldsymbol{M}$ and $\boldsymbol{k} \perp \boldsymbol{M}$ are called the Damon-Eshbach and Backward-Volume modes, respectively [DE61]. Analytical expressions for mixed exchange and dipolar magnetic modes can also be derived [KS86].

Experimental investigations of spin waves span a wide range of decades and techniques. An approach of particular importance for the present work is the all-optical excitation and detection with ultrashort laser pulses [vKJK+02], making use of the electro-magnetic coupling between electrons and photons [Ker77]. Respective results from reference [LEHM10] are reprinted in chapter 2: on a continuous ferromagnetic film, non-thermal spin waves are investigated. Intense laser pulses excite the magnetization dynamics and populate the different modes of precession mentioned above. An identification is facilitated by the modes' frequencies depending differently on the applied external field, and observed spin-wave lengths span both the exchange and dipolar regime. In view of the present thesis, this is the basis for investigations of periodically structured systems and their effect on the spin-wave population.

## Manipulating waves with metamaterials

> We may speak of the form (or the thing as having a form) as an individual thing, but we may never so speak of that which is material by itself.
>
> Aristotle, Metaphysics, VII 1035a

Wave propagation is crucially dependent on the host medium. In general, this refers to the microscopic coupling between the individual oscillators, given for example by exchange stiffness, surface energy, or elastic modulus. Resulting wave lengths are much larger than the distance between oscillators and in that respect, the host material is thought to be continuous. However, a periodic structure with a length scale of the dynamic excitation allows for the manipulation of static and dynamic properties of the sample system.

An appropriate choice of a structural unit and its long-range ordered arrangement can be used to control essentially any sort of wave. With a periodic structure, an effectively new material with intrinsic properties different from the bulk is created. By definition, it is these new properties that require the use of the term *metamaterial*: since the emerging effects cannot by derived from the independent properties of the host material and periodically arranged constituents, they represent a deviation from the common physical understanding of matter [Sup74].

Notably, this general statement applies to many orders of magnitude in time and length scales. For real and Fourier space, two examples are depicted in figure 1.2. In (a), surface water waves with typical sub-Hz frequencies are focussed after traversing a lens-shaped arrangement of copper cylinders [YTO$^+$09] – an effect which had been predicted from a multiple scattering formalism [HC05]. Second in figure 1.2(b), results from a finite-element calculation on acoustic steel resonators are presented [Hsu11]. In such a system, frequencies lie in the 100 kHz-range and individual resonators are separated by millimeters. Still, in close analogy to electronic band structures in solid state physics, *phononic* band gaps are observed.

While these examples have been illustrated only in brevity, they emphasize an important point: the periodic arrangement of artificial atoms (copper cylinders or steel resonators) does not modify existing properties of the host material itself (water or air), but creates novel phenomena. The equivalence of real and Fourier space can be made use of in order to gain an insight from different points of view and to develop an understanding of the relevant physical effects. An additional generalization can be made: close interaction between theoretical/numerical work and experimental studies provides the different perspectives for a most possibly

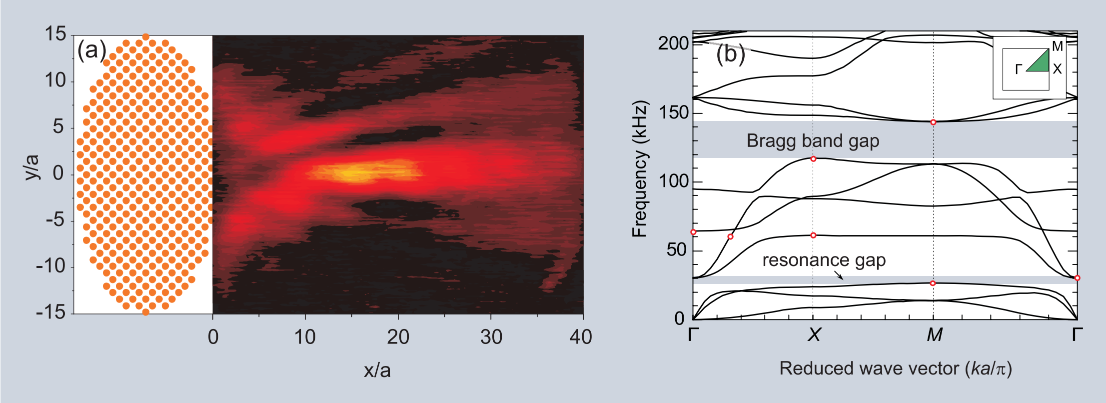

**Figure 1.2 – Manipulation of waves with metamaterials.** In real space, the focussing of surface waves in water has been experimentally observed and is presented in (a). Small copper cylinders of diameter $d = 2\,\text{mm}$ are periodically arranged on a lattice with parameter $a = 6.7\,\text{mm}$ and lead to an increased amplitude in the focal point for plane waves impinging from the left [YTO+09]. On the other hand, calculations in Fourier space yield band structures as exemplified in (b): phononic crystals composed of steel resonators (size and separation in the mm-range) show band gaps which shift in frequency and change in size for different structural constituents [Hsu11]. Red points mark sound modes discussed in detail in the reference.

extensive understanding of emerging effects.

Another example of metamaterials with a particularly broad spectrum of applications is the field of *photonics*. For light, the use of periodic structures allows such unexpected behavior as bending around corners or switching between two (optical) output channels [JJWM08, pp. 204]. Moreover, light propagation can considerably be slowed down in photonic crystals [Kra07] – even the localization of light in sub-wavelength energy hot spots has been achieved [KJRZ11]. The reprint of reference [LUGM11] in chapter 3 presents a more detailed view on the analogy between metamaterials for light and spin waves. Therein, also an elusive discussion of the rivalling effects of localization and propagation of spin waves (tunable by host material and periodic structure) is given. Furthermore, the aforementioned equivalence of real and Fourier space is exploited: on the one hand, time-resolved experiments show the ultrafast excitation of different types of spin waves, while on the other hand band-structure calculations verify their *magnonic* character – a term to be described in the following section.

## Magnonic crystals

A major part of the present work is the investigation of emerging effects in long-range ordered, periodically structured ferromagnetic materials. The respective field of research devoted to these magnetic metamaterials, called magnonic crystals, has been coined *magnonics* around the year 2001 [NTT01], a point in time marking the revival of ideas on structured magnets discussed as early as 1976 [SAC76].

Chapter 3 reprints a review paper on magnonics which includes an elaborate introduction. To avoid doubling, respective contents are not repeated here. Instead, because of their importance for this thesis, two-dimensional systems will briefly be described – in particular, thin ferromagnetic films periodically structured with micron-sized holes. Following the convention in literature, throughout this thesis the term *antidots* will be used for the structural units. This is to emphasize the contrast to the multitude of studies devoted to separated ferromagnetic islands (i.e., dots) and their potential applications [WTK+98].

As generally noted for metamaterials in the previous section, also magnonic crystals show properties that cannot be deduced from the individual ingredients. For example, spatially resolved studies on single antidots reveal their function as scattering sites for spin waves [BOT+09]. However, if arranged on a square lattice, the antidots induce new spin-wave modes which are specific to the lattice and mostly independent of the single antidot properties [ULM10]. The excitation of these *magnonic* modes can be understood in terms of a magnonic band structure, also investigated in detail in chapter 3. The formalism for the band-structure calculations has to account for the – as compared to photonics – complication of a spatially varying magnetic permeability [VDDRP96]. In analogy to figure 1.2(b), magnonic band gaps occur which have been shown to be tuneable by design [LHK09, CCG+12]. The position of these band gaps and the accompanying flattened spin-wave bands are closely connected to the experimentally observed magnonic modes.

The concepts described above and the investigations on structured media in chapter 3 provide the perspective to make use of the high spin-wave frequencies and the versatility of metamaterials. One example are anisotropic magnonic crystals which allow the tuning of magnonic spin-wave modes by rotation of the external field. Respective results from reference [LAPM12] are reprinted in chapter 4, containing a direct comparison between numerical calculations and experimental investigations. The findings are based on chapters 2 and 3 in that the principles of ultrafast spin-wave excitation are exploited to populate only selected (and tunable) dynamic magnonic modes. Finally, band-structure calculations can conclusively be related to the experiments.

Aiming at the application of magnonic devices, chapter 4 also discusses a scheme for spin-wave filtering. With the focus on rectangular antidot lattices, the degree of freedom imposed by the external magnetic field is of high importance:

it provides an additional control parameter to tune the magnonic modes.

In summary, the present thesis is devoted to the optical excitation of spin waves (chapter 2), to the challenge of spin-wave selection and modification with metamaterials (chapter 3), as well as to the underlying interactions and their utilization in an example application (chapter 4). The final chapter 5 gives a general discussion and places the findings into a wider context.

## Chapter 2

# Spin-wave population in nickel after femtosecond laser pulse excitation

B. Lenk, G. Eilers, J. Hamrle, and M. Münzenberg

Physical Review B **82**, 134443 (2010)
DOI: 10.1103/PhysRevB.82.134443

**Abstract.** The spin-wave relaxation mechanisms after intense laser excitation in ferromagnetic nickel films are investigated with all-optical pump-probe experiments. Uniform precession (Kittel mode), Damon-Eshbach surface modes and perpendicular standing spin waves can be identified by their dispersion $\omega(H_{\text{ext}})$. However, different to other ferromagnets $\omega(H_{\text{ext}})$ deviates from the expected behavior. Namely, a mode discontinuity is observed, that can be attributed to a non-linear process. Above a critical field the power spectrum reveals a redistribution of the energy within the spin-wave spectrum populated.

## 2.1 Introduction

Spin-wave generation and manipulation have already been demonstrated in many ways [DSA+04]. They are of great importance in magnetism-based spin-wave logic and XNOR as well as NAND gates have recently been implemented [SSL+08]. To reduce the size of potential devices, effective spin-wave pumping mechanisms are needed in ferromagnetic metallic films owning micron to nanometer characteristic magnetic length scales. Here we present a pumping mechanism using femtosecond laser excitation that allows for a large precession angle ($> 3°$) after local excitation. On the other hand, the relevant length scales can be artificially selected by the design of magnonic crystals, i.e. periodically microstructured and nanostructured magnetic materials, with only very selected dynamic eigen states [ULM10].

For large precession angles the equations of motion are intrinsically non-linear. This can be used to pump energy into a certain spin-wave mode by non-linear interaction and becomes evident for example in spin-wave nano-oscillators [ST06, KPR+05, MRET05]. Given a spatial separation of two spin-torque oscillators and hence, an overlap in their spin-wave power when excited by a direct current, one finds a locking of frequencies if the frequency mismatch is below a critical

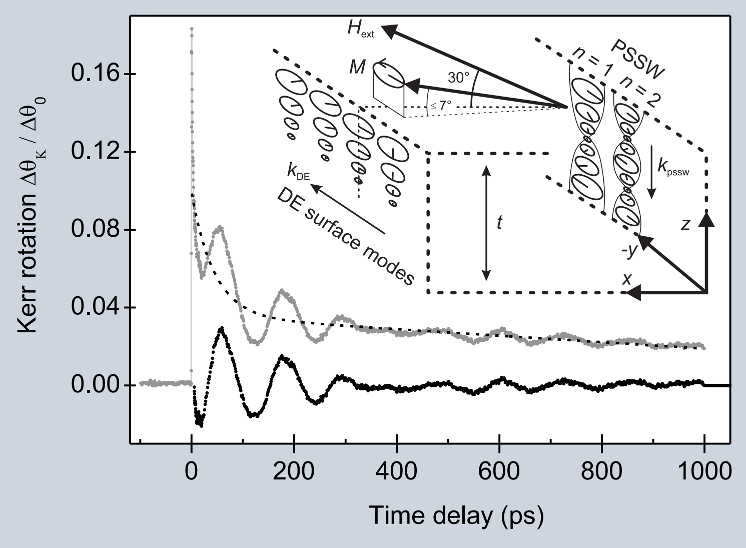

**Figure 2.1 – TRMOKE measurement and scheme of spin-wave modes.** Time-resolved measurement of the pump-induced change of the Kerr rotation (light gray) and the fitted background (dashed line) that is subtracted to yield the residual oscillation (black). The data set shown has been recorded at a nickel thickness of 80 nm under an external field of 140 mT. A large angle of precession as high as 3° is observed. Inset: Schematic representation of spin-wave modes in a continuous ferromagnetic film of thickness $t$. Local amplitude and phase of the dynamic magnetization $m(t)$ are illustrated. Shape anisotropy accounts for mainly in-plane alignment of the magnetization $M = M_S + m(t)$.

value. Driven to an extreme, a steady transfer of energy from higher to lower energy modes results in Bose-Einstein condensation observed at room temperature [DDD+08].

In the following we focus on dipolar and exchange spin-wave modes in continuous films excited by intense laser pulses, where the nature of the excited spin-wave modes is tuned by the external magnetic field. The excitation by femtosecond laser pulses has major differences as compared to methods that work in thermal equilibrium. These are for example Brillouin light scattering (BLS) [JDM+99], conventional ferromagnetic resonance (FMR), strip-line based techniques like vector network analyzer [NBG08] or spatio-temporal Kerr effect based FMR used to study spin-wave modes [PYC+05].

Our technique works in space and time-resolved manner and the detection process owns no $k$ selectivity a priori. Yet, the strongest difference to resonant techniques is the broadband excitation in the spin system [DM07, ACFW+10], by which all magnetic modes are excited. However, only resonant modes contribute to the signal coherently and can be detected while others appear as non-coherent background. A further advantage is the contact-free, very local excitation and detection which simplifies the testing of various samples and structured media.

We make the very unusual observation that below a critical magnetic field two dominant spin-wave modes are excited, whereas above the critical field, they merge into one single mode. We shall also see, that intrinsic to the experimental method used, surface modes are preferentially excited if the sample thickness considerably exceeds the penetration depth of the laser field.

In general, magnetic precessional motion can have dipolar and exchange spin-wave character and can be described as follows. Starting from the free magnetic energy density, the Landau-Lifshitz equation of motion for the magnetization vector $M$ yields a theoretical dispersion describing the uniform precession (also referred to as the Kittel mode) in the macrospin approximation [Far98]

$$\left(\frac{\omega_\mathrm{k}}{\gamma\mu_0}\right)^2 = H_x\left(H_x + M_\mathrm{S} - \frac{2K_z}{\mu_0 M_\mathrm{S}}\right), \tag{2.1}$$

where $\mu_0 M_\mathrm{S}$ is the saturation magnetization (being $= 659\,\mathrm{mT}$ for nickel), the only free parameter $K_z$ accounts for the effective anisotropy in the out-of-plane direction, and $H_x$ is the component of the external field projected to the sample plane.

Damon and Eshbach solved the equation of motion accounting for Maxwell's equations in the magnetostatic limit and adequate boundary conditions yielding the dispersion for long wavelength surface modes, so called Damon-Eshbach (DE) modes:

$$\left(\frac{\omega_\mathrm{DE}}{\gamma\mu_0}\right)^2 = H_x\left(H_x + M_\mathrm{S}\right) + \frac{M_\mathrm{S}^2}{4}\left[1 - \exp(-2k_\mathrm{DE}t)\right]. \tag{2.2}$$

Here, $t$ is the film thickness and $k_\mathrm{DE} \perp M_\mathrm{S}$ denotes the wave vector of the magnetostatic surface wave. An analogous approach in reference [KS86] yields dispersion characteristics taking into account exchange interaction as well as anisotropy. In thin magnetic layers one finds a quantization of the wave vector perpendicular to the sample plane and in analogy to equation (2.1) one can give a dispersion describing the exchange-dominated perpendicular standing spin waves (PSSWs),

$$\left(\frac{\omega_\mathrm{pssw}}{\gamma\mu_0}\right)^2 = \left(H_x + \frac{2A}{\mu_0 M_\mathrm{S}}\,k_\mathrm{pssw}^2\right)\left(H_x + M_\mathrm{S} - \frac{2K_z}{\mu_0 M_\mathrm{S}} + \frac{2A}{\mu_0 M_\mathrm{S}}\,k_\mathrm{pssw}^2\right). \tag{2.3}$$

Therein, $A$ is the exchange constant and $k_\mathrm{pssw} = n\pi\,t^{-1}$ is the quantized wave vector in out-of-plane (i.e., $z$-) direction attributed to a given order $n$ of the PSSW.

A schematic of the different magnetic modes is given in the inset of figure 2.1 where the Kittel mode is not explicitly drawn, as both PSSW and DE modes result in the uniform precession in the limit $k_{\mathrm{pssw}} \to 0$ (i.e., $n = 0$) and $k_{\mathrm{DE}} \to 0$, respectively.

## 2.2 Experiment

The samples consist of polycrystalline nickel films with thicknesses of up to 220 nm. The thickness dependence of the occurring modes is measured on a wedge-shaped sample to perform all measurements on one specimen. It was prepared by electron beam evaporation in ultra high vacuum under a base pressure of $5 \times 10^{-10}$ mbar. A linearly moving shutter was used to produce a nickel wedge with thickness $20\,\mathrm{nm} \leq t \leq 220\,\mathrm{nm}$ on a Si(100) substrate and in order to prevent oxidation, the ferromagnetic layer was capped with 2 nm of copper.

For the experiments we use an approach in the time domain, i.e. an all-optical pump-probe setup as previously described in reference [DEP+06]. An ultrashort laser pulse with 60 fs duration and $\lambda_c = 810\,\mathrm{nm}$ central wavelength excites the saturated sample and at a variable time delay $\tau$ a second laser pulse with the same characteristics but 5% of the intensity probes the time-resolved magneto-optical Kerr effect (TRMOKE) [BMDB96, JVN+98, vKJK+02]. Therewith, spin dynamics in the femtosecond regime can be detected, where electronic excitations lead to a demagnetization and subsequent relaxation into the initial state via scattering of high energy to low energy spin waves [DM07].

The processes that initially quench the magnetization in the first few picoseconds are subject to ongoing discussions [KMD+10], but can be modeled quite successfully in some detail [ACFW+10]. Here in focus are oscillations on a time scale from 30 ps to 1 ns. We shall see, that all modes corresponding to equations (2.1)-(2.3) can be optically excited in a thin ferromagnetic film. In a simplified picture the mechanism can be regarded as an effective-field pulse which stems from the heat-induced change in the sample's anisotropy and local exchange field upon absorption of the pump pulse [LSK+07]. Therefore, to promote magnetic precession of the Kittel mode, the external field was tilted by 30° out-of-plane thus giving rise to an angle between sample plane and the effective internal field $H_i \parallel M_{\mathrm{S}}$. For an external field of $\mu_0 H_{\mathrm{ext}} = 150\,\mathrm{mT}$, which is the maximum used in the experiments, we calculated a rotation of 7° of $H_i$ out of plane due to the Zeeman term in balance with the shape anisotropy (see also figure 2.1). The angle is rather small and thus, its influence can be neglected for simplicity. Hence, in the analytical expression of the spin-wave modes we assume $H_i$ and $M_{\mathrm{S}}$ to be in-plane. The data presented here have all been recorded with the field applied under 30°. Please see the supplemental materials section for experiments at other angles and a detailed hysteresis analysis [LEHM10].

## 2.3 Results and discussion

In order to obtain the precession frequencies from the time-dependent MOKE spectra, the incoherent background owing to phonons and magnons is subtracted. This procedure is demonstrated in figure 2.1 with a single measurement recorded at $\mu_0 H_{\text{ext}} = 140\,\text{mT}$ and $t = 80\,\text{nm}$. After subtraction of the background (black data points in figure 2.1), Fourier transformation of the $M(\tau)$ curves yields peaks in the oscillations' power spectra. For a given thickness $t$, the external field is varied between 0 and 150 mT, resulting in a change in amplitude and frequency of the oscillation. The position of the corresponding peaks in the frequency domain is determined for each such set of measurements and plotted versus $\mu_0 H_{\text{ext}}$.

Shown in figure 2.2 are power spectra recorded on different nickel thicknesses, revealing up to three precessional modes of different origin. In the upper row the Fourier power spectra for a given thickness are plotted in a color map as calculated from the $M(\tau)$ curves (the Fourier transformation of the data from figure 2.1 is marked with a vertical gray line). In the bottom row all spectra have been normalized by their respective maximal fast Fourier transform power to give a better overview of mode evolution. The data points represent the peak positions and included as solid lines are the fitted theoretical frequency dispersions [equations (2.1)-(2.3)] of the various modes, which have been used to attribute the branches to the Kittel mode, the DE surface mode as well as the PSSW mode with $n = 1$.

Analysis of the thickness-dependent occurrence of the different magnetic modes yields the results depicted in figure 2.3. For a given external field of 50 mT the observed frequencies have been extracted and the aforementioned identification of Kittel, PSSW, and DE modes is confirmed. Both the Kittel mode (black) and the PSSW (gray) display the expected evolution with the thickness: while the frequency of uniform precession $\omega_{\text{K}}$ remains unchanged, the frequency of the PSSW reduces. Being proportional to $t^{-2}$ it approaches $\omega_{\text{K}}$ in accordance to literature [ST58].[1]

The DE modes (blue lines and points in figure 2.3) have been predominantly studied with BLS [GMVG82]. We find from our experiment that they are first excited at a nickel thickness of 80 nm. There, they are only present at low external fields, but for thicker nickel layers these modes dominate the spin-wave dynamics over a wider field range up to $\mu_0 H_{\text{ext}} = 90\,\text{mT}$. This is due to the excitation

---

[1] From the fit in figure 2.3 (solid gray line) the exchange constant $A = 6.9(5)\,\text{pJ}\,\text{m}^{-1}$ was extracted.

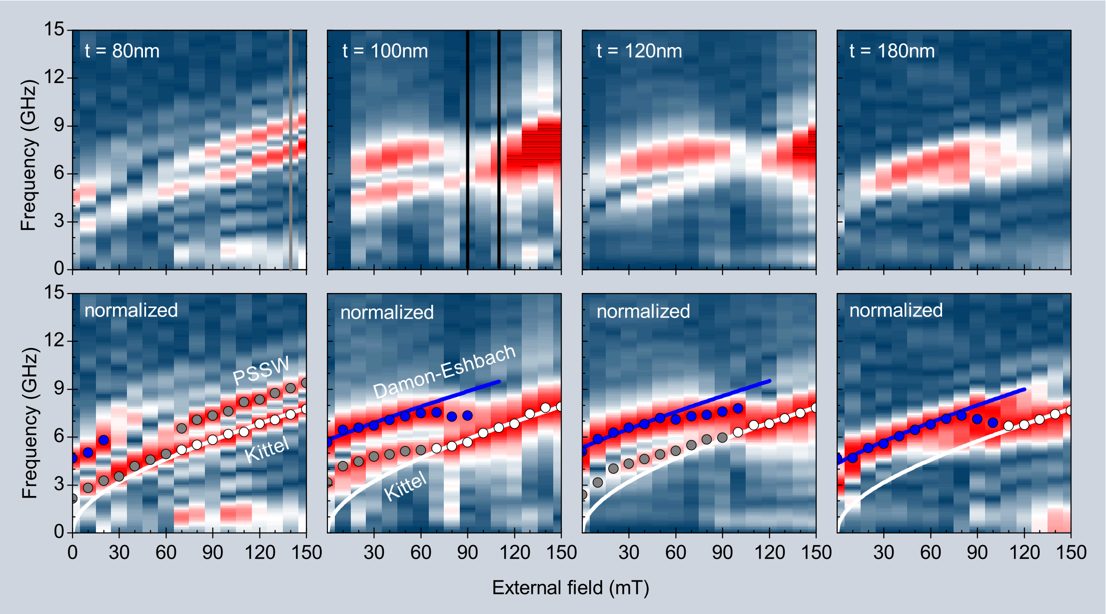

**Figure 2.2 – Spin-wave power spectra of thin nickel films with $t$ = 80-180 nm.** Magnetic oscillations are observed after optical excitation (top plots) and normalization yields frequency branches (bottom plots), that can be attributed to uniform precession (white points), magnetostatic surface waves (blue points) as well as perpendicular standing spin waves (gray points). Solid lines represent theory according to equations (2.1) to (2.3). The vertical gray line at 80 nm of nickel corresponds to the data set from figure 2.1, vertical black lines for 100 nm denote Fourier spectra analyzed in figure 2.4. Please note the mode discontinuity around $\mu_0 H_{\text{ext}} = 90\,\text{mT}$ for $t > 80\,\text{nm}$.

mechanism and its relevant length scales: sample thickness $d$ and optical penetration depth $\Lambda_{\text{opt}}$ (i.e., penetration depth of the electrical field at optical frequencies which evaluates to $\lambda/(2\pi\Im(N)) \approx 30\,\text{nm}$, where $N$ is the complex refractivity index). Calculations that show our experiments' sensitivity to magnetic modes in the top 15 nm of the ferromagnet can be found elsewhere [HPH+10].

The magnetic excitation depth is governed by the penetration of the laser field and energy is deposited in form of an initial disarrangement of spins [DM07]. This energy will very effectively excite eigen modes with similar spatial profile and thus, by choosing a thickness $t \gg \Lambda_{\text{opt}}$, the resulting strong asymmetry will make DE surface modes the favored relaxation channel. Consequently, the appearance of the DE modes is based on the fact that they own an amplitude profile with the maximum at the surface, decaying exponentially into the film. Herein lies a strong analogy to surface acoustic waves excited with laser pulses, which can be used to determine elastic properties of surface layers [NH92].

Assuming a propagation direction perpendicular to the magnetization ($k_{\text{DE}} \perp M_{\text{S}}, H_{\text{ext}}$) the dispersion (2.2) can be used to determine the wave vector $k_{\text{DE}}$. In the inset of figure 2.4 the respective quantitative analysis of the Damon-Eshbach modes is given. From the fits one obtains wave vectors in the inverse micrometer range, corresponding to wave lengths of about 3 µm. We find that the product $k_{\mathrm{DE}}d$ entering equation (2.2) is not constant but that the relation $k_{\mathrm{DE}} = (t - t_0)^{-1}$ holds with $t_0 = 66(4)\,\mathrm{nm}$ (solid gray line in the inset of figure 2.4). The divergence of $k_{\mathrm{DE}}$ around that value supports our earlier interpretation.

An asymmetry between film thickness and optical excitation depth is needed to give rise to dipolar spin waves in contrast to exchange-dominated spin waves with rather high $k$. In other words, the parameter $t_0$ can be considered an onset thickness above which the dipolar interaction comes into play. In general, our understanding of the selection of the DE wave vector is not fully developed. However, we can exclude that the laser spot sizes of pump (60 µm) or probe (20 µm) enforce a selection, since the observed DE wave lengths are on the order of only very few microns. A tentative reduction in the probe beam diameter to 14 µm did not result in a change in $k_{\mathrm{DE}}$. The pump beam on the other hand is only present for a very short period of time. The formation of a boundary condition resulting from the demagnetized spot and a selection of the $k$ vector whose wavelength is related to multiples of the demagnetization spot is therefore improbable. Most importantly the characteristic thickness dependence of $k_{\mathrm{DE}}$ is a counter indication for the latter model.

Another possibility for the formation of the Damon-Eshbach mode is a periodic inhomogeneity of the magnetization intrinsic to the ferromagnetic film. The supplemental data include hysteresis curves for various film thicknesses which will be discussed in the following [see appendix A for supplemental data]. The coercive fields are around 20 mT, which is well below the area of interest. It is clear that if magnetic domains appeared, their irregularity would destroy any coherent and well defined Damon-Eshbach mode.

In the experiments the TRMOKE spectra have been measured by applying 150 mT and subsequently reducing the magnetic field after saturation of the sample. However, periodic ripple patterns are known to appear in materials with small crystallites to adapt the direction of the local anisotropy. Typically in the few microns range the deviation of the magnetization direction can be up to a few 10° [GCXC05]. The ripple patterns are known to change periodicity depending on the film thickness and could explain the longer wave lengths observed for thicker Ni films. Still, certain difficulties in this model arise that do not match some of our observations. First, the region of existence terminated by the critical field does not match the saturation field values that are typically much lower. Also, we observe a constant $k$-vector over a wide field region, indicating that the

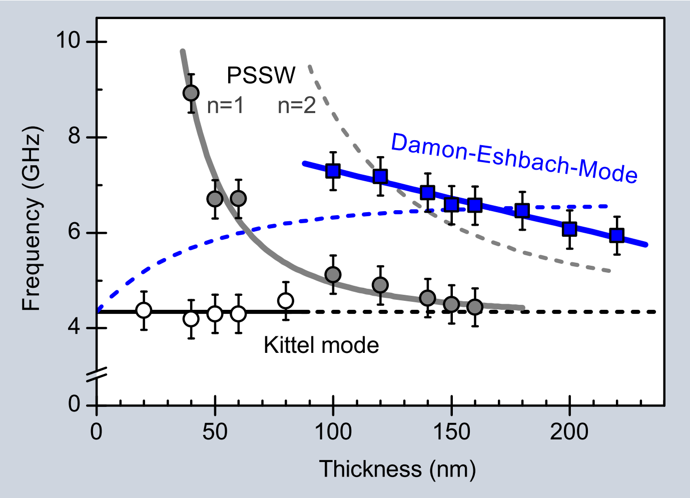

**Figure 2.3 – Spin-wave modes at $\mu_0 H_{\mathrm{ext}} = 50\,\mathrm{mT}$ for varying thickness $t$.** Below 40 nm only the uniform precession (white points, black line) is observed, which does not change in frequency for increasing $t$. Perpendicular standing spin waves with $n = 1$ can also be identified (gray) and fit well to the expected $t^{-2}$ behavior [ST58]. PSSW of second order are not observed (dashed gray line), instead Damon-Eshbach surface waves (blue) are excited. The blue dashed line represents the DE dispersion (2.2) with $k_{\mathrm{DE}} = 1\,\mu\mathrm{m}^{-1}$ and reveals that the DE wave vector is not constant in our experiment (the solid blue line is a guide to the eye).

periodicity of the (hypothetical) ripple pattern is almost field independent. This opposes experimental findings by Gentils et al. who found a strong dependence of the ripple periodicity on the applied field [GCXC05].

Further experiments using Kerr microscopy performed in collaboration with the IFW at Dresden did not yield any evidence for ripple patterns. Instead, rather large domain structures above 15 µm dominate the magnetization reversal. A periodic variation in the magnetization can thus be rather only small in angle, but also too small then to form the periodic potential for the selection of the $k$-vector of the Damon-Eshbach standing wave. Moreover, the periodicity of the ripple pattern is found along the direction of the applied field while the Damon-Eshbach modes propagate perpendicular to that. Such a periodic magnetic pattern could only form a periodic boundary condition for the backward volume mode. The respective energy when compared to the Kittel mode should be lower, which is not consistent with our data. At this stage we conclude, that we cannot totally exclude an effect of an inhomogenous magnetization but considerable observations point against such an interpretation.

As described, the DE mode dominates the spectra up to critical fields as high as $\mu_0 H_{\mathrm{crit}} = 90\,\mathrm{mT}$. Around that value, an explicit deviation from the theoretical dispersion arises (blue line and points in the bottom row of figure 2.2). A distinct modification of the DE mode intensity takes place which – for sufficiently high fields – ultimately results in a peculiar characteristic evident in figure 2.2. Namely, the DE mode merges into the Kittel mode. This leads to a very strong increase in the total Fourier power, i.e., precession amplitude, as seen in the non-normalized data (upper row of figure 2.2). The propagating surface mode seems to lock to the frequency of the Kittel and PSSW modes for magnetic fields higher than $\mu_0 H_{\mathrm{crit}}$. Above that value, the peaks can be attributed to the dispersion of the uniform precession by equation (2.1). The fits (white lines) yield values for the effective anisotropy $K_{\mathrm{z}}$ around $50\,\mathrm{kJ\,m^{-3}}$ showing no monotonous trend with the thickness.

The idea to explain the merging of both modes is based on the alternating magnetic field that the stationary precession of the magnetization generates. In this respect, the absolute value of the amplitude is of great interest. It can be derived from the dynamic magnetization by calibration of the experiment for a given saturation magnetization: A comparison of the magneto-optical signal at zero time delay with and without pump-induced demagnetization at $F = 70\,\mathrm{mJ\,cm^{-2}}$ and $\mu_0 H_{\mathrm{ext}} = 150\,\mathrm{mT}$. This results in a precessional amplitude of $4.6\% \times \mu_0 M_{\mathrm{S}}$ corresponding to an angle of 3°. One calculates an absolute value of 30 mT which would provide a rather strong coupling field. Thus, another hypothesis to understand the observation is a locking of the DE mode to the $k = 0$ homogenous precession originating from an energy transfer between the two dynamic modes. Only if the propagating surface waves would couple to the alternating field of the Kittel mode and the amplitude of the magnetic precession could be that drastically increased.

A reasonable starting point to test this general idea is to draw parallelities to a model by Slavin and co-workers. They proved that phase locking of spin-torque nano-oscillators can take place [ST06]. In their publication, the authors use a non-linear set of equations of motion for two coupled oscillators and can explain the experimental results presented in references [KPR+05] and [MRET05]. Once the free-running frequency mismatch between the two oscillators is smaller than a threshold value $\varDelta_{\mathrm{max}}$ [equation (9) in reference [ST06]], they phase lock to a mutual frequency. The mechanism is twofold: coupling can be either mediated by spin waves radiated into a common magnetic layer or a dipole field created by the oscillators. Either way, one of the crucial parameters is the spatial separation $a$ of the two contacts, tuning the overlap of spin-wave power in real space (figure 1 in reference [ST06]).

Transferring these findings to our observation, we could speculate that an increased overlap of the magnetic modes in Fourier space leads to a sudden interaction such that locking takes place. Figure 2.4 illustrates this hypothesis:

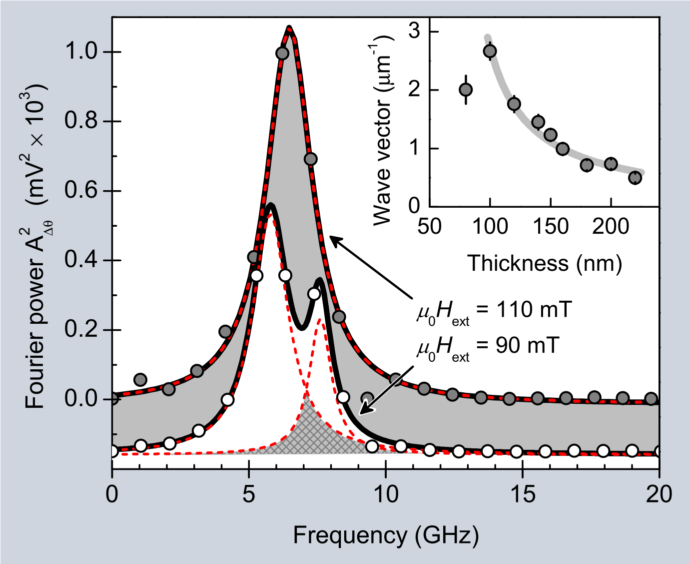

**Figure 2.4 – Fourier linewidths and Damon-Eshbach wave vector.** Gray and white points denote the Fourier power $A^2_{\Delta\theta}$ as calculated from the time-resolved MOKE measurements at $t = 100\,\text{nm}$, $\mu_0 H_\text{ext} = 110\,\text{mT}$ and $90\,\text{mT}$, respectively. Solid and dashed lines represent Lorentz-Peaks which where fitted to the data. The expected linewidth in nickel is larger than 1 GHz and as a result, possible mode locking leads to the population of only a single mode at 110 mT if the overlap indicated by the hatched area is increased. Additionally, the mutual intensity is strongly increased. In the inset, the dependence of the Damon-Eshbach wave vector on the thickness is given, where the solid gray line is a guide to the eye (see text also).

two Fourier spectra from measurements recorded on nickel with a thickness of 100 nm are shown. At $\mu_0 H_\text{ext} = 90\,\text{mT}$ clearly two precessional modes can be distinguished, whereas at $\mu_0 H_\text{ext} = 110\,\text{mT}$ only one smooth peak with nearly identical width is found. The two modes observed, namely uniform precession and DE surface waves, are separated in Fourier space by several gigahertzs at low external fields. However, if $\mu_0 H_\text{ext}$ is increased in the experiment, the separation reduces and at one point approaches the value of the linewidth, which implies an overlap in the frequency domain (hatched area in figure 2.4). Above a threshold overlap the frequencies seem to lock and the two modes cannot be distinguished anymore. Moreover, a single smooth peak in the Fourier spectrum is observed. Concerning the evolution with increasing magnetic field, a step-like change in the DE frequency is apparent in the Fourier spectra in figure 2.2 and hence, the term mode locking seems justified.

Equivalent to the damping time constant $\tau_\alpha$ in the time domain is the linewidth in the Fourier domain. From $\tau_\alpha$ apparent in the time-resolved MOKE spectra one expects the width of the peak after Fourier transformation to be $(\pi\tau_\alpha)^{-1}$ at 50% of maximum power (full width half maximum). For nickel the expected line width

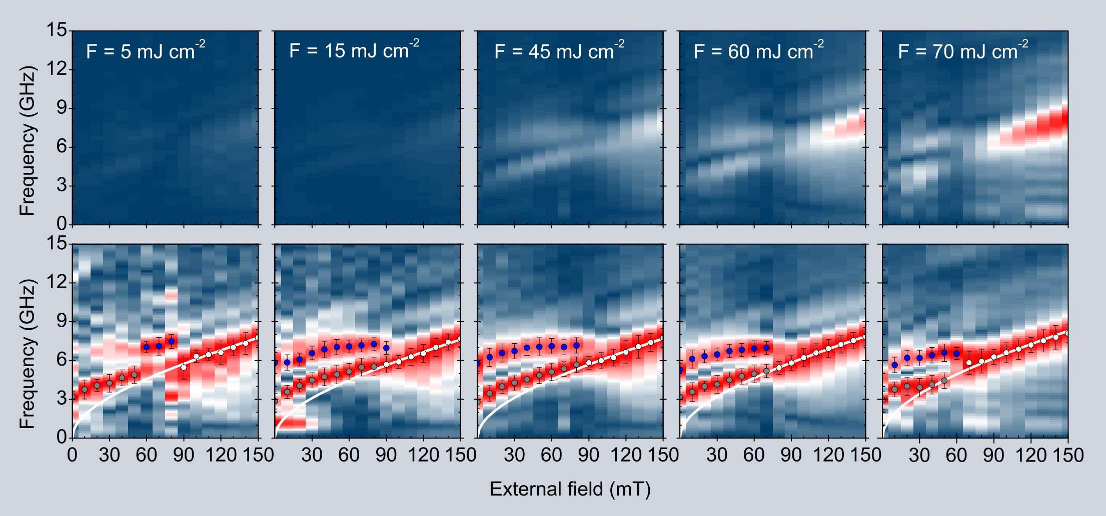

**Figure 2.5 – Fourier power spectra for different pumping fluences $F$ = 5-70 mJ cm$^{-2}$ with $t$ = 150 nm.** The identification of modes corresponds to figure 2.2 and the color scale in the top row (not normalized plots) is the same for every spectrum to reveal the fluence-dependence of the precession amplitude. One observes a strongly increasing amplitude of the uniform precession with increasing fluence, whereas the bottom row (normalized data) shows a small shift of the critical field towards lower values, which will be detailed in figure 2.6.

therefore is 1.1 GHz, using $\tau_\alpha = 300$ ps, which has been extracted from the time-resolved spectra. Due to the strong damping in nickel (implying a rather large line width) considerable overlap can occur. The interplay with $H_{\text{ext}}$ tuning the DE and Kittel frequency mismatch leads to possible phase locking (see figure 2.4). Normally, the synchronization time of two oscillators depends on their interaction strength. We do not observe any hints for delayed synchronization in our data which is a counter indication for this hypothesis [see appendix A for supplemental data]. However, also significant differences to the analogy to two coupled oscillators come into play. First, the different excitation mechanism using optical pump pulses ensures the same initial phase which simplifies a synchronization. Second, in the spin-wave picture after laser excitation in the hot disordered ferromagnet, a broad spectrum of spin waves is present. By the alternating field of the Kittel mode the population of the Damon-Eshbach state with the wave vector $k$ previously found at lower fields is hindered. Only spin waves synchronized with the frequency of the Kittel mode can be populated in the relaxation process. This relaxation happens very fast and takes place within 30 ps [DM07]. In this context, the high energy of the pump pulses is of great importance. It is delivered on ultrafast time scales pushing the system far out of equilibrium and must be considered when discussing the effects observed.

A test for our hypothesis based on non-linearity is the influence of the (optical) pumping power that excites the magnetization dynamics. Corresponding experiments were performed on a separate continuous nickel film which was 150 nm thick and was prepared as described above. For the measurements, the pumping fluence was varied over one decade ranging from 5 to $70\,\mathrm{mJ\,cm^{-2}}$. The resulting Fourier power spectra are presented in figure 2.5 and reveal that the nature of the magnetic modes excited by the pump pulses does not significantly change. To give a better insight into the fluence dependence, all power spectra in the top row are identically color-scaled. This shows an increase in the spin-wave amplitude with the fluence (from left to right) as expected when considering the heat-induced disorder triggering the oscillation [LSK$^+$07]. This increase is quantitatively given in the inset of figure 2.6(b), where the Kittel amplitude at $\mu_0 H_\mathrm{ext} = 150\,\mathrm{mT}$ has been plotted versus the pumping fluence (gray points).

A feature of figure 2.5 that requires a closer look is the somewhat changing critical field for the transition from surface to uniform characteristics. Figure 2.6(b) details the corresponding analysis and gives the respective results in the inset. Starting from the fit of the Kittel dispersion [equation (2.1)] to the data (white lines in the bottom row of figure 2.5) the amplitude of the Kittel mode for each magnetic field is extracted from the data. In the normalized case, this amplitude equals 1 if $H_\mathrm{ext} > H_\mathrm{crit}$ and below the critical field a monotonous, in good approximation linear behavior is found. By a linear fit, the point at which the Kittel amplitude reaches 1, i.e., above which the Kittel mode is the dominant mode of precession, can be determined. We define this field value as the critical field $H_\mathrm{crit}$ [also marked by vertical lines in figure 2.6(b)]. The above described procedure is explicitly given in figure 2.6(b) for the fluences $5\,\mathrm{mJ\,cm^{-2}}$ and $60\,\mathrm{mJ\,cm^{-2}}$, respectively. In the inset the overall decrease in $\mu_0 H_\mathrm{crit}$ for increasing $F$ is shown. Together with the threshold-like onset of the population of the uniform precession in figure 2.6(a) and the accompanying rapid increase in precession amplitude our initial hypothesis of a non-linear transfer of energy seems to speak in favor of the mode coupling.

## 2.4 Conclusion

In conclusion, we have identified the excitation of the uniform precession (Kittel mode) as well as magnetostatic surface waves (DE mode) in asymmetrically pumped nickel films. Below a critical magnetic field $H_\mathrm{crit}$ the dipolar DE modes dominate the precession, whereas a step-like feature in the dispersion $\omega_\mathrm{DE}(H_\mathrm{ext})$ indicates the population of the $k = 0$ mode above $H_\mathrm{crit}$ (figure 2.2). The observation of the DE surface waves for $H_\mathrm{ext} < H_\mathrm{crit}$ can be understood by considering

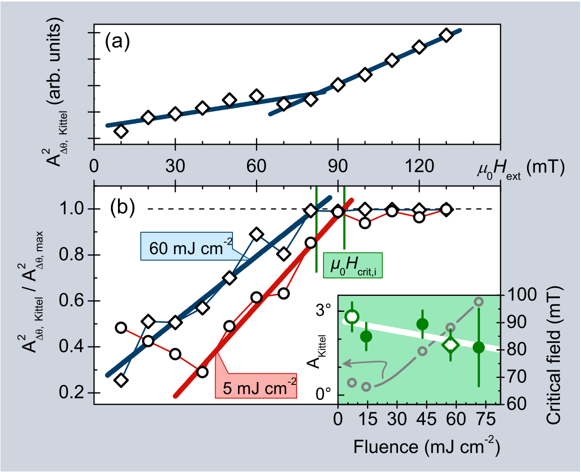

**Figure 2.6 – Threshold behavior of the Fourier power $A^2_{\Delta\theta,\mathrm{Kittel}}$ of the Kittel mode.** (a) The external magnetic field can be used tune the observed characteristics between dipolar surface waves and uniform precession. (b) Determination of the critical magnetic field $\mu_0 H_{\mathrm{crit}}$ for different fluences $F = 5$ and $60\,\mathrm{mJ\,cm^{-2}}$, respectively. $A^2_{\Delta\theta,\mathrm{Kittel}}$ is plotted after normalization to the maximum of the respective Fourier spectrum for a given external field, $A^2_{\Delta\theta,\mathrm{max}}$. The result can be regarded as a measure of mode population and a linear increase is found prior to saturation. The critical field can be extracted as depicted by the vertical green lines. In the inset, corresponding results for all fluences are included, giving a clear trend towards smaller $\mu_0 H_{\mathrm{crit}}$ for increasing $F$. Additionally, the Kittel amplitude as induced by different pump fluences is shown for $\mu_0 H_{\mathrm{ext}} = 150\,\mathrm{mT}$ (gray points).

the optical excitation mechanism. A concept was developed taking into account the amplitude profile of the DE mode as well as the asymmetric excitation profile stemming from the laser pump pulses. However, the exact understanding of the DE wave vector is a challenge still to be met. The possibility of a periodic magnetic ripple pattern that imposes its periodicity onto the wave vector has been discussed. We tried to explain the transition from a well defined DE mode to a uniform precession mediated by the external field above a critical-field value of $H_{\mathrm{ext}} > H_{\mathrm{crit}}$ and we have pinpointed possible mechanisms. Only a non-linear process allows to explain the dependence of the transition field $H_{\mathrm{crit}}$ on the pumping power. In this context the high energy of the pump pulses driving the system far out of equilibrium leading to rather large precession angles should be mentioned, which is the most important experimental finding. In essence, the population of either the Kittel or the DE mode can be tuned by both the external field and the pumping fluence. Understanding the underlying mechanism might prove crucial on the way to spin-logic devices, especially with the interconversion of electrical, optical, or magnetic signals in mind.

One of the authors (J. H.) acknowledges financial support through the Grant Academy of The Academy of Sciences of the Czech Republic (Grant No. KAN-

400100653). Also, fruitful discussions with A. Slavin and B. Hillebrands and the contribution of the Kerr microscopy by C. Patschurek and R. Schäfer from the IFW in Dresden are gratefully acknowledged.

## Chapter 3

# The building blocks of magnonics

B. Lenk, H. Ulrichs, F. Garbs, M. Münzenberg

Physics Reports **507**, 107–136 (2011)
DOI: 10.1016/j.physrep.2011.06.003

**Abstract.** Novel material properties can be realized by designing waves' dispersion relations in artificial crystals. The crystal's structural length scales may range from nano- (light) up to centimeters (sound waves). Because of their emergent properties these materials are called metamaterials. Different to photonics, where the dielectric constant dominantly determines the index of refraction, in a ferromagnet the spin-wave index of refraction can be dramatically changed already by the magnetization direction. This allows a different flexibility in realizing dynamic wave guides or spin-wave switches. The present review will give an introduction into the novel functionalities of spin-wave devices, concepts for spin-wave based computing and magnonic crystals. The parameters of the magnetic metamaterials are adjusted to the spin-wave $k$-vector such that the magnonic band structure is designed. However, already the elementary building block of an antidot lattice, the singular hole, owns a strongly varying internal potential determined by its magnetic dipole field and a localization of spin-wave modes. Photo-magnonics reveal a way to investigate the control over the interplay between localization and delocalization of the spin-wave modes using femtosecond lasers which is a major focus of this review. We will discuss the crucial parameters to realize free Bloch states and how, by contrast, a controlled localization might allow us to gradually turn on and manipulate spin-wave interactions in spin-wave based devices in the future.

## 3.1 Introduction

Magnonics is a young and evolving research field. Its aim is to control and manipulate spin waves in ferromagnetic materials [KDG10]. In analogy to photonics taking control of the flow of light, it allows for the design of material properties for spin waves. The experimental realization of computing with spin waves will be discussed first. These are logic gates (NOR, XNOR, etc.) – novel devices that benefit from the particular properties of spin waves. To connect and to guide information, spin-wave frequency filters and wave guides are under research. In such, novel computing concepts have been described. One of these are reconfigurable mesh structures using spin waves for parallel graphics computing. This review will introduce how periodic structures can be realized in different dimensions which will determine the line, plane or volume in which the artificial material properties are tailored and affect propagating spin waves. A large part of the present review will map how they can be investigated using laser light – hence the term photo-magnonics – a technique developed in the last years. In particular, two-dimensional structures will be considered.

Generally, the response function to a dynamic excitation propagating through a periodic crystal determines its propagation defined by the dispersion $E(\boldsymbol{k})$ which in turn determines the available density of states. For weak potentials, the concept of constructing Bloch states using plane waves and calculating their dispersion in the reduced zone scheme is straightforward. Applied to photons in periodic dielectrics, we show how band gaps at the Brillouin zone boundary tailor novel functionalities.

In the case of spin waves, the dispersion can be quite complex in the unstructured materials; we give a short introduction to the peculiarities of the spin-wave dispersion, namely the anisotropy of the dispersion with respect to the magnetization direction. The same concepts as for electrons and photons can be applied to magnons to form Bloch states in a magnonic crystal. In the uniform-mode approximation simple band structures can be directly calculated. However, these ignore the detailed shape of the potential and are a good approximation for a weakly varying potential only. A more realistic potential landscape will be discussed in the case of the periodic dipolar potential for a simple antidot lattice. The individual shape of each spin-wave scatterer, the building block of the magnonic crystal, is determined by its detailed variation of the dipole field.

Spin-wave modes in periodically structured materials have been studied experimentally by different techniques: microwave-based techniques (ferromagnetic resonance (FMR), vector network analyzer FMR or pulse-inductive microwave magnetometer (PIMM)), in combination with spatial-resolved Kerr microscopy. A somewhat larger part will be devoted to optical pump-probe techniques with femtosecond lasers in this review. The interplay between localization and delocalization of the dynamic modes in the magnonic crystal is shown to be crucial to understand the observed spin-wave modes. The deep distortion of the internal field by the dipole field at an antidot site results in a localization of the spin waves in many cases, prohibiting the observation of delocalized modes. However, in order to realize magnonic wave guides and active spin-wave materials, it is crucial to control the interplay between localization and delocalization of the dynamic modes in the magnonic crystal. For a high filling fraction of the antidot lattice (i.e. amount of material removed), spin waves are trapped over a large field range at places with reduced internal field in the magnonic crystal. Generally, only for small filling fractions delocalized free Bloch modes are observed, whose $k$-vector is determined by the crystal's unit cell. We will discuss how these Bloch modes can be identified in photo-magnonics. At the end we will give a short outlook on future possibilities, perspectives and developments in the field, such as guiding spin waves in magnonic wave guides, spin-wave resonators or tuning the degree of localization of a spin wave and their interaction.

## 3.2 Computing with spin waves

On the semiconductor roadmap of 2009, possible emerging research devices and emerging materials for future electronics and logic are presented [Sem09]. On the materials side, graphene, carbon nanotubes, and nanowires are discussed as possible candidates to develop materials to meet requirements for future semiconductor devices. On the device side, the use of the electron spin for information storage, and the implementation of spin waves for performing non-volatile logic functions on a CMOS chip are discussed. The idea to use waves for signal processing is not new: light in glass fibers is used as an interconnect between chips in powerful computers. The IBM blue gene super computer link modules have optical circuits on each board. However, their function is to convert electrical signals into optical signals that can be directed to the next step of data processing. As long as the processing relies on electrons, the extra effort of transforming the data into light pulses for effective and fast throughput to other regions of the processor is unavoidable. Building a computer that uses solely photons for information processing and its non-volatile logic functions is not that easy a task. It is difficult to realize a light switch that can be operated by light; to switch light, one would need to modify the index of refraction which is related to the electron density of the material. Consequently, a high density of photons is needed to have a significant effect on the dielectric properties of a material. To realize a switch that should turn on and off the total number of photons, certain tricks have to be played. We will discuss in section 3.3.4 the progress in this area briefly.

How is it possible to take advantage of the properties of spin waves, the intrinsic strong non-linearities to realize switches for spin waves and to realize non-charge-based persistent devices for spin-wave based computing? In recent years, a large portion of the effort of the magnetism community was devoted to the field of spin electronics, to develop spin-based semiconductor devices for spin-based transistors and spin-based logic. Magnetic random access memories (MRAMs) have been developed that exploit the advantage of non-volatile memory storage, while reducing power consumption. Power consumption is one of the biggest problems of high integration circuits today, because of the heating of the chip, reduced battery lifetimes and environmental harmfulness. The idea of looking at spin waves stands to reason, which has, however, not been done until recently. Even though spin waves have been studied as narrow frequency filters from the 60s to the 80s in YIG-based high frequency devices [Rod88, Gla88, Ada88, Ish88, Sch88, SAC76], the idea to use spin waves for data transmission and processing is very new. It can be realized with control on the nanometer scale by now and will be discussed in section 3.5. What makes spin waves favorable for technological applications is the corresponding index of refraction which can easily be manipulated. The term 'index of refraction' should here be understood in analogy to photonic crystals where optical resonances can be shifted by a periodic modulation of the dielectric constant.

In the ferromagnetic case, the modulation may be in the parameter exchange constant ($A$) and/or saturation magnetization ($M_\mathrm{S}$), while an additional directional asymmetry is introduced by the applied magnetic field. Corresponding Bloch-like resonances of the spin-wave spectrum will be discussed in section 3.5.3. In general, spin-wave frequency and wave length can both be tuned from MHz to THz on micron to sub-nm scales, respectively. Therefore, the use of spin waves for logic devices is the natural extension of magnetic non-volatile elements for storage. The flexibility of spin-wave based materials opens up the possibility of a spin-wave based computing architecture. This is the underlying idea of magnonics: to use spin waves for power-saving computing. Nevertheless, certain prerequisites in manipulating and guiding spin waves have to be demonstrated a priori [DDB$^+$09, DJD$^+$09, KBW10b]: (i) the controlled excitation of spin waves at defined frequencies, (ii) guiding spin waves in magnetic wave guides and (iii) active spin-wave devices for spin-wave manipulation and information processing.

### 3.2.1 What are spin-wave guides?

An object often referred to as a spin-wave guide is a (quasi) one-dimensional strip of ferromagnetic material. Through its physical boundaries, it restricts the region of existence for spin waves. In optics, an analogue object is called a fiber. Different from glass fibers in optics, a spin-wave guide is a homogeneously magnetized wire that can channelize, split, and manipulate submicrometer-width spin-wave beams, as was shown by Demidov and Demokritov [DJD$^+$09]. The differences are depicted schematically in figure 3.1 where the properties of a graded index glass fiber are compared to a magnetic wave guide. In the graded index glass fiber, the index of refraction gradually increases to the outer shell of the glass fiber having a higher index. The light is totally reflected and conducted in the core of the fiber. The gradual transition leads to a smooth curvature of the wave fronts so that

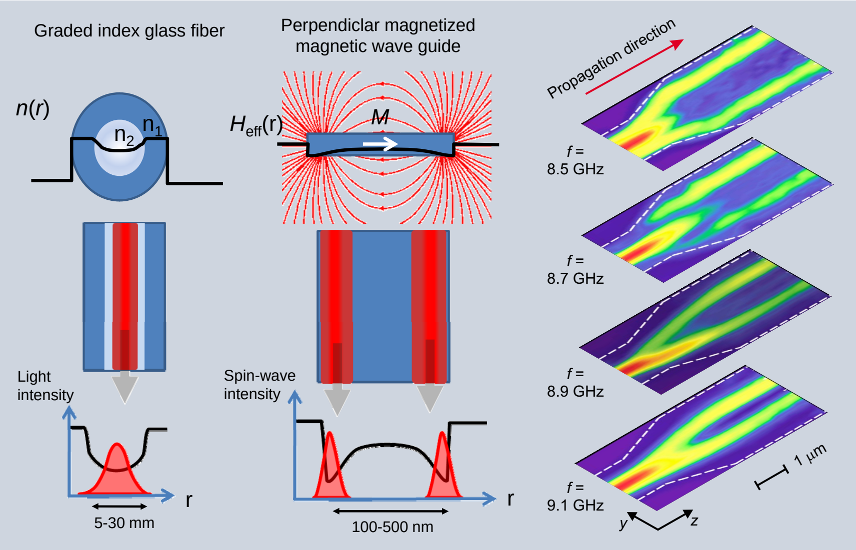

**Figure 3.1 – Comparison of optical and magnetic wave guides.** A graded index glass fiber (left column) concentrates the intensity of the light modes in the area of low index of refraction, i.e. small dielectric constant (depicted by a solid black line). In a simple, homogeneously magnetized plane magnetic wire (center column), the internal effective field (solid black line) determines the localization of the spin-wave modes. Localization of spin waves along a spin-wave guide (right column) measured with micro-BLS (Brillouin Light Scattering) (adapted from reference [DJD$^+$09]). The internal field changes as the width of the wire changes, resulting in different localization axes of the beam path.

the Gaussian shape of the intensity profile and temporal coherence of the signal pulse is only slightly distorted. The index of refraction, arising from the dielectric properties of the materials, serves as a potential landscape for the light wave.

For a spin wave, the situation is sketched in the middle of figure 3.1. A flat, structured strip with a width in the micron range serves as a spin-wave guide. The details of propagation depend on the magnetization direction: magnetized in-plane perpendicular to the wire axis, Damon-Eshbach modes that are a species of dipolar spin waves (see section 3.4.1) can travel along the wire. Magnetic charges at the boundaries lead to a decrease of the internal magnetic field in the wire at both sides; i.e., due to the demagnetization field of the wire magnetized perpendicular to the wire axis, the effective field is reduced at the edges of the spin-wave guide (see sketch in figure 3.1). The well structure of the internal field shows minima at both sides of the wave guide. Depending on the width of the strip, the internal magnetic field in the center of the stripe is also diminished more or less in strength for smaller or wider wave guides. One can excite modes, which are localized in these wells – so-called ‘edge modes’, as well as modes in the middle of the wave guide – so-called ‘center modes’. In this context, it is important to notice that edge-modes always have lower frequencies, as compared to center modes.

The right panel in figure 3.1 shows micro-Brillouin Light Scattering (µ-BLS) maps of such modes. Spin waves are excited in the region with smaller width, and thus a stronger reduced internal field at the center. They propagate towards the region with increased width and thus increased internal field in the center. A transformation from a center into an edge-mode takes place in the transition zone. Due to the upward shift of the spectrum in the wider strip, the excited wave can no longer exist in the center. This localization process depends on the frequency of the initially excited mode: for higher frequencies, the edge-modes move towards the center. This example nicely shows that the understanding of and control over the spin-wave dispersion, localization, and delocalization with the internal field distribution is one of the key aspects to progress in this novel sub-field.

### 3.2.2 Spin waves on a chip: Reconfigurable mesh design

Concepts to use spin waves for data processing in a chip have been developed by Kang Wang et al., a short review on spin-wave based computing has been published in the series of the first "International Seminar and Workshop Magnonics: From Fundamentals to Applications" held in August 2009 in Dresden [KBW10b] based on their earlier work published in references [KW05, KNB$^+$07]. Many current applications require a vast amount of data to be processed in parallel. A typical example is a graphic chip, with its algorithms for parallel image processing. Their architecture and computation power has been increased enormously in the last decade. From the scientific point of view, numerical simulation programs which can be parallelized, can take advantage of the significant progress in that field, so when put together, an array of graphic chips makes a new super computer.

The idea of the spin-wave based computing concept to parallelize computation uses a reconfigurable mesh architecture. Spin-wave guides transmit the signal at each line. The chip consists of a mesh of $N \times N$ spin-wave switches interconnected by ferromagnetic spin-wave guides. Each node is realized by a ferromagnetic switch. If the switch is "on", the spin wave is guided into the crossed line to the spin-wave buses' output. The switching frequency is in the order of GHz and transmission speed is $10^4\,\mathrm{m\,s^{-1}}$, allowing fast data processing. In the architecture presented in references. [KW05, KNB$^+$07, KBW10b], excitation is realized by a strip-line; detection will be realized by inductive detection at a second strip-line.

The spin-wave switch at each crossing could be realized by a diluted magnetic semiconductor which can be switched from a ferromagnetic to a paramagnetic state by applying positive or negative voltages. It should be remarked that as of today, this concept is lacking a realistic practical implementation. Ferromagnetic

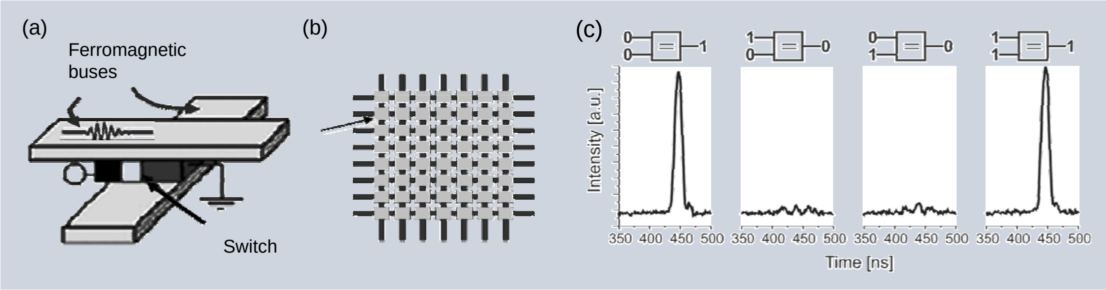

**Figure 3.2 – Concepts and first realization of spin-wave based computation.** (a) Schematics of a spin-wave bus, and (b) building blocks of a reconfigurable mesh structure (from references [KW05, KNB+07]). (c) Experimental realization of XNOR functionality (logic equality) using a spin-wave interferometer with phase shifter as reproduced from reference [SSL+08].

semiconductors like Mn-doped GaAs have both a very strong spin-orbit interaction and a critical temperature that is below room temperature, and hence will not work for actual devices. However, using a mesh structure allows for large image data to be processed in the reconfigurable nodes. This is a typical application needed for example to process image data for compression in a television graphics chip. Additionally, different to a standard reconfigurable mesh design, spin-wave buses could in principle address different frequencies. Therefore, parallel operation seems possible as well. The layout is shown in figure 3.2. In (a), the schematic layout of one node is shown which can be addressed by the voltage turning on/off the magnetization, which then guides the spin-wave package to the lower magnetic wave guide. In (b), the full layout of the mesh structure is depicted.

### 3.2.3 Elements of spin-wave computing and logic

At the same time as concepts that take advantage of spin-wave computing have been put forward, spin-wave based logic elements have been demonstrated. Their principle relies on a spin-wave beam splitter. Two spin-wave packets of the same amplitude are split into different arms of a spin-wave guide. In one arm, the propagating spin wave receives a phase shift by 180° ($\pi$). The arms are united and both spin waves interfere destructively. This can be compared to a spin wave Mach-Zehnder-type interferometer.

Different realizations for phase shifters have been suggested; for example, in micromagnetic simulations, it was shown that a domain wall could be utilized as a phase shifter in one of the interferometer arms [HWK04]. More generally, the phase shift, slowing down or acceleration in one interferometer arm relative to the other, depends on the dispersion of the spin wave. The dispersion is naturally modified by the (sometimes complicated) magnetic structure of the domain walls, thus the average internal field in the domain wall.

Another possibility is to shift the frequency by locally applying an external magnetic field. In the yttrium iron garnet (YIG) wave guides, which have the lowest damping of any magnetic material, millimeter propagation length of spin waves in the microwave frequency range can be realized. In these systems, spin-wave propagation, spin-wave amplification, spin-wave pumping, phase shifters, interferometers and filters were demonstrated [SSL+08, SSHK08]. Schneider and coworkers developed in these wave guides a spin-wave logic realizing exclusive-not-OR and not-AND gates based on the Mach-Zehnder-type interferometer which will be presented in more detail. Input and output into the YIG wave guides is implemented by microwave antennas; the signal is propagated in two YIG arms of the interferometer. The phase shifter is realized by applying an Oersted field on top of the YIG, which changes the carrier wave number of the spin-wave packet within that region. By changing the amplitude of the Oersted field, the phase shift can be chosen to sum up to one half of a wavelength. The output signal is shown in figure 3.2(c). If no field is applied at either arm, both spin-wave packets are equal in phase and the full signal is detected. If for any of the arms the relative phase is shifted (input 0,1; 1,0), the signals detected at the microwave detection antenna have opposite signs and cancel out. The output signal is zero. If both arms are subject to an Oersted field, both spin waves are shifted by the same phase, and again, the full signal is measured at the output. This gives the functionality of an XNOR logic device (logic equality).

A second logic device functionality is implemented by using the Oersted field on top of the YIG arm to completely suppress the propagation (spin-wave switch), which gives a zero transmission (output 0) if both inputs are on (input 1,1), else (input 0,0; 0,1; 1,0) a signal is detected (output 1), which is the NAND functionality. The disadvantage of YIG-based magnonic devices is that YIG cannot be integrated into standard semiconductor technology because high quality YIG films cannot be grown on silicon at the moment, but special substrates are needed. The industrial demand of miniaturization and integration into semiconductor technology is much better met by Permalloy ($Ni_{80}Fe_{20}$). This is why the aforementioned concepts need to be transferred to smaller structures.

In figure 3.3, Wang et al. compare MOS logic and magnonic logic in terms of throughput (the number of operations per area per time) as a function of the minimum feature size $\lambda$ which is the gate length for CMOS or the wavelength for a spin-wave circuit, respectively. The throughput in devices realized so far is quite small and feature sizes lie in the micrometer range. However, according to the projected estimates, spin logic may provide a throughput advantage of

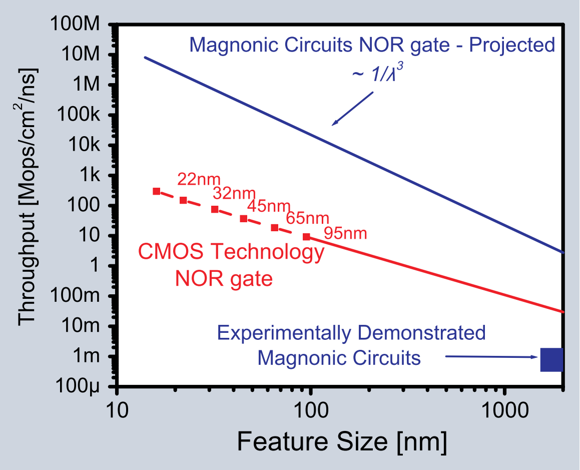

**Figure 3.3 – CMOS technology scaling versus spin-wave based magnetic circuits.** From [KBW10b]. For spin-wave circuits, the number of operations per area per time (throughput) scales inversely proportional with the minimum feature size (wave length) $\lambda$.

more than three orders of magnitude over CMOS in the future. Magnonic logic has several scaling advantages, one being the inversely proportional throughput of the spin circuit to the wavelength. However, scaling down to spin-wave length in the nanometer range is in first order a material problem: one has to find materials where the damping of spin waves is low [LMC+09]. Half metals are an ideal candidate here, since electron and spin scattering channels can be decoupled [MWD+09].

## 3.3 Tailoring artificial materials

To realize devices described in the previous section, it is most convenient to microscopically manipulate the properties of a single material. This is the origin of the success of the semiconducting materials as silicon which has a band gap at the Fermi level. Thus, no states are available for conduction inside the gap region. To design the electronic properties, doping is necessary. The potential landscape is then formed by a combination of differently doped regions and various devices such as transistors can be realized to switch current flow through a device on and off. It is the flexibility of the material that allows a change in the conductivity by orders of magnitude and allows the shaping of the density of states at well-defined energies with a spatial precision down to nanometers. The band gap and a controlled introduction of defect states defines this flexibility. In a similar manner, photonic materials can be designed (see figure 3.4).

Spectacular examples are materials with negative index of refraction [Ves68], photonic band gap materials already existing in nature giving it its colorful life, and controlled 'defects' realizing high quality resonators for light waves. These materials own novel properties that are very different from those of their con-

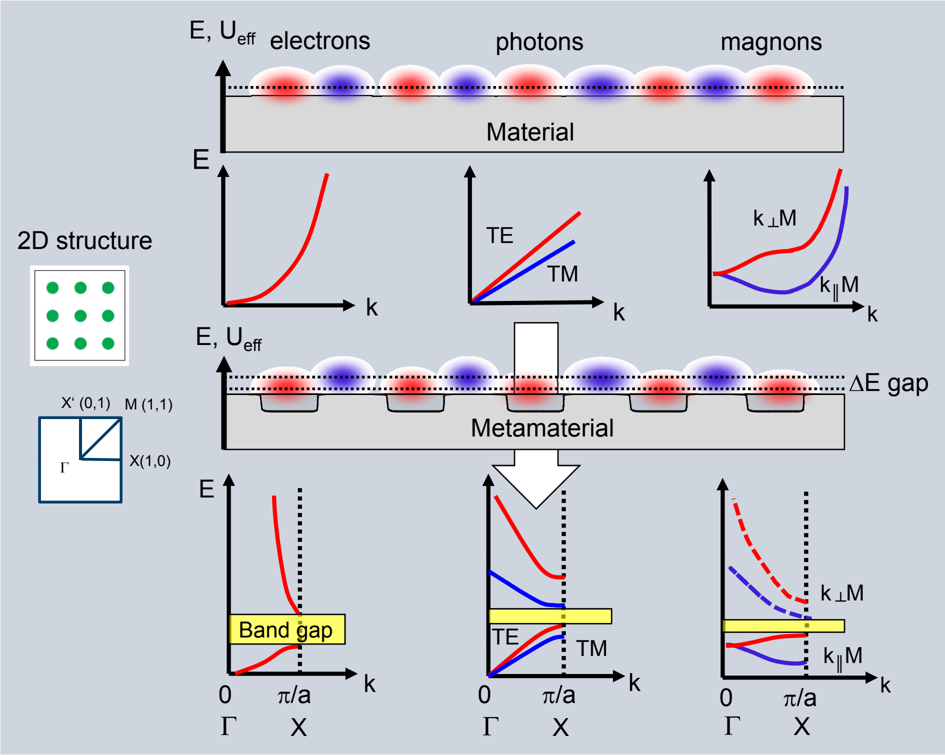

**Figure 3.4 – Schematic analogy of electrons, photons, and magnons in periodic potentials.** The dispersion is shown in the reduced zone scheme. Different dispersions result in characteristic differences in the band structure. A common feature is the possibility of the formation of band gaps. The polarization (transverse electric (TE) or transverse magnetic (TM)) for photons and the propagation direction $k$, with respect to the applied magnetic field for magnons (parallel or perpendicular), are additional free parameters determining the band formation for the latter (the $k$-scale is logarithmic for magnons).

stituents. Any wave propagating probes a material with effective parameters designed by structure and composition. Therefore, metamaterials are per definition artificial materials where the periodicity of the structure is smaller or equal to the wavelength. This can be centimeter or millimeter in size: first metamaterials have been realized for microwave radiation [SPW04]. Artificial materials also include those acting on water waves [HC05], which allow the formation of refractive elements like lenses and sonic waves, to realize sonic crystals with negative refraction [FLL+06]. These examples from other areas utilize rather macroscopic waves transmitted through the metamaterial.

In the following, we will remind the reader of the basics of band structure formation in metals and covalent bonded materials. As a next step we will apply this formalism to photons in a periodically structured material with alternating index of refraction before we expand the formalism to magnons.

### 3.3.1 Bloch conditions and band structure: weak periodic potential

In a metal, the free electron ansatz is very successful, leading to Sommerfeld equations describing transport in an electron gas. The kinetic energy dominates the properties of the electrons. The energy levels are filled homogeneously up to the Fermi level leading to a Fermi sphere in momentum space, which behaves isotropic for the different directions. The Hamilton operator is given by

$$H = H_{\mathrm{kin}} + V(\boldsymbol{r}).$$

The solution for the free electrons where $V(\boldsymbol{r})$ is neglected, is simply given by a quadratic dispersion mirroring the increase of kinetic energy

$$\psi_k = e^{i\boldsymbol{kr}}, \quad E = \frac{(\hbar k)^2}{2m}.$$

Turning on a periodic potential, the Bloch theorem allows us to exploit the periodicity. The solution can be separated into two parts: a free electron propagating part with wave number $k$ and a function that is periodic with the lattice $u_{n,k}$. The new quantum state is described by a wave number $k$ and a band index $n$,

$$\begin{aligned} V &= V(\boldsymbol{r} + \boldsymbol{R}), \\ \psi_{n,k} &= e^{i\boldsymbol{kr}} u_{n,k}(\boldsymbol{r}). \end{aligned}$$

The periodic function $u_{n,k}$ describes the electron distribution within one cell around the crystal atom. Without making any calculations of the exact band structure, already some general conclusions regarding the electron states in the resulting band structure can be drawn. As a consequence of the periodic potential, the electron dispersion mirrors the symmetry of the lattice. Gaps open up especially around the zone boundary in the high symmetry directions. This can be seen in figure 3.5 (middle) where, for a weak potential, the opening of the gap at the zone boundary is given.

The periodic functions $u_{n,k}$ and their eigen energy $E_{n,k}$ have to be calculated. To do this for a given potential, the plane wave ansatz $\exp(i\boldsymbol{kr})$ is used to make a Fourier expansion for the wave function. It is most convenient to solve the set of Bloch states in $k$-space via the Fourier transform of the Schrödinger equation. Then the Fourier coefficients of the periodic potential $V$ determine the coefficients of the Fourier expansion of the wave function. This directly allows the calculation of the band gap: it is given by $2|V_G|$ where $V_G$ is the Fourier component of the

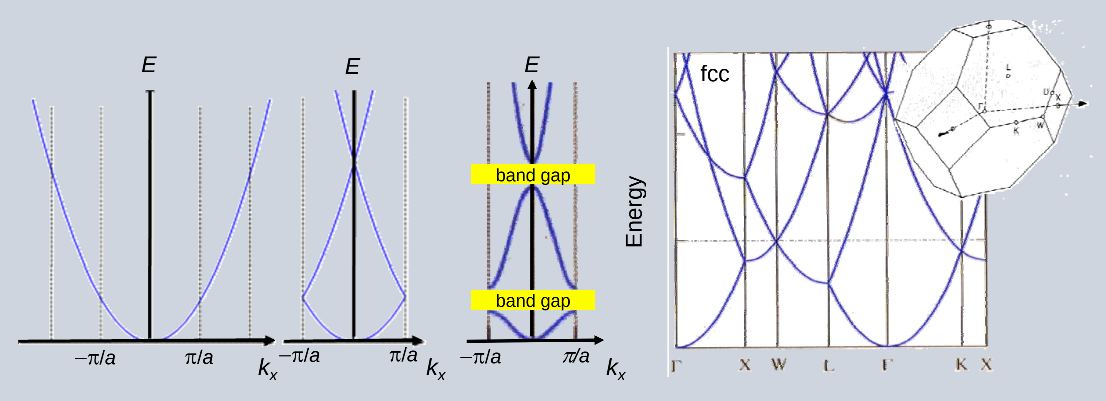

**Figure 3.5** – Free electron band structure (left) in the periodic boundary scheme and reduced zone scheme. In a weak periodic potential a band gap opens up (middle). It is given by $2|V_G|$ where $V_G$ is the Fourier component of the periodic potential. Free electron band structure (right) for a fcc-lattice along the main symmetry directions (adapted from reference [Hun07]).

periodic potential at the zone boundary $\boldsymbol{k} = \boldsymbol{G}$. In fact, we will see in section 3.4 that for spin-wave states, similar approaches to calculate their band structure can be used, however, also with distinct differences arising from the different equations of motion including the symmetry of dipolar interactions mirrored by the vector nature of the magnetization $\boldsymbol{M}$.

### 3.3.2 Electrons in a strong periodic potential

If the electron wave function possesses a localized nature, the free electron approach is not successful. The electronic band structure of such a material mirrors more strongly the orbital nature of the atomic wave functions. The $s$,$p$,$d$-like symmetry determines many of the fundamental properties of the material. Examples are band ferromagnets, where the flat $d$-like electron bands are responsible for the formation of the ferromagnetic order [KÖ0]. Other examples include carbon, silicon and germanium of the group 4 elements in the diamond structure. The local electron density is described by the linear combination of s and p wave functions forming the $sp^3$ tetraeder structure. In that case, another possibility is to take the atomic wave function of the single atom as a basis to construct the bands. Typically, a Wannier function localized on an atom, but with decaying density of states to the neighboring atom, is used. The band width is given by the overlap to the next atom. A large overlap means a large hopping rate and a strong delocalization and consequently a large bandwidth. The more localized the electrons are on the atomic-like orbitals, the smaller is the overlap and the smaller is the band width in energy.

One can derive these tight binding bands for different crystal symmetries (fig-

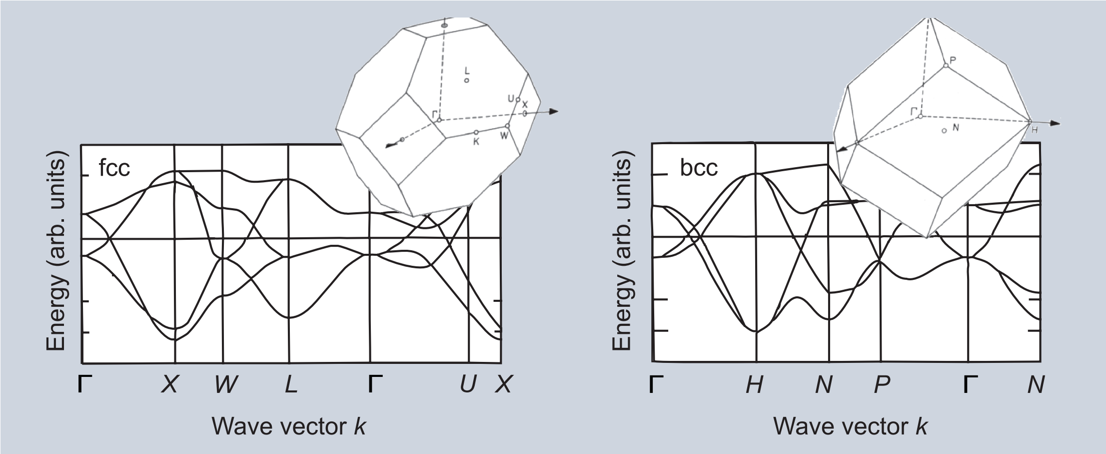

**Figure 3.6 – Canonical tight binding *d*-band structure for fcc and bcc lattice along the main symmetry directions.** The band width $\omega_d$ of the cosine-like bands is given by the overlap $t_d$ of the atomic orbital functions (here *d*-orbitals) into the different crystal directions $\sim 2\sqrt{N_{nn}}t_d$. The overlap $t_d$ determines the delocalization of the electrons within the band. The symmetry is determined by the underlying atomic wave functions admixture (adapted from references [Hun07, KÖ0]).

ure 3.6 for bcc and fcc). For example, in the bcc case, the splitting into the $d_{\mathrm{xy}}$, $d_{\mathrm{xz}}$, $d_{\mathrm{yz}}$ symmetry and $d_{3\mathrm{z}^2-\mathrm{r}^2}$, $d_{\mathrm{x}^2-\mathrm{y}^2}$ symmetry are observed varying from a different distance to the next neighbor atom along the axes of the cube and along the diagonal. The band width of the $d_{3\mathrm{z}^2-\mathrm{r}^2}$, $d_{\mathrm{x}^2-\mathrm{y}^2}$ bands is increased by a factor of 1.5 along the $\Gamma$-$X$ symmetry direction. The symmetry of the atomic wave function in connection with the lattice symmetry determines the electron states observed in the crystal; even though the states are strongly determined by their atomic wave functions and show a weaker dispersion, the next neighbor distance significantly influences the properties of the electron in the band such as localization. We will see here the similarities to the magnonic systems, where spin waves can also be of localized nature later and its symmetry is mirrored by a short range interaction.

### 3.3.3 Photonic crystals – photons in periodic potentials

Similar to the periodic potential experienced by electrons around ion cores in a lattice, in a photonic crystal the periodic dielectric properties determine the periodic confinement for the photons. In general, if the potential varies periodically for a wave traveling through a two-dimensional artificial crystal, one can obtain a solution by labeling the modes with their band index $n$ and wave vector $\boldsymbol{k}$ using Bloch's theorem, as described for the electrons before. The same concepts can be applied despite the equation of motion being determined by the wave equation derived from the Maxwell equations.

Equal to the periodic potential of the positive ion cores $V_U$ in the solid state for electrons, for a photonic material the dielectric properties $\varepsilon$ determine the refractive index, which determines the periodic confinement for the photons $V_\varepsilon$ [JJWM08]. To compare: in a magnonic material, the dispersion will be dependent on the local magnetization direction $V_M$ and the induced internal field. In many cases, photonic structures are two-dimensional. The mathematical ansatz to describe the electro-magnetic modes of a photonic crystal is similar to the description of delocalized electronic states in solids. The wave traveling through a two-dimensional artificial photonic crystal experiences a periodically varying potential arising from the dielectric constant $\varepsilon$. In two dimensions the potential $V_\varepsilon$ varies as

$$V_\varepsilon = V_\varepsilon(\boldsymbol{r} + \boldsymbol{R}),$$

where $\boldsymbol{R}$ is a linear combination of the primitive lattice vectors for a two-dimensional array in the $x$-$y$-plane. Using Bloch's theorem and using $\rho$ as the projection of $\boldsymbol{r}$ in the $x$-$y$-plane, one obtains a solution labeling the modes with their band index $n$ and wave vector $k_\parallel$:

$$\psi_{n,k_z,k_\parallel} = e^{ik_\parallel \rho} e^{ik_z z} u_{n,k_z,k_\parallel}(\rho).$$

One example taken from [JJWM08] is given in figure 3.7. It has been calculated for a two-dimensional array of aluminum columns with the dielectric constants of Al ($\varepsilon = 8$) and air ($\varepsilon = 1$). In the case of an electro-magnetic wave, one has to distinguish two solutions in the two-dimensional crystal. For a photon propagating through the crystal, the electric field can be polarized in the plane or out of the plane of the two-dimensional structure.

Therefore, different dispersions are found for transverse electric (TE) and transverse magnetic (TM) polarization to the plane of the crystal: TE and TM modes show a different slope at the $\Gamma$-point. The TM-mode shows a lower velocity because it effectively sees the higher dielectric constant of the Al columns. The corresponding modes at the zone boundary along the different symmetry directions at the $X$- and $M$-points are plotted to the right: they form standing waves which are localized either at the Al columns or in between. The one with lowered energy is localized in the areas with high $\varepsilon$ and the one with increased energy in the areas with low $\varepsilon$, leading to distinct gaps in the photonic band structure in this direction. It can be easily understood that the gap is larger for the TM modes for the same argument that this mode, since its $E$-vector is in the plane, is strongly affected by the alternating dielectric constants.

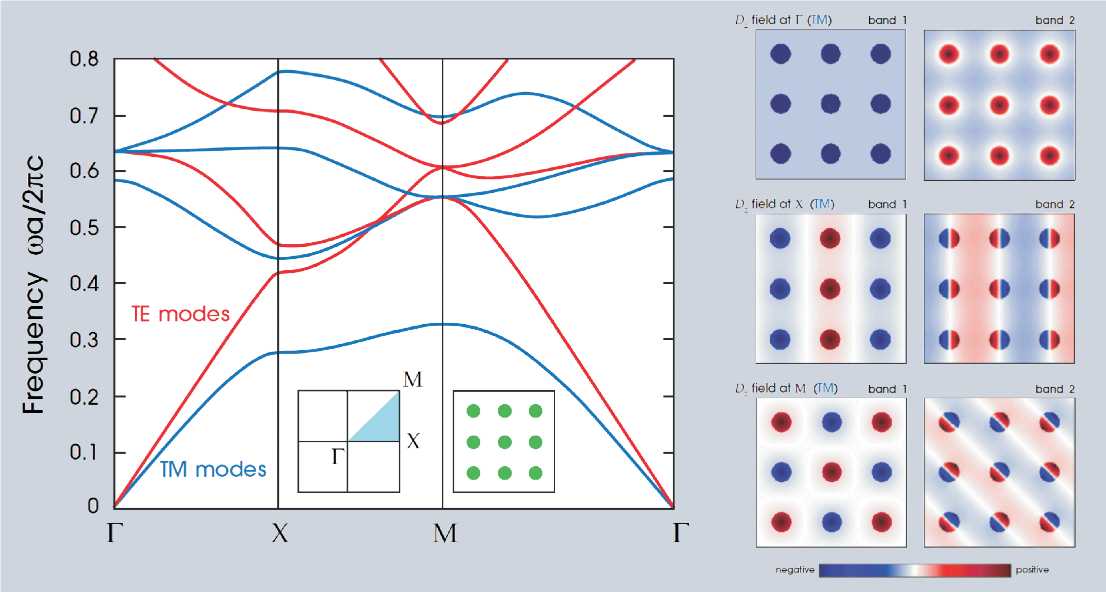

**Figure 3.7 – Photonic band structure calculated for an array of two-dimensional Al columns.** Transversal electric (TE) and transverse magnetic (TM) modes show a different slope at the $\Gamma$-point. The TM-mode shows a lower velocity because it effectively sees the higher dielectric constant of the Al columns. Shaded areas mark the split bands at the high-symmetry points. Right: At the zone boundary for the different bands, the standing waves with high and low energy are plotted (Al ($\varepsilon = 8.9$) in air ($\varepsilon = 1$)) (adapted from reference [JJWM08]).

### 3.3.4 Novel functionalities of photonic crystals: slow photons

A designed photonic band structure can be used to achieve novel optical properties. Quite generally, close to the zone boundary, the band flattens out. Approaching the zone boundary then means in terms of group velocity given by $d\omega/dk$, that the photon is "slowed down" as depicted in figure 3.8 [Bab08, Kra08]. Usually switching light by light is not possible: the change in the index of refraction is only small. However, when using slow light, a trick can be applied. Exploiting the sensible reaction to the refractive index in the region where the band flattens out, it was experimentally demonstrated that it is feasible to guide light from one wave guide to another output, which is the realization of an ultrafast nanophotonic switch using slow light [KBKK09, KBW$^+$09]. In detail, the spatial beating due to odd and even super-modes in two parallel wave guides is used for rerouting triggered by a femtosecond laser pulse.

This shows that a wave guide in a photonic material is not only a straight line of material conducting light as a glass fiber: the peculiar properties can be designed by the photonic structure around the wave guide giving the light completely new properties in the artificially structured material. We suggest it should be one aim

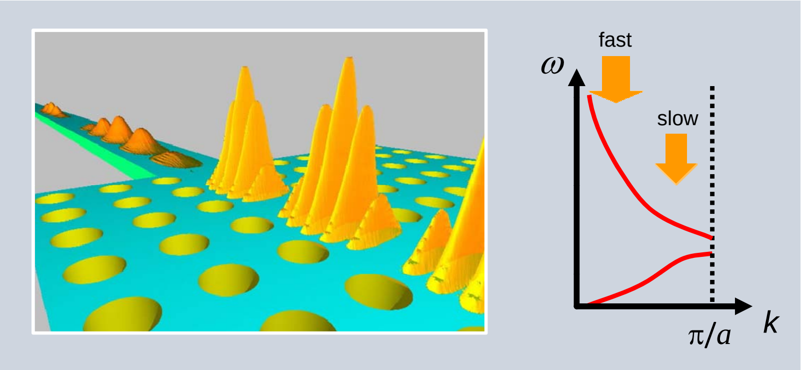

**Figure 3.8 – Photons entering a wave guide.** In the wave guide, the pulses are compressed and their intensity increased. The wave vector is close to the zone boundary and their propagation speed is slowed down (from reference [Kra07]).

in magnonics to put forward similar concepts to exploit the full possibilities of artificially structured materials for spin waves.

## 3.4 Magnonic crystals – spin waves in periodic potentials

We will now in more detail discuss the effect of structuring a magnetic film to form a magnonic crystal. That is, only two-dimensional systems are taken into account and beginning with a continuous film, the effects of periodic structures are considered on an analytical as well as numerical level. We will show that for the dipolar modes, the dispersion differs for different propagation directions $\boldsymbol{k}$ relative to the magnetization vector $\boldsymbol{M}$. Namely, the Damon-Eshbach ($\boldsymbol{k} \perp \boldsymbol{M}$) and the backward volume mode ($\boldsymbol{k} \parallel \boldsymbol{M}$) exist, which are different due to dipolar interactions. As a consequence, the spin-wave states in a square magnonic crystal have a lower symmetry than the underlying lattice structure. The manipulation of the local magnetization direction or an applied field on a nanometer scale allows active dynamic control of the spin-wave diffraction on the nanometer scale. Thus, a rotation of the magnetization relative to the lattice changes the energy landscape dramatically.

### 3.4.1 Spin-wave dispersion from nanometer to micron range

Before we discuss the propagation of spin waves in a structured medium, in analogy to the preceding chapters on electrons and photons in periodic potentials, we first have to say some words to the equation of motion for spin waves to be solved in the periodic environment. In a continuous, non-periodic system, the magnetization follows the Landau-Lifshitz-Gilbert equation of motion, which reads

$$\frac{d\boldsymbol{M}}{dt} = -\gamma\mu_0 \boldsymbol{M} \times \boldsymbol{H}_{\mathrm{eff}} + \frac{\alpha}{M_S}\left(\boldsymbol{M} \times \frac{d\boldsymbol{M}}{dt}\right). \tag{3.1}$$

We will only consider a field applied in the plane of the film. The case of perpendicular magnetization is technologically less favorable since it demands strong fields for saturation, and it is also physically less interesting because the spectrum is isotropic. In the macrospin approximation, all the individual spins are considered to precess in phase and the thin-film solution to equation (3.1) is given by the Kittel equation

$$\left(\frac{\omega_k}{\gamma\mu_0}\right)^2 = H_x\left(H_x + M_S - \frac{2K_z}{\mu_0 M_S}\right). \tag{3.2}$$

Here, $K_z$ represents an effective anisotropy in the out-of-plane direction. If one allows for solutions to equation (3.1) other than uniform precession, it becomes important to distinguish two different interactions coupling magnetic moments or individual spins, respectively. The corresponding solutions will be discussed in the following sections.

### Dipolar spin waves

Solving equation (3.1) in the magnetostatic limit yields a manifold of dynamic solutions for a thin magnetic film of thickness $t$ [DE61, KS86, LEHM10]. All can be classified by their propagation direction with respect to the magnetization. Modes whose frequency lies above the one of the uniform precession generally tend to localize at the surface of the film and have a wave vector pointing perpendicular to the magnetization. The geometry with $\boldsymbol{k} \perp \boldsymbol{M} \parallel \boldsymbol{H}$ is identified as the Damon-Eshbach (DE) geometry [DE61]. The particular relation between the magnetic field and mode frequency is given by

$$\left(\frac{\omega_{\mathrm{DE}}}{\gamma\mu_0}\right)^2 = H_x\left(H_x + M_{\mathrm{S}} - \frac{2K_z}{\mu_0 M_{\mathrm{S}}}\right) + \frac{M_{\mathrm{S}}^2}{4}\left(1 - e^{-2|k_{\mathrm{DE}}|t}\right). \tag{3.3}$$

For directions $\boldsymbol{k} \parallel \boldsymbol{H}$, the so-called backward volume waves occur, with a reduced precession frequency compared to the uniform precession. This leads to a negative dispersion, as the waves travel “backward” in phase. In between, one finds a manifold of spin waves corresponding to the continuous change of angle from parallel to perpendicular (gray shaded region in figure 3.9). This peculiar energy dependence on the angle arises from the dipolar interactions. For wave lengths

**Figure 3.9 – Schematic spin-wave dispersion.** In the micron wave length (left), dipolar interactions dominate. The Damon-Eshbach and backward volume modes are shown. At an arbitrary angle in between further modes are found (gray shaded area). In the nanometer region (right), the dispersion shows cosine-like behavior. Here, the exchange interaction is dominant and can be approximated by a parabola for small energies. It intersects in a broad region of high-energy spin-waves excitation, where spin waves are heavily damped (red shaded area).

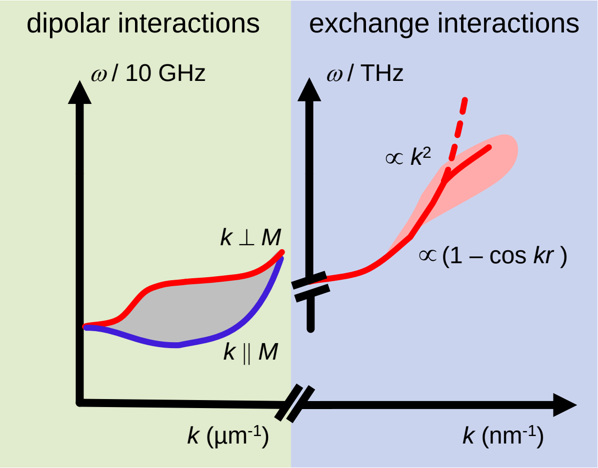

below a micron, the energy difference becomes smaller and both dispersions are degenerate in energy. Here, the exchange interaction becomes important, so that this contribution has to be taken into account for mixed dipole and exchange spin waves in an intermediate region of length scales [KS86]. The steep uprise of the energy for smaller wave length marks the dominance of the exchange interaction. In a thin film, the confinement perpendicular to its plane is dominated by the exchange interaction, while in lateral directions no such restrictions exist and dipolar magnetostatic spin waves may be formed.

### Exchange spin waves

Since spin-wave lengths span several orders of magnitude from tens of microns (even higher for low-damping materials) to below 1 nm, also their frequencies may vary from GHz to THz. In addition, the frequency for a given wave length can be shifted by the magnetic field. This broad region in length and time scales is one reason that makes spin waves so interesting for high frequency applications. However, also the dominating interaction varies: at wave lengths below 100 nm, the dispersion is dominated by the exchange interaction. The magnetostatic contribution to the energy of the wave can be neglected. This simple picture is solved in many solid states physics textbooks for a chain of precessing spins, where next neighbors are coupled by the exchange interaction. The solution is a $(1-\cos(kr))$ like behavior. As a consequence of neglecting the anisotropic dipolar contribution, the dispersion in the exchange limit does not change with the magnetization direction. It only depends on the next neighbor distance $r$ and the strength of the exchange interaction, and can be calculated in the 'frozen magnon' picture from the electronic structure. For small $k$, the dispersion can be approximated to a quadratic form. In that region, the energy increases quadratically with momentum $\hbar k$ similar to the free electron behavior. One can think of realizing 'free electron-like' magnonic materials.

At even higher energies, the spin waves approach the THz regime. Their energy gets comparable to single spin-flip excitations (Stoner excitations) between the bands of different spin character. These high-energy spin-wave modes in the THz range are heavily damped, indicated by the red shaded area. Dynamic excitations have to be thought of as a superposition of multiple spin excitations propagating through the ferromagnet [CMM04, HE73]. Life times of these high-energy spin waves of nm length scales are a few picoseconds before the decay into other spin-wave excitations of lower energy [DM07]. Investigated heavily in the 80s [BMC85, CLD80, PMMS88], their physics have drawn new interest. They are thought to be the key to the further understanding of ultrafast demagnetization processes after femtosecond laser excitations. Because of their short wave length and lifetime, at the moment, these are not suited for studies of the formation of magnonic bands. They propagate only a few nanometers. In the following, we will discuss the formation of magnonic band structures in the dipolar region.

### 3.4.2 Band structures of magnonic crystals

In this section we will discuss first what are the expectations for a band structure in a magnetic material that is periodically modified. If novel spin-wave states appear due to the periodic modification, a magnonic crystal is formed. Second, we will calculate for one example the respective band structure.

For wave lengths larger than 1 µm, the dispersion of the spin waves is dominated by dipolar interactions. Corresponding frequencies are below 20 GHz, depending on the magnetic material and applied field. A steep quadratic increase is related to the nanometer wave length range. The strong magnetic exchange interaction takes over as the frequency reaches 1 THz. The dispersion has completely different slopes for both regions. The consequence is shown in figure 3.10: in the short wave length range a periodic modification will lead to a 'quasi free electron'-like band structure in the periodic zone scheme (schematically constructed on the left), similar to what is found in micromagnetic simulations [KLH09].

If dipolar interactions dominate, the energy splits for the Damon-Eshbach and backward volume modes: the band structure will be anisotropic with regard to the applied field. When the structure size is larger than the micrometer range, the negative dispersion of the backward volume mode leads to the surprising result that the second band can be lower in energy than the first band. We will see that this unexpected feature is found as well in our band structure calculations. A very complex spin-wave manifold can develop with many bands having similar

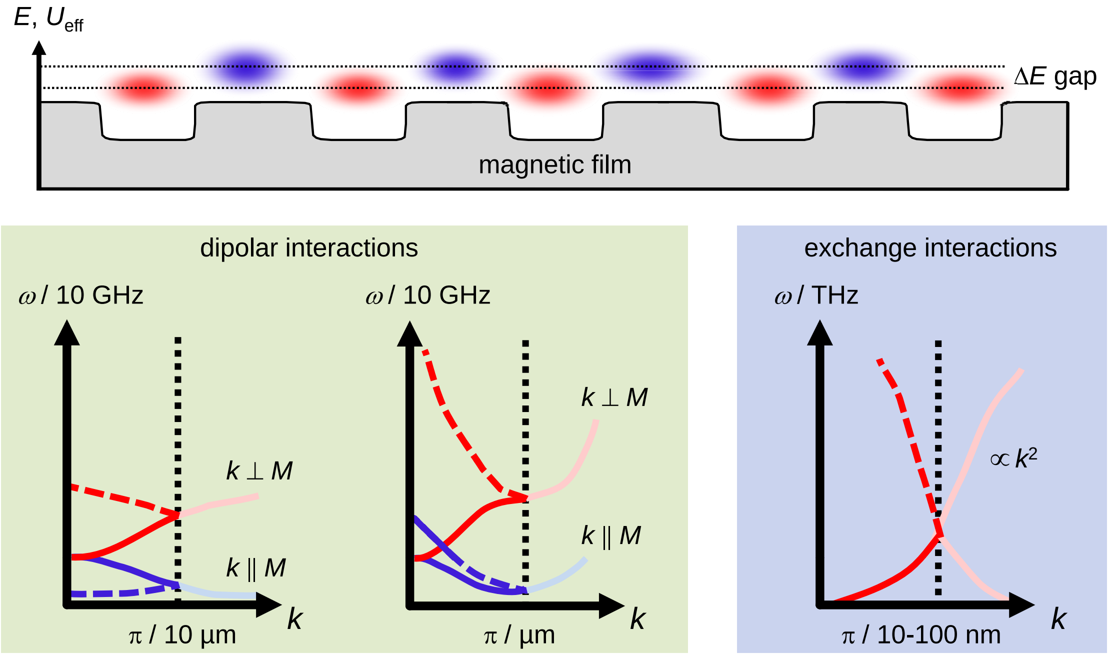

**Figure 3.10 – Schematic spin-wave dispersion for different length scales in the periodic zone scheme.** For a spin-wave Bloch state, prominent effects in the band structure are expected: 10 µm range (left), 1 µm (middle) and 100 nm (right).

energies. The three types of magnonic crystals classified in figure 3.10 will show a very different behavior: dipolar bands with negative or positive dispersion as well as quadratic exchange dominated bands.

In the following, we will discuss in greater detail how, similar to the Bloch theorem applied to electrons and photons, a magnonic band structure of a periodic ferromagnetic system can be computed. A theory was developed by Puszkarski et al. [KP08, VDDRP96]. A periodic alteration of the saturation magnetization was put into the Landau-Lifshitz Gilbert equation and solved by a plane-wave method. This theory is based on infinitely extended, three-dimensional magnonic crystals. While this ansatz emphasizes the close relationship of photonic and magnonic crystals, it neglects the particular property of inhomogeneous internal magnetic fields by setting $H_{\text{int}} = H_{\text{ext}}$. Note, that only if the regions with an inhomogeneous $H_{\text{int}}$ are restricted to a vanishing fraction of the magnonic crystal's unit cell, this can be justified. This is for example the case for a two-dimensional magnonic crystal, whose typical structure size is much smaller than its thickness. We will in the following show, how the plane-wave ansatz can be modified to apply to such a magnonic medium – exemplarily represented by an antidot lattice.

Spin waves with a wave length $\lambda$ which is much bigger than the film's thickness $t$

(external field in the film's plane), have almost uniform mode profiles in the $z$-direction. Thus, in the following the lower order modes' profiles will be assumed to be uniform and the so-called uniform-mode-analysis will be applied (see Hurben and Patton for details [HP95]). The basic idea of this approach is to neglect the exchange interaction, valid for sufficiently small $k$ as opposed by the full theory in reference [KS86], and solving the linearized Landau-Lifshitz equation

$$\begin{aligned} &i\Omega m_y - m_z + \frac{M_S}{H} h_z = 0, \\ &i\Omega m_z + m_y - \frac{M_S}{H} h_y = 0. \end{aligned} \tag{3.4}$$

The ansatz for the dynamic magnetization in the framework of the uniform-mode-analysis reads:

$$\begin{aligned} &m_y(x,y) = m_y e^{i(k_x x + k_y y)}, \\ &m_z(x,y) = m_z e^{i(k_x x + k_y y)}. \end{aligned} \tag{3.5}$$

In the above equations $m_y$ and $m_z$ are constant across the thickness. From the electromagnetic boundary conditions, it follows that the dynamic magnetic field reads:

$$\begin{aligned} &h_y = -m_y \frac{kt}{2} e^{i(k_x x + k_y y)} \sin^2 \phi, \\ &h_z = \left(-m_z + m_z \frac{kt}{2}\right) e^{i(k_x x + k_y y)}. \end{aligned} \tag{3.6}$$

By combining equations (3.5) and (3.6) into equation (3.4), the following direction-dependent dispersion relation can be derived:

$$\omega = \frac{g\mu_B\mu_0}{\hbar}\sqrt{H_{\mathrm{ey}}H_{\mathrm{ez}}}. \tag{3.7}$$

In equation (3.7), $H_{\mathrm{ey}} = H + M_{\mathrm{S}}\frac{kt}{2}\sin^2\phi$, and $H_{\mathrm{ez}} = H + M_{\mathrm{S}} - M_{\mathrm{S}}\frac{kt}{2}$, where $M_{\mathrm{S}}$ is the saturation magnetization, $g$ is the gyromagnetic ratio and $\phi$ is the angle between the external field and the wave vector. As a next step, a periodic modulation of the saturation magnetization is introduced:

$$M_{\mathrm{S}}(\boldsymbol{r}) = \sum_{\boldsymbol{G}} M_{\mathrm{S}}(\boldsymbol{G}) e^{i\boldsymbol{G}\boldsymbol{r}}. \tag{3.8}$$

Where $\boldsymbol{G} = [G_n,\, G_m]^T = \left[\frac{n2\pi}{a},\, \frac{m2\pi}{a'}\right]^T$ is a two-dimensional vector of the reciprocal lattice. Any geometry can now be specified by an analytic expression for the Fourier components $M_\mathrm{S}(\boldsymbol{G})$. In order to circumvent additional boundary conditions arising from the air regions in the experimentally interesting geometry of antidot lattices, the following trick can be performed: by filling the antidots with some artificial ferromagnet with a very high magnetic moment, spin waves in such a system either exist in the antidot, or in the surrounding matrix. Thus, a periodic energy landscape is constructed, which confines the spin waves. After solving the eigenvalue problem, one can remove the unphysical solutions, which predominantly dwell in the antidot.

The rather smooth nature of the boundary, as a result of the cutoff by the Fourier expansion (3.8) tends to mix the solutions for the matrix and the antidot. This results in non-vanishing imaginary parts for the frequencies of the modes in the matrix. However, one would need to use an infinite number of Fourier components to model a sharp transition between matrix and antidot, which would immediately violate the condition $\lambda \gg t$.

In the case of magnetic discs ($M_\mathrm{S}^2$) with radius $R$, which are periodically arranged on a square lattice with side length $a = a'$ and embedded in a magnetic matrix ($M_\mathrm{S}^1$), an analytical expression for the Fourier components of the magnetization profile can be found in [VDDRP96]

$$M_\mathrm{S}(\boldsymbol{G}) = \frac{2f\left(M_\mathrm{S}^1 - M_\mathrm{S}^2\right)}{P} J_1\left(P\right),$$

where $P = R|\boldsymbol{G}|$, $f = \pi R^2\, a^{-2}$ is the filling fraction and $J_1$ is the Bessel function of first order. Note that a modulation of other material properties like the gyromagnetic ratio or the exchange stiffness are not considered here. The generalization of equation (3.5) for the periodic material is a Bloch wave expansion:

$$\boldsymbol{m}(\boldsymbol{r}) = \sum_{\boldsymbol{G}} \boldsymbol{m}_{\boldsymbol{k}}(\boldsymbol{G}) e^{i(\boldsymbol{k}+\boldsymbol{G})\boldsymbol{r}}. \tag{3.9}$$

Using the uniform-mode-analysis, the dynamic magnetic field components are

$$\begin{aligned}
h_y &= \sum_{\boldsymbol{G}} h_{y,\boldsymbol{k}}(\boldsymbol{G}) e^{i(\boldsymbol{k}+\boldsymbol{G})\boldsymbol{r}} \\
&= \sum_{\boldsymbol{G}} \left( -m_{y,\boldsymbol{k}}(\boldsymbol{G}) \frac{|\boldsymbol{k}+\boldsymbol{G}| \cdot t}{2} \sin^2 \phi_{\boldsymbol{G}} \right) e^{i(\boldsymbol{k}+\boldsymbol{G})\boldsymbol{r}}, \\
h_z &= \sum_{\boldsymbol{G}} h_{z,\boldsymbol{k}}(\boldsymbol{G}) e^{i(\boldsymbol{k}+\boldsymbol{G})\boldsymbol{r}} \\
&= \sum_{\boldsymbol{G}} \left( -m_{z,\boldsymbol{k}}(\boldsymbol{G}) + m_{z,\boldsymbol{k}}(\boldsymbol{G}) \frac{|\boldsymbol{k}+\boldsymbol{G}| \cdot t}{2} \right) e^{i(\boldsymbol{k}+\boldsymbol{G})\boldsymbol{r}},
\end{aligned} \tag{3.10}$$

where $\phi_{\boldsymbol{G}}$ is the angle between the external field and $\boldsymbol{K} = \boldsymbol{k} + \boldsymbol{G}$. The equations (3.9), (3.10), and (3.4) provide a system of equations (finite number of $N$ lattice vectors)

$$\tilde{M} \boldsymbol{m}_{\boldsymbol{k}}^{j} = i\Omega_j \boldsymbol{m}_{\boldsymbol{k}}^{j}, \tag{3.11}$$

the eigen values of which have to be determined. Here,

$$\boldsymbol{m}_{\boldsymbol{k}}^{j} = \left[ m_{y,\boldsymbol{k}}^{j}(\boldsymbol{G}_1), ..., m_{y,\boldsymbol{k}}^{j}(\boldsymbol{G}_N), m_{z,\boldsymbol{k}}^{j}(\boldsymbol{G}_1), ..., m_{z,\boldsymbol{k}}^{j}(\boldsymbol{G}_N) \right]^T .$$

The eigenvalues $\Omega_i = 2\pi f_i \left(\gamma\mu_0 H\right)^{-1}$ are proportional to the eigenfrequencies $f_i$ and the mode profiles can be constructed from the eigenvectors $\boldsymbol{m}_{\boldsymbol{k}}^{j}$. Note that the $2N \times 2N$-matrix $\tilde{M}$ has a block-diagonal form:

$$\tilde{M} = \left\{ \tilde{M}_{yy}, \tilde{M}_{yz}; \tilde{M}_{zy}, \tilde{M}_{zz} \right\}.$$

In the equation above, $\tilde{M}_{yy}^{ij} = \tilde{M}_{zz}^{ij} = 0$ and

$$\begin{aligned}
\tilde{M}_{yz}^{ij} &= \delta_{ij} - \frac{1}{H} \left( -1 + \frac{|\boldsymbol{k}+\boldsymbol{G}^j| d}{2} \right) M_S(\boldsymbol{G}^i - \boldsymbol{G}^j) + \frac{H_{\text{dem}}((\boldsymbol{G}^i - \boldsymbol{G}^j))}{H}, \\
\tilde{M}_{zy}^{ij} &= -\delta_{ij} - \frac{1}{H} \frac{|\boldsymbol{k}+\boldsymbol{G}^j| d}{2} \sin^2 \phi_{\boldsymbol{G}^j} M_{\text{S}}(\boldsymbol{G}^i - \boldsymbol{G}^j) - \frac{H_{\text{dem}}((\boldsymbol{G}^i - \boldsymbol{G}^j))}{H},
\end{aligned}$$

with $i, j = 1 \ldots N$. In this formula, a locally varying static demagnetizing field $H_{\text{dem}}$ was taken into account by including a Bloch wave formulation of this field which is similar to the expression used for the magnetization profile:

$$H_{\text{dem}}(\boldsymbol{r}) = \sum_{\boldsymbol{G}} H_{\text{dem}}(\boldsymbol{G}) e^{i\boldsymbol{G}\boldsymbol{r}}. \tag{3.12}$$

In practice, the demagnetizing field can be obtained from numerical simulations, or from analytic expressions. Such a field may strongly alter the boundary conditions for the confinement. Since the model for the antidots confines the waves in yet another way, it cannot be included for this approach. Nevertheless, artificial structures exist [WZL+10], where the full model, taking into account the demagnetizing field and the exchange field, could similarly be applied.

For a realistic situation, one problem has to be solved: the accurate description of a potential demands many reciprocal lattice vectors. But in this case the initial assumption $\lambda \gg t$ may be violated. A good agreement between theory and experiment may then only be expected for the lowest order branches. For the antidot model, we will only use thirteen lattice vectors here to discuss general trends. Note the sketched theory could be very easily altered to describe the situation, where – as for active devices – the spatially varying quantity is the applied field.

Band structure calculations are performed for a CoFeB film with a thickness $t = 50\,\mathrm{nm}$, a hole distance $a = 3.5\,\mathrm{\mu m}$ and hole diameter $d = 1\,\mathrm{\mu m}$ (figures 3.11 and 3.12), and a nickel film with the same geometrical parameters (figure 3.13). A field of 130 mT is applied in the plane along the (1,0)-direction. The discs are filled with an artificial ferromagnet with a high saturation magnetization of 10 T. The artificial solutions, which predominantly dwell in the discs, are by virtue of the high magnetic moment shifted above the depicted frequency range. This ansatz separates the solutions into two sets. Only the low frequency which are of interest are given in figure 3.11.

Because of the larger saturation magnetization $M_\mathrm{S}$, the bands for CoFeB are much higher in frequency. In the following we will describe some typical features. For comparison, the free spin-wave band structure is shown, with the first and second band marked. For this purpose, we have taken equation (3.7) and plotted it in a reduced zone scheme. As expected, no band gaps at the zone boundary are present. On the left side of figure 3.11 the propagation direction is parallel to the applied field and thus determined by the backward volume geometry. As expected, with respect to the schematic bands given in figure 3.10 the second band is below the first band in energy. At the right, for the $\mathit{\Gamma} \rightarrow X'$ direction, the band dispersion is determined by the Damon-Eshbach geometry, showing a steep increase. The band calculation clearly reveals a different dispersion for the magnetization along the (1,0)-direction. Only for the $M \rightarrow \mathit{\Gamma}$ point the bands are the same. At the points of high symmetry, a splitting is observed which is of about 0.5 GHz in frequency. The uniqueness of the solutions inhibits sections of individual bands, as they appear in the free spin-wave picture. Instead,

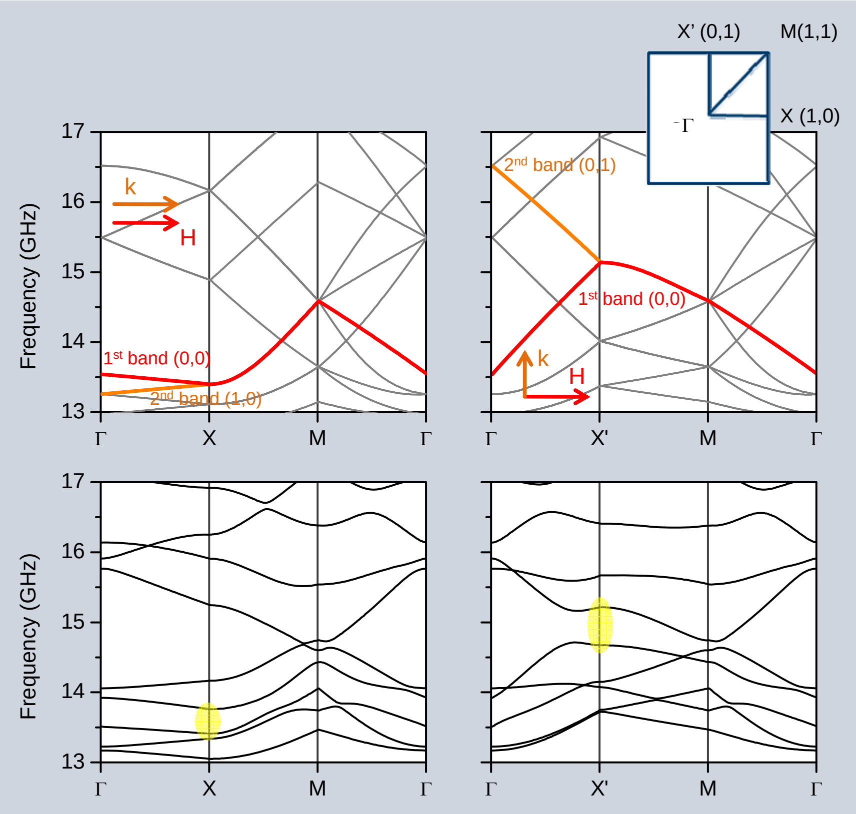

**Figure 3.11 – Band structure calculation for a CoFeB film for a two-dimensional square lattice.** Top: Free spin-wave band structure with first and second band marked in red and orange, respectively. Bottom: Solved by a set of Bloch states for a film thickness of $t = 50\,\mathrm{nm}$, hole distance $a = 3.5\,\mathrm{\mu m}$ and hole diameter $d = 1\,\mathrm{\mu m}$. The splitting at the high symmetry points $X$, $X'$ at the zone boundary is marked with the shaded yellow area.

in the hybridization regions, the modes repel each other and interchange their character. Detailed theoretical studies of the group around Puszkarski showed the appearance of gaps in the band structure of two-dimensional [VDDRP96] and three-dimensional [KP08] materials, where the spin-wave propagation is forbidden. They find that the size of the magnonic gap increases if the contrast between the constituents in magnetization or exchange stiffness is increased.

### 3.4.3 Periodic dipolar potential in structured films: micromagnetic simulations

Apart from analytical descriptions, numerical simulations provide a convenient tool to investigate magnonic crystals and predict their spectral response, please refer also to a current review especially devoted to this topic [Kim10]. For the purpose of numerical simulation, it is necessary to implement periodicity. The

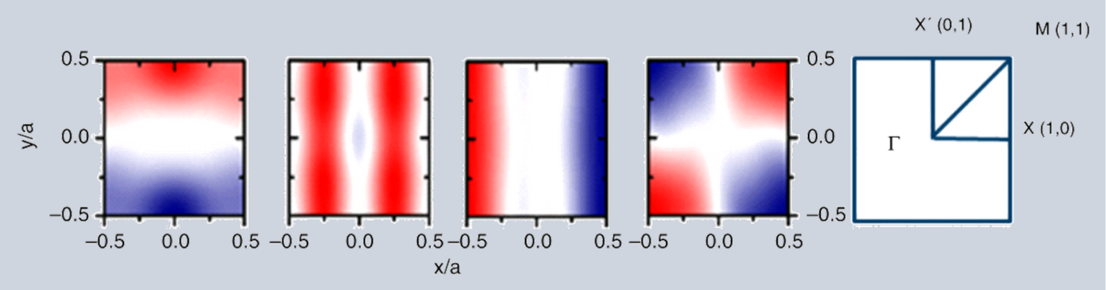

**Figure 3.12 – Distribution of the spin-wave amplitudes at the point of high symmetry $X$, $X'$ and $M$.** From the left to the right, one can see mode profiles of the first band at $X'$, $\Gamma$, $X$ and $M$. Different colors denote positive and negative phases. (From reference [Ulr10]).

main physical entity to handle in this context is the long-range static demagnetizing field which is of dipolar origin. The easiest way to do this is to construct a simulation volume that consists of many unit cells. One can then assume that, at least in the central cell, the surroundings approximate infinite periodicity. Of course, such an approach demands high computational power, especially if one has to respect fundamental length scales arising from the exchange interaction. The discretization length should not exceed a few nanometers if dynamic or static phenomena on this scale, like exchange dominated spin waves or domain walls, are considered. The result is that simulating many unit cells is only applicable when access to a proper computing facility is given.

Implementing periodic boundary conditions for a single unit cell circumvents this problem by using an accordingly modified demagnetization field. Before the integration of the LLG-equation, a demagnetization tensor is computed from the geometry of the sample [FFBF07, DP99]. In a single isolated unit cell, strong divergence of the magnetization occurs at the boundaries. By assuming an identical magnetization configuration repeated periodically in space, this divergence is removed, and the demagnetization field of a continuous and periodic medium is created. In the strict sense, the imposed exact repetition restricts dynamic computations to spin waves with $k = 2n\pi\, a^{-1}$, where $n \in N^0$ and $a$ is the lattice constant.

Only by increasing the number of unit cells within the (periodic) simulation boundary, a finer grid in the reciprocal space can be probed. For the computation of the static equilibrium magnetization configuration or quasi-static simulations of hysteresis loops, the described method provides less ambiguous results. Note that the approach can also be applied to the dynamical-matrix method which reformulates the linearized LLG-equation as an eigenvalue-problem on a finite grid [RSdLK07]. Apart from the fact that the dynamic matrix method only ap-

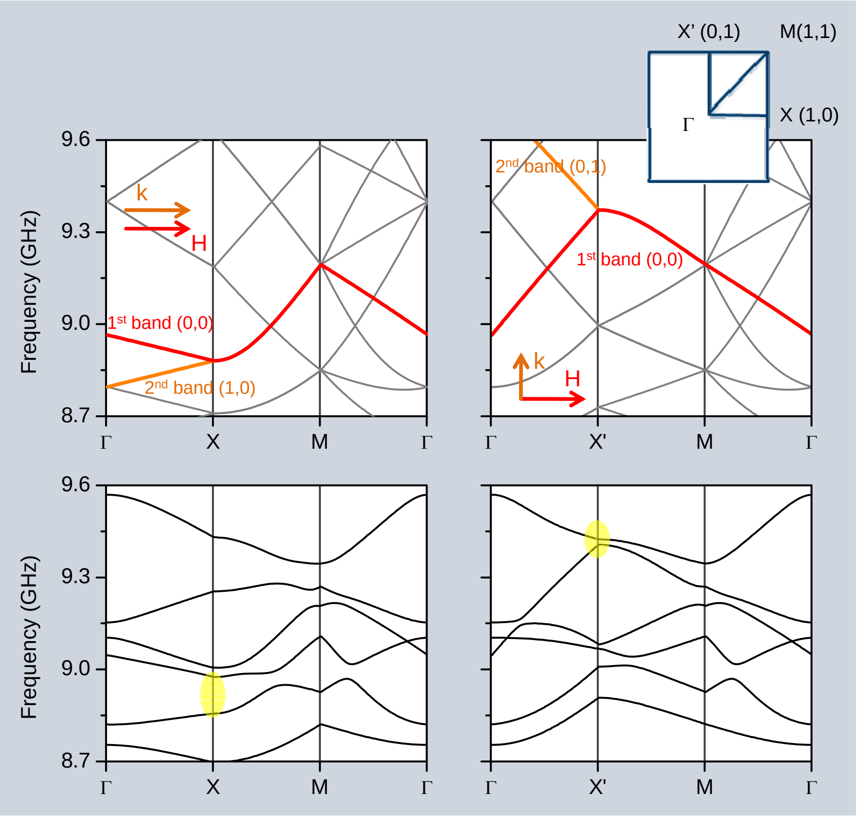

**Figure 3.13 – Band structure calculation for a Ni film for a two-dimensional square lattice.** Top: Free spin wave band structure with first and second band marked in red and orange, respectively. Bottom: Solved by a set of Bloch states for a film thickness of $t = 50$ nm, hole distance $a = 3.5$ µm and hole diameter $d = 1$ µm. The splitting at the high symmetry points $X$, $X'$ at the zone boundary is marked with the shaded yellow area.

plies to the linear regime of magnetization dynamics, it is practically limited to structures not bigger than 100 nm.

Figure 3.14 shows the calculation of the internal field ($H_{\mathrm{int},x} = H_{\mathrm{ext},x} + H_{\mathrm{demag},x}$) for a CoFeB sample, where the anisotropy field may be set to zero. If not stated otherwise, the external field was canted by an angle of 30° out of the film plane, mirroring the experimental situation to be discussed in a later section. The pictures show the equilibrium state of a unit cell of a square and an unconventional unit cell of a hexagonal antidot structure. The colors represent the field component parallel to the external field, normalized to the external field amplitude. The cells were computed using the software package *Nmag* which can apply periodic boundary conditions.

Calculations of the square lattice show inhomogeneities around the antidots, while in the hexagonal simulation, these regions show higher expansion due to the

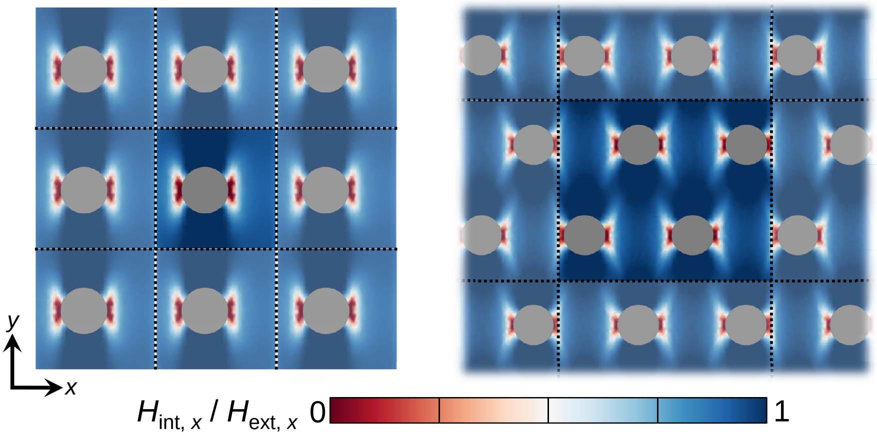

**Figure 3.14 – Calculation of the total internal field for a square (left) and a hexagonal (right) antidot structure with an applied field in the $x$-direction of $\mu_0 H_{\text{ext}} = 100\,\text{mT}$.** The colors show the minima in the extension of the internal field around each antidot. Please note the slight asymmetry in the square case to rule out unit cell artifacts.

higher fraction of holes per unit area. In both simulations, a lattice periodicity $a = 3.5\,\mu\text{m}$ and an antidot diameter $d = 1.36\,\mu\text{m}$ was used, which lead to filling fractions of 11.9% and 13.7% in the case of square and hexagonal lattice, respectively. Note that concerning low computational power, discrete element sizes in this case are in the range of 60 nm. Therefore, exchange interactions cannot be discussed by this simulation. Significance has been proven by calculations with bigger and smaller elements showing identical results.

### 3.4.4 Micron and nanometer structuring for static and active magnonic crystals

Thin film technology provides a large variety of techniques to prepare one- and two-dimensional structures. The relevant length scales may range from nano- to millimeters, depending on the material under investigation. A technique that is becoming increasingly important is lithography using a beam of ions. Starting from a continuous film, the magnetic material is sputtered off by a focused beam of gallium ions (focus 10 nm). Scanning the beam across the sample provides the flexibility of e-beam lithography without the need for further processing of the specimen. This reduces the efforts and the production of precise large scale nanostructured samples is possible. An example of a two-dimensional structure is given in figure 3.15 showing high precision, long-range order, and in the inset, an enlargement of a well defined constituting antidot. Damage and implantation of Ga ions happens only close to the antidot site. With this method different lattice geometries can conveniently be achieved and it was used for most of the structures shown in the experimental section. Generally, the damping or magnetization of the material is found to be unchanged.

Other standard techniques, such as optical lithography for structures above 1 µm diameters and e-beam lithography combined with lift-off or $\mathrm{Ar}^+$-ion milling, are also used as methods for structurization. In the bottom row of figure 3.15 we give some examples of magnetic superstructures. By ion beam modification, the exchange bias can be modified locally, resulting in a separate switching of different areas of a material [CBF+98]. The varied switching field allows an active modification of the superstructure during the experiments. A modified switching field can also be realized by combining soft/ hard materials [SDJ+07]. An example where dynamic experiments on very small magnonic structures have been realized is shown on the very right of figure 3.15: using self-organized or prestructured porous alumina membranes it is possible to enter the range below 100 nm [MANG09].

Ferrites like yttrium iron garnet (YIG) are particularly well suited for fundamental research. They have a very low Gilbert damping ($\alpha = 6 \times 10^{-5}$) and decay lengths are in the millimeter range. Thus, typical structures are modified on larger length scales [SCH10]. In YIG already dynamic magnonic crystals have been realized by using a set of parallel, periodically spaced, current conducting strips close to the YIG film surface. When the current is turned on the current flow causes a sine-like variation of the film's internal magnetic field [CNS+09, VB10].

## 3.5 Experiments with magnonic structures

Magnonic crystals with different dimensionalities have been experimentally investigated in the past. In one dimension, frequency band filters were demonstrated by the group of Hillebrands (see review on YIG magnonics [SCH10]). For a two-dimensional magnonic crystal, the simplest case is a squared antidot lattice in a thin ferromagnetic film, as discussed by Neusser and Grundler [NG09], however the expression ‘magnonics’ had been formed by Kruglyak and Hicken [KH06]. In the experiment, the control over the internal field distribution by the filling fraction (area of the holes per total area) and lattice parameter turns out to be crucial. From a broad continuum of spin waves at high energies in low damped CoFeB films (Gilbert damping $\alpha = 0.006$), in which the spin-wave propagation length is more than 100 µm, Bloch modes appear only for low filling fractions [ULM10].

The static dipolar fields stemming from a single hole defect have also been studied by combining MFM measurements and micromagnetic simulations [RRRV+08]. One can access the confinement distance and determine the interaction of single

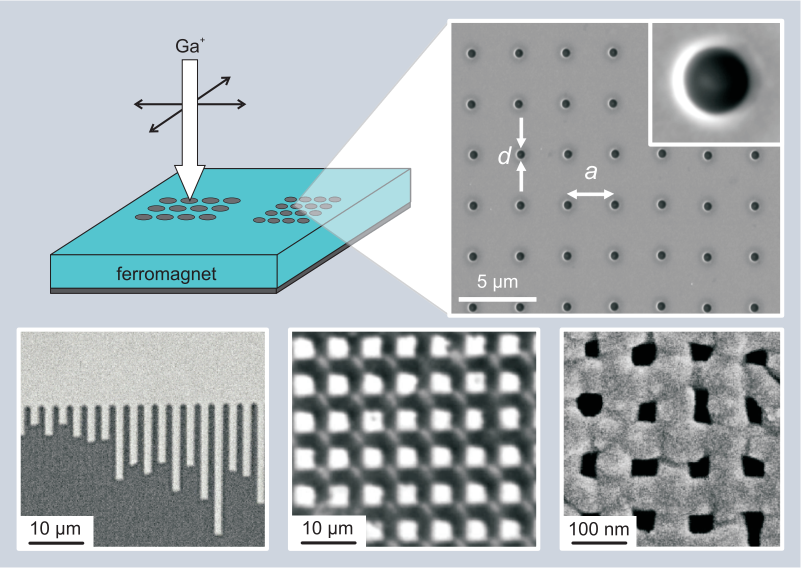

**Figure 3.15 – Magnetic periodic structures on different length scales and by different methods.** Top: Antidot structure prepared by focused ion beam etching. The parameters *d* (diameter of the hole) and *a* (antidot distance) define the filling fraction. Bottom: other techniques involve ion beam bombardment of exchange biased layers which modifies the switching field (left, from reference [CBF+98]) or combined soft/hard composite materials (middle, from reference [SDJ+07]), in both cases the magnetic contrast has been imaged. Smallest structures on large areas can be produced by interference lithography or by self-organized or prestructured porous alumina membranes entering into the nm-range (right, from reference [MANG09]).

defects with radius $R$. It is found empirically that if the separation is smaller than $10R$, collective effects emerge. This is also true for the dynamic case [BOT+09]. In this experimental section a somewhat larger part will be devoted to the application of femtosecond lasers to study magnonic materials. We will divide the presentation of experimental results into those, where spin-wave localization dominates the collective behavior in the periodically structured material and those, where delocalized Bloch modes predominate. To give an introduction to this rich field of research, experimental findings from the various magnonic systems obtained with different approaches will be discussed. First, a short overview on the experimental techniques to detect and excite spin waves will be given.

### 3.5.1 Techniques

Experimentally spin-wave modes in periodically structured materials have been studied by different techniques: microwave-based techniques (ferromagnetic resonance (FMR), vector-FMR or pulse-inductive microwave magnetometer (PIMM)), in combination with spatial resolved Kerr microscopy; also, optical pump-probe techniques using femtosecond lasers have been applied. Brillouin light scattering (BLS) takes a special role since it also allows a resolution in $k$-space, and thus, to measure dispersions and band structures directly. The different methods have different advantages. Typical specifications for a study of magnonic materials are that small areas have to be measured for all in common. Structurization of materials in a top-down approach generally allows, as outlined in the previous chapter, only small areas.

### Microwave techniques: resonance and time-resolved experiments

Microwave-based techniques owing to high sensitivity on small areas have the strip-line geometry in common. Two methods have to be distinguished: ferromagnetic resonance (FMR), or vector network analyzer-FMR which use a harmonic resonant excitation, and methods that use pulsed activation as pulse-inductive microwave magnetometer (PIMM). In the first case, a harmonic microwave is guided through the strip line and the transmitted signal is measured [PGG06], similar to a standard FMR experiment using a microwave hollow conductor measuring the absorption power of the sample in the cavity, however much more sensitive. More complex setups use a local excitation and detection. That enables guiding the microwave signal through the magnonic structure directly and early studies showed the formation of narrow transmission bands in YIG [GNZ+03]. Also, this allows studying the transmission and reflection of a magnonic material as a function of the frequency by a vector network analyzer.

PIMM uses a pulsed excitation [SLCR99]. The ringing down of the magnetic excitations is shown in figure 3.16 for different field values. The signal is the inductance-induced voltage into the stripline. To fully exploit the advantage in probing small volumes, the magnetic structure has to be lithographically structured on top of the wave guide. A local approach is possible by using an inductive magneto-dynamic probe that can be scanned across the sample, in which spin waves are excited by a microwave strip line [WKS+04].

### Microscopy techniques: imaging of resonant modes

To map magnetic modes with different frequency spatially, microscopy methods have to be used. Experiments on magnonic antidot structures have been performed by Pechan et al [PYC+05]. They combined Kerr microscopy with time resolution to map modes at different frequencies. A current pulse excites the magnetization dynamics which are probed spatially by rastering the sample and measuring the time-resolved Kerr signal. The pump beam and probe beam come from a femtosecond pulsed laser. The response on different spot positions on the sample is reprinted from their work in figure 3.17. To analyze the data, the time-domain data is Fourier transformed to the power spectrum at each spot to a map

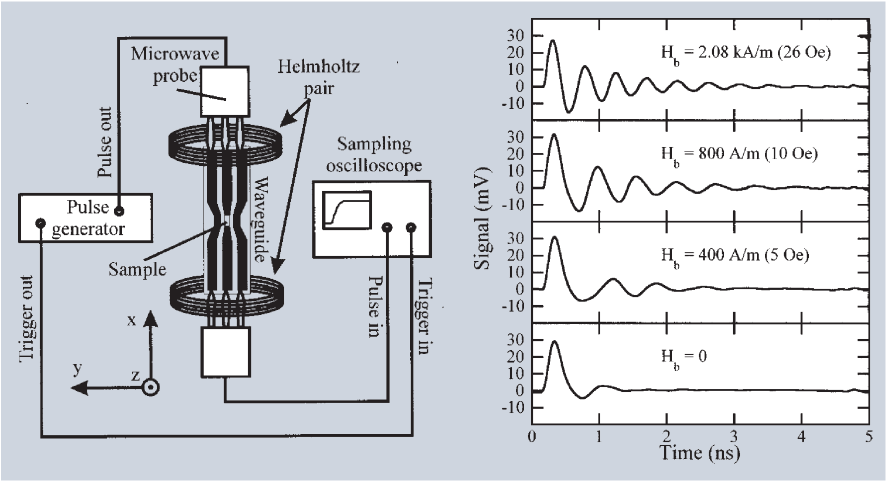

**Figure 3.16 – Time-resolved wave-guide techniques: pulse-inductive microwave magnetometer (PIMM).** [SLCR99].

power distribution which determines the mode location at the resonance frequencies. A very recent work shows the power of this method to map the localizing of spin-wave modes [NDB+10]. Examples will be discussed in section 3.5.2.

### Brillouin light scattering (BLS): micro- and nano-BLS

BLS can access a further degree of information: the measuring of the inelastically scattered light under a certain angle allows the calculation of the $k$-vector and, by measuring the energy shift, the frequency is accessible simultaneously. This method has been developed and applied to micron-sized structures by the Hillebrands group to highest perfection over the last years. Using methods that allow the determination of the resonance of a magnetic mode alone gives access to the energy of the mode for different field directions, but no information on the wave length. Then, by studying the field dependence, modeling the dispersion and comparison to the experimental data, modes can be identified. Naturally for that reason, BLS is the most powerful method to access the dispersion and spin-wave band structure of a material directly. For example, a wide range of wave vectors can be probed [SJV+10], and three-magnon processes investigated [OnRKK+09]. The method can be combined with microwave excitation to select or populate well-defined modes or to investigate the propagation of spin waves along a magnetic wave-guide stripe.

Two recent developments should be mentioned: by using phase information, phase fronts can be investigated [VSH+09]. Also, the resolution of the method has been considerably increased just lately: using high-resolution scanning microscopy

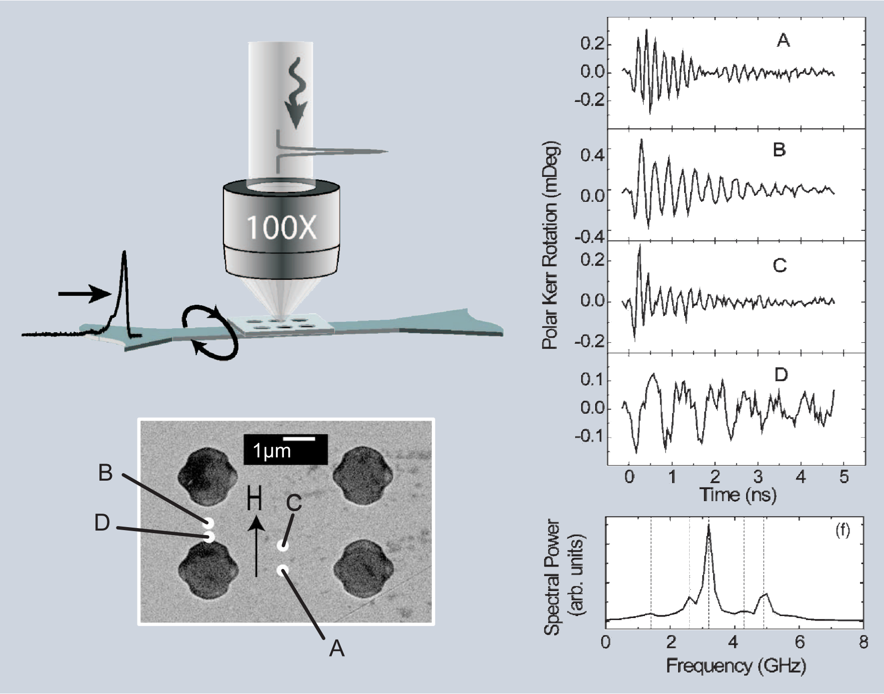

**Figure 3.17 – Time and spatially resolved MOKE.** [PYC+05].

in combination with BLS, the resolution has been increased, approaching 200 nm (µ-BLS). This allowed the mapping of modes in permalloy wave guides, shown in figure 3.1. A further step has been published by the Demokritov group. Using an optical aperture on a cantilever, near-field imaging of the BLS intensity allows mapping of the edge modes of a micron-sized ellipse, shown in figure 3.18, with a resolution of even below 55 nm. The µ-BLS technique was also used for the first observation of Bose-Einstein condensates of magnons [DDD+06, DDD+08] under continuous pumping of spin waves at microwave frequency.

## Femtosecond laser techniques: photo-magnonics

A technique to investigate ultrafast processes involving spin waves is the excitation with femtosecond (fs) laser pulses, a field recently reviewed by Kirilyuk et al. [KKR10]. Such ultrashort pulses can be achieved using titanium-doped sapphire seed lasers. Due to the broad emission spectrum (FWHM = 200 nm) of the crystal, by mode locking of more than $10^5$ modes, fs laser pulses can be generated. Resulting pulses with a repetition rate of typically 80 MHz have an average energy of about 6 nJ. At the expense of repetition frequency, amplification of single pulses to ≈ 5 µJ then at 250 kHz is feasible to achieve large degrees of demagnetization upon absorption of the pulse by the sample. Focusing the pulses to a 60 µm spot

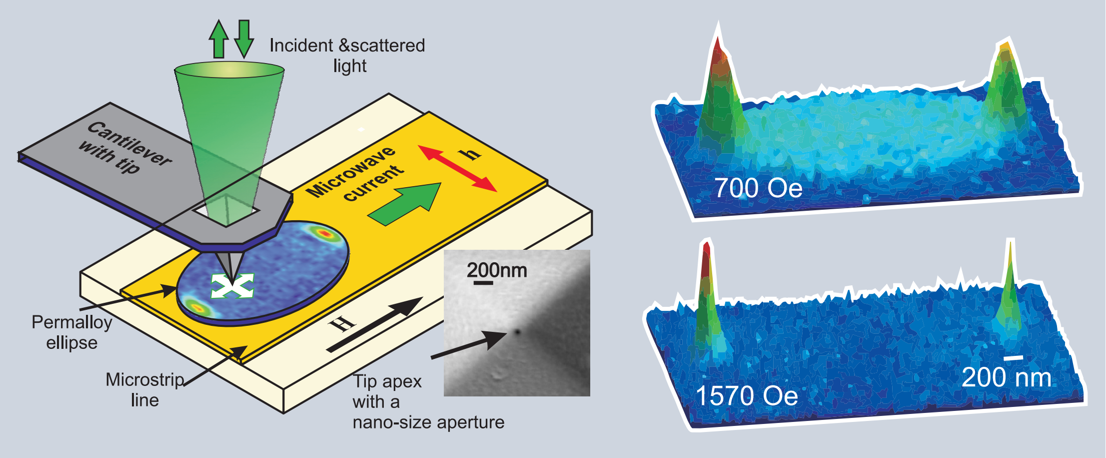

**Figure 3.18 – BLS setup with high spatial resolution.** Left: Schematic of how to achieve nanometer resolution with a BLS setup. An AFM tip with a nanosize aperture is used for near-field imaging. Right: Experimental data obtained from an elliptical permalloy disc showing precessional modes localized at the edges. The applied field tunes the spatial extension of the magnetic excitation in a manner proportional to $1/H_{\text{ext}}$. From reference [JDF+10].

(in diameter) onto the sample, one achieves a fluence of $60\,\text{mJ}\,\text{cm}^{-2}$.

However, the use in magnonics is relatively new and we will therefore go into more detail. For all-optical experiments, the laser beam is split into two pulses. The stronger pump pulse (95% of the intensity) yields demagnetization in the order of up to 50% and is used to excite the spin waves in the sample. The other, less intense, pulse locally probes the magnetization of the sample. Due to the magneto-optical Kerr effect, upon reflection from the surface, the polarization changes depending on the magnetization. It is remarked that in this technique not the absolute, but only the change of magnetization induced by the pump pulses is recorded.

In the experimental setup [DEP+06, WDL+08], the pump pulse is guided over a delay stage in order to tune the time delay between both pulses. The magnetic field of up to $\mu_0 H_{\text{ext}} = 150\,\text{mT}$ is in the longitudinal Kerr-effect configuration, but tilted 30° out of the film plane. Due to the very small signal, a double-modulation technique is used with a mechanical chopper operating at 800 Hz in the pump beam and a photo-elastic modulator (PEM) at 50 kHz in the probe beam. In the experiments, the time delay between pump and probe can be varied in steps of very few fs up to the maximum range of 1 ns after excitation.

A data set of such a measurement, recorded on a 50 nm nickel film, is plotted in figure 3.19 (right). Before the pump pulse arrives, the magnetization is in a state of equilibrium. At $\Delta\tau = 0$, the pump pulse hits the sample, leading to the

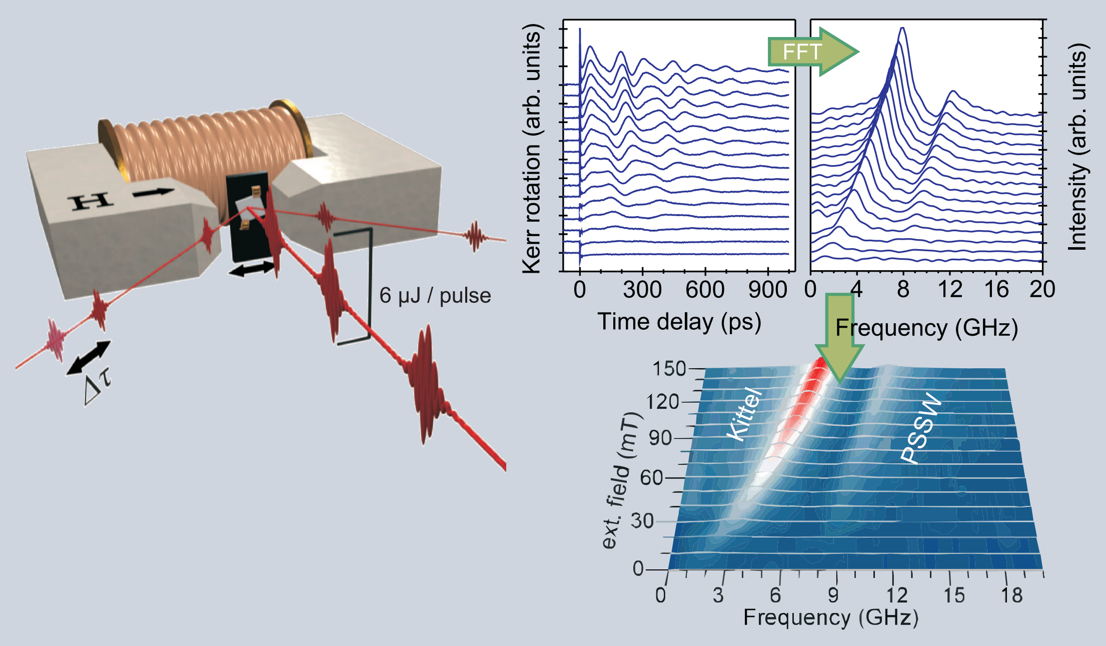

**Figure 3.19 – Time-resolved pump-probe setup.** Intense pump pulses for excitation and the detecting probe pulses with tunable time delay $\Delta\tau$ (left). Analysis steps for a 50 nm Ni film (right): time-resolved traces as a function of the pump-probe delay, Fourier transform and color plot of the Fourier power.

demagnetization of the sample, as shown by the strong change of the magnetization. As one can already see in the raw data, the magnetization shows two different modes of precession. After analysis (subtraction of the incoherent background and Fourier transformation) these modes can be identified as the uniform Kittel and the perpendicular standing spin-wave modes. Both precession amplitude and frequency increase linearly with the external field, as expected. For a better visualization, all frequency data is also plotted in a color code.

Compared to BLS measurements, the pump-probe technique only probes the Kerr rotation, and thus, is not directly $k$-sensitive. Comparing it to the resonant excitation at a fixed frequency in FMR, significant differences are evident. The excitation mechanism using a pump pulse does not select a certain mode. Instead, high energy spin waves with a broad distribution of wave vectors are excited. During the first few picoseconds after excitation, these relax to lower energy states [DM07], cool down and populate modes given by the sample and magnonic crystal itself. All modes observed are not externally selected (for example, by an alternating microwave field), but are selected by the sample itself. Hence, the results of this technique lead to different information on the magnon density than the ones described previously. This technique combines photo and spin-wave excitation, hence the term photo-magnonics. A recent work by Hamrle showed that both optical techniques, BLS and TRMOKE are comparable in their sensitivity [HPH$^{+}$10].

### Fundamental mechanisms for spin-wave excitation using lasers

The full relaxation path of spin waves after laser excitation is a research field of its own. We will therefore briefly describe the ideas in this separate section. Since there is no direct coupling between the spin degree of freedom and the light field, we want to shed some light on the excitation mechanism specifically used in the examples to follow. How can spin waves be excited and what is the specific mechanism used in photo-magnonics?

Just recently two parallel investigations combined theoretical and experimental proof that it is possible to quantitatively describe femtosecond demagnetization dynamics in its absolute value and characteristic time scales [MÏ10, KMD$^{+}$10, ACFW$^{+}$10]. A slowing down due to intrinsic fluctuations characteristic to the exchange-coupled spin system can be mirrored by the models found. It is found for strongest demagnetization or approaching the Curie temperature. Atxitia et al. [ACFW$^{+}$10] used a stochastic equation of motion that is mapped onto a macrospin description, the Landau-Lifshitz-Bloch equation.

From spatially resolved micromagnetic simulations, one gets a microscopic insight into the origin of the delayed remagnetization. Short wave length spin waves and higher order spin-wave modes with a high spatial frequency dominate the dynamics within the first ps [DM07, KHN$^{+}$07, NMW$^{+}$05]. These excitations are distributed very efficiently from the hot-spin region into the magnetically not disturbed region. For small excitation-spot sizes, the magnetization can be restored very fast by the emission of spin-wave packets and high-energy magnons [ELM06]. High-energy magnons have been studied in detailed, experimentally challenging neutron-diffraction experiments in ferromagnetic metals in the 80s [PMMS88], investigating the broadening of the spin-wave dispersion curves at high energies as predicted also at that time arising from the strong interaction with the Stoner band, called Landau damping: near the surface of the Brillouin zone, it results in a severe energy dissipation and extremely short lifetime of the high-energy spin waves.

In the last years, using spin-resolved electron energy loss spectroscopy [EAT$^{+}$05, VEA$^{+}$04] and theoretical investigation [CMM04], these excitations have been related to spin-wave packets with lifetimes below 1 ps and localized within a few nanometers only. The starting point of the relaxation chain is an energy transfer from the high-energy spin-wave excitations resulting from local spin-scattering

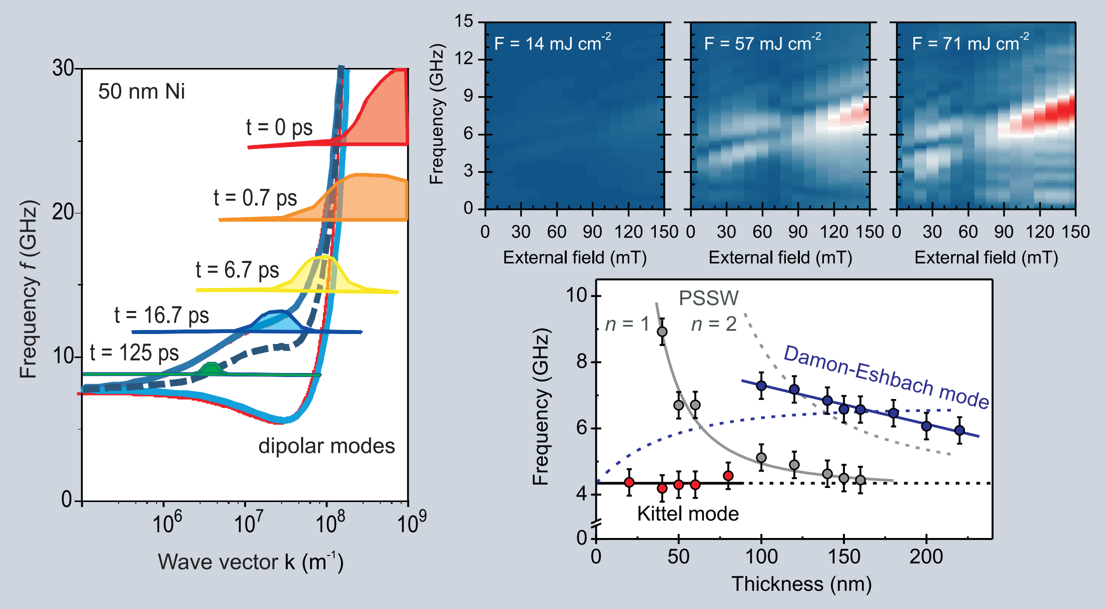

**Figure 3.20 – Spin-wave relaxation in all-optical experiments after laser excitation.** Micromagnetic simulation (left, from reference [DM07]). Fourier power spectra for different pumping fluencies 14, 57 and 71 mJ cm$^{-2}$, Ni film 150 nm thickness (right). A Damon-Eshbach mode with fixed wave length $\lambda$ from 0.5 - 6 µm as determined by the Ni thickness is found. Precession amplitudes can be up to 5°. A summary of the mode and wave-length dependence is given below as a function of the Ni thickness (for a magnetic field of 50 mT) (from reference [LEHM10]).

processes to the lower-order spin-wave excitations. The high-energy excitations are overpopulated in an ultrafast demagnetization experiment. Furthermore they are densely populated (demagnetization typically much larger than 1%). It seems plausible that the Stoner excitations that are populated by the elementary spin-flip relaxation processes of the hot electron system (exchange scattering for hot electrons [CMM04, HE73] and Elliott-Yafet spin-flip processes for lower electron energies [Ell54, KRLdJ05, WMD$^+$08, SF09, SIF10]), decay into short wave length spin excitations and gradually relax to the lower spatial frequency excitations discussed in reference [DM07].

A very recent work by Schmidt et al. nicely proves these ideas on the femtosecond time scales experimentally [SPD$^+$10]. The energy is transferred from the highest excited mode into modes owning a lower energy following the spin-wave dispersion. From the corresponding Fourier transform, through the magnetization profiles in the micromagnetic model, spin-wave excitations are accessible (spatial frequency) given in figure 3.20. High spatial frequencies dominate after excitation at $\tau = 0$. During the relaxation process, the center of the spectral weight moves towards lower spatial frequencies. For 6.7 ps, the center is at around 0.1 nm$^{-1}$.

This corresponds to a spatial spin-wave period of 10 nm. The damping results in an overall reduction of the spectral amplitudes, accompanied by a shift of the spectral weight to lower frequencies. It has to be mentioned that the dipolar Damon-Eshbach modes are not within the simulation window because of the film thickness of only 50 nm. Nevertheless, simulations are an indication for an energy transfer from high-energy modes to low-energy modes within the spin-wave relaxation.

Here we see some similarities to the Bose-Einstein condensation, where spin waves driven by microwave fields relax to their lowest state of energy and overpopulate these states so that condensation sets in by permanently driving up the chemical potential [DDB+08, DDD+06]. In these experiments the decay from the GHz pump frequency to the frequency of the lowest energy level of the condensate can be followed directly. The optically-induced precession verified by many groups [JVN+98, JNF+99, DEP+06, vKJK+02, VAG+05] has been successfully used to extract the magnetic Gilbert damping for a variety of materials [LRK+10, LSKH10, MMMG08, RKBS08]. The amplitudes can be increased up to few degrees by increasing the pump fluence.

In the excitation spectra the mode of the homogenous precession, standing spin waves of up to fifth order for low damping materials [Kim10], and dipolar spin waves with a fixed $k$-vector inversely related to the film thickness have been investigated [LEHM10]. Such a well-defined $k$-vector resulting from all-optical spin-wave excitation leads to the idea to study the effect of a periodic modification in order to create a magnonic crystal with that periodicity.

### 3.5.2 Localization effects in magnonic crystals

The idea to excite spin-waves all-optically in a magnonic crystal had been put forward by Kruglyak et al. [KH06]. In the following, we will study 2D magnonic crystals. And in fact: when compared to a continuous film as presented in the previous section, magnetization dynamics drastically change after arrays of antidots have been inserted.

The two-dimensional periodic modification of the internal magnetic field has been realized by focused ion beam. Shown in figure 3.21 are three data sets, recorded on a continuous 150 nm nickel film, as well as on two different antidot lattices of the respective sample. On the structured areas (lattice parameter 3 µm (3.5 µm), antidot diameter 0.5 µm (1 µm), respectively) the Damon-Eshbach mode as previously excited at field values below 100 mT is not observed anymore, instead a new magnetic mode is observed. Its frequency does not significantly change with the external field. This is a hint that a major role is played by the internal

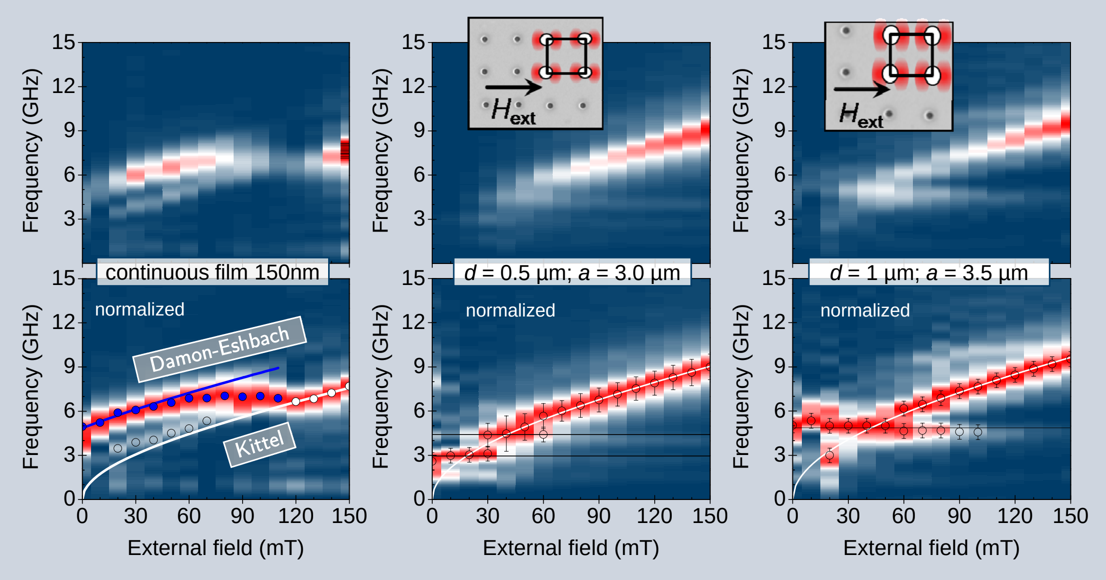

**Figure 3.21 – Effect of an antidot lattice structure measured by all-optical spin-wave excitation and detection.** Left: continuous nickel film of 150 nm. Middle: antidot diameter 0.5 µm. Right: antidot diameter 1 µm. With the antidot diameter, the mode intensity showing weak field dependence and low frequencies is found to increase.

magnetic field which is significantly reduced next to the antidots, compared to the applied field. These regions of internal fields, however, become smaller with increasing field and finally disappear. The interaction between different modes at the antidot sites decreases and they are not coupled anymore. This is in accordance with the disappearance of these weakly field-dependent modes at a certain field value which is found to be different for different antidot diameters.

From different previous works it is well-known, that spin-wave modes in antidot lattices can have localized or extended character, referring to the spatial behavior of the mode amplitude. This was shown in micromagnetic simulations for antidot lattices [NBG08], and in earlier experiments by Pechan [PYC$^{+}$05]. The results of the latter using time-resolved Kerr microscopy are given in figure 3.22. In 2005, they had already mapped two kinds of modes: the spin-wave amplitudes of the high-frequency modes have dominantly maxima in between the antidots, whereas the low-frequency modes have strong intensity around the antidot, showing a typical structure that we know already from section 3.4.3: it mirrors the areas of a reduced internal field. Recently, this was investigated in a combined study by vector network analyzer FMR, time-resolved Kerr microscopy and BLS [NDB$^{+}$10].

The appearance of delocalized, extended modes strongly depends on the prop-

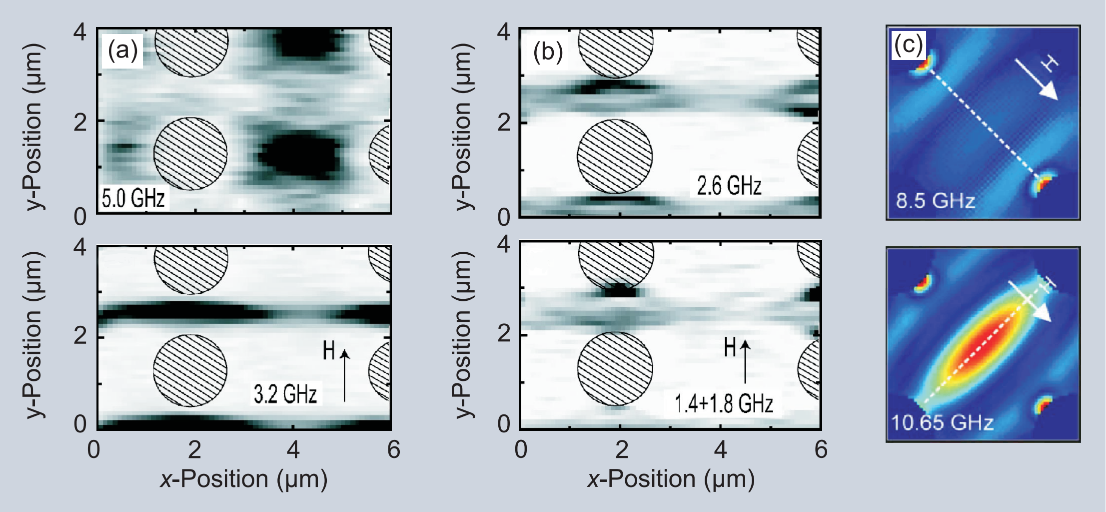

**Figure 3.22 – Spatially resolved Fourier power of resonant modes.** (a), (b) Modes measured by time-resolved Kerr microscopy (from reference [PYC$^+$05]): the Fourier power at a resonance frequency is mapped. High-frequency modes are found between the antidot structures (a), low-frequency modes localized in the low effective field regions around the antidots (b) depict the areas of a reduced internal field. In (c), numerical results from reference [NBG08] are reprinted that indicate an analogue situation.

agation length of the spin wave excited. In the case of figure 3.21, where nickel is the ferromagnet under investigation, the spin-wave propagation length is on the order of ten microns due to the rather large intrinsic Gilbert damping ($\alpha = 0.02$). This distance is similar to a few unit cells of the antidot lattice. The data in figure 3.21 can thus be explained: arising from the demagnetization field, at the antidot edges are potential wells for spin waves with a rapidly changing effective field. At these sites localized modes are excited, while in the regions of constant internal field the uniform Kittel mode is present.

A schematic of the internal field has already been depicted in figure 3.14 for the overlapping inhomogeneities in periodic lattices. In a time-resolved MOKE experiment, also modes extending across several unit cells, hence 'feeling' the periodic potential, are induced by the structure. These will be presented in detail in section 3.5.3 (Bloch modes in magnonic crystals). The parts (middle) and (right) of figure 3.21 display two major differences. The difference of the two antidot arrays being the filling fraction $f$ of 2.2% and 6.4%, respectively, the relative amplitude of the localized modes changes when compared to the uniform precession. Resulting from the larger perturbance by the lattice in figure 3.21 (right), the localized mode dominates the spectrum over a wider field range than in figure 3.21 (middle). The area of inhomogeneous internal field grows with the

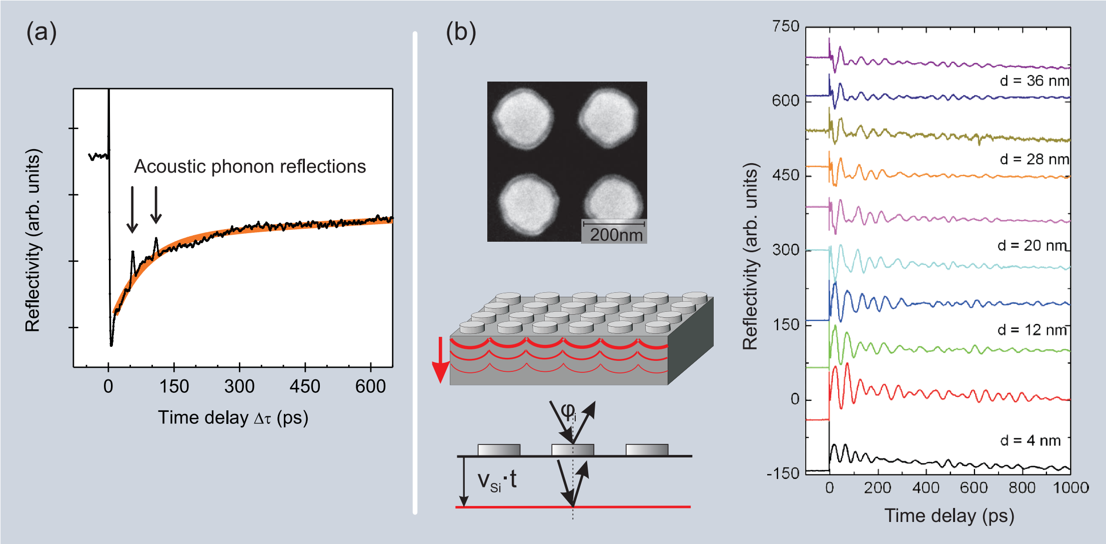

**Figure 3.23 – Effect of acoustic phonons.** (a) Ultrafast heating of the surface of an antidot-structured nickel film generates a stress wave which is reflected at the substrate, as seen at a delay of 70 and 140 ps as a sharp peak. This film was structured with $a = 3.5\,\mu\mathrm{m}$ and $d = 1\,\mu\mathrm{m}$. Because of the low filling fraction, the lateral heating is homogeneous and no acoustic phonons are excited parallel to the surface which interfere with the magneto-optical measurements. (b) In the case of nickel dots on an Si substrate the traced reflectivity changes show strong oscillations that can be attributed to a standing acoustic wave governed by the periodicity of the structures (reproduced from reference [MEW+08]).

filling fraction so that the observed increase in amplitude further supports the localized interpretation of the non-dispersive modes.

Another possible explanation for a dominantly field-independent mode is to attribute this to a non-magnetic effect, the phonon surface wave of the thin metal film. Corresponding measurements of the time-resolved reflectivity are shown in figure 3.23 and reveal the propagation and interfacial reflection of heat-induced stress waves normal to the film plane described, which can interfere with the measured transient Kerr rotation [DLM+06]. Though small oscillations are visible on longer timescales, they do not account for the large amplitudes observed and described earlier and are at a different frequency.

Additionally, with the velocity of sound of the respective materials, the frequency of possibly excited standing phonons can be estimated: assuming the basic mode of phonons with a wave length of $\lambda_{\mathrm{phonon}} = 2a = 7\,\mu\mathrm{m}$ and using $v_{\mathrm{Ni}} = 4900\,\mathrm{m\,s^{-1}}$ as the sound velocity in nickel, one finds an expected phonon frequency of 0.7 GHz. Lateral acoustic phonons in the silicon substrate ($v_{\mathrm{Si}} = 8433\,\mathrm{m\,s^{-1}}$) have an expected frequency of 1.2 GHz. As a consequence, acoustic phonons as an origin for the field-independent modes can be ruled out.

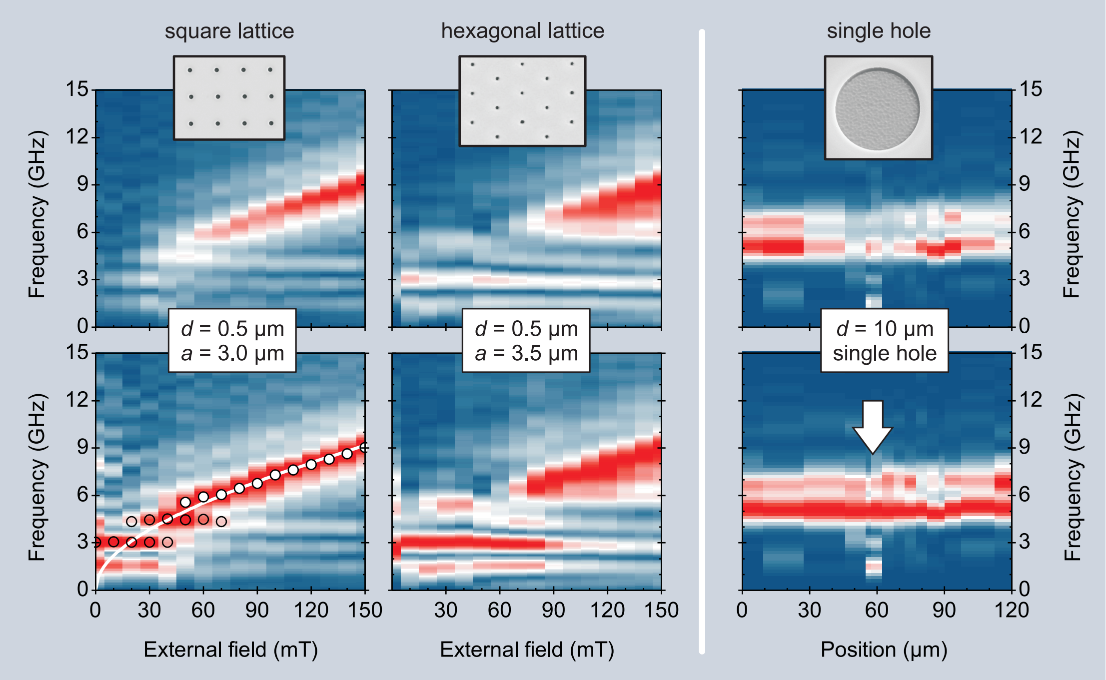

**Figure 3.24 – Effect of the antidot lattice geometry measured by all-optical spin-wave excitation and detection.** Left: square lattice. Middle: hexagonal lattice. Right: mode spectrum around a single hole structure for $\mu_0 H_{\mathrm{ext}} = 30\,\mathrm{mT}$. By scanning the laser spot across a single antidot, also here a mode at low frequencies is found that solely exists around the antidot.

The peaks as seen in figure 3.23(a) arise from the stress waves reflected at the film-substrate interface and clearly do not appear in the Kerr spectra, which is a sign that there is no crosstalk of the signal here. A reason is that the filling fraction is very low, and thus, the whole surface is heated equally.

The different possible contributions to the transient signal have been discussed by Müller et al. [MEW$^+$08] and reproduced in figure 3.23(b). In their case, a metallic dot array produced by optical interference lithography was investigated all-optically; the small dots heat up very fast, while the Si substrate keeps cold. The large difference in expansion creates surface acoustic waves with large amplitudes that can be matched to the inter-dot distance, which serves as a periodic lattice for the surface acoustic waves. This poses a clear difference to antidot experiments.

It is also possible to examine other, more complex symmetries than the simple square geometry; then the spin-wave modes in the structured media should mirror the lattice symmetries if they are not only determined by the potential around a single antidot, but interacting with the next-neighbor antidot mode. Static measurements of hysteretic properties and electronic transport have been

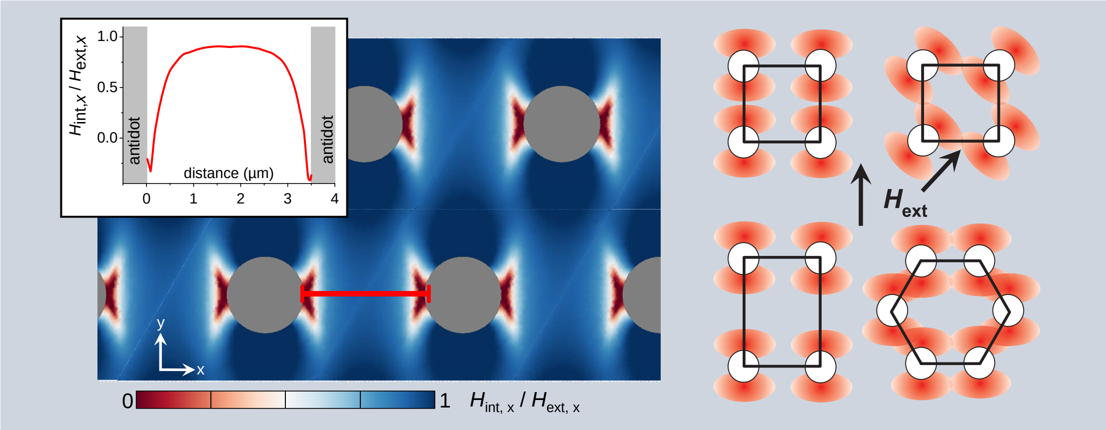

**Figure 3.25 – Internal field and spin-wave localization.** Calculation of the total internal field (left) in a hexagonal structure at $\mu_0 H_{ext} = 90\,\mathrm{mT}$ for lattice periodicity $a = 3.5\,\mu\mathrm{m}$ and antidot diameter $d = 1.36\,\mu\mathrm{m}$. The inset shows the values for a cut along the red line. Schematics of the internal field distribution (right) for square lattice with field along (0,1), (1,1), tetragonally distorted and for a honeycomb lattice.

performed and resemble the respective lattice symmetries [WAS06]. According dynamic experiments are shown in figure 3.24. They reveal that localized modes are also observed on hexagonal lattices (figure 3.24 (middle)). The mode distance in frequency of about 1.5 GHz seems very similar for the square and the hexagonal lattice. It is solely determined by the antidot diameter. The reader may note the slightly increased periodicity in the case of the hexagonal lattice in order to maintain the filling fraction of approximately 2%. Also shown in figure 3.24 (right) are measurements determined on a single antidot. For a fixed external field, the Fourier power is color-coded as a function of position and frequency. At the position of the single antidot (marked by an arrow), additional modes can be seen. This supports the picture that these low-frequency magnetic modes are localized at single antidot edges.

To get a better understanding, we will first discuss the internal field distribution around an antidot site in these lattice geometries, and then show more detailed angular-dependent experiments. In figure 3.25, a calculation of the total internal field in a hexagonal structure at $\mu_0 H_{ext,x} = 90\,\mathrm{mT}$ for lattice periodicity $a = 3.5\,\mu\mathrm{m}$ is shown. The inset reveals that strong changes of the internal field up to distances of $0.5\,\mu\mathrm{m}$ from the dot are found. In the same figure on the right, schematics of the internal field minima for different lattices and magnetic field direction are drawn to illustrate a possible interaction of modes located in these minima.

For honeycomb lattices, one expects to find the 6-fold rotational symmetry

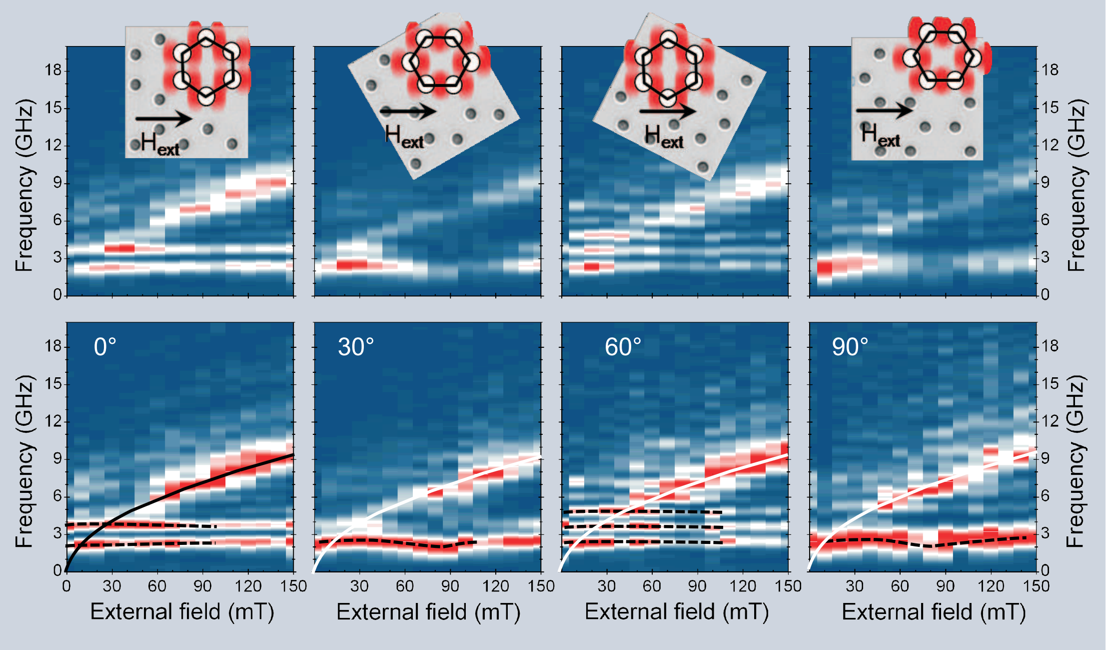

**Figure 3.26 – Effect of the antidot lattice geometry measured by all-optical spin-wave excitation and detection.** The honeycomb lattice is rotated: for 0° and 60°, the mode-splitting in energy is low. A weak localization is found. For 30° and 90°, only one mode is found and the mode splitting in energy is high. In the schematic picture, a blocking of the Damon-Eshbach wave propagating perpendicular to $H_{\text{ext}}$ is observed (strong overlap of the red areas which represents a drop of the internal field).

which coincides with a 60° repetition of the spin-wave pattern. Here, when compared to hexagonal lattices, regions of rather homogeneous internal field are coexistent with closely packed antidots. Again, when rotating the sample around the film normal, by tilting the structure with respect to the applied field, the behavior of the localized modes can be controlled. Respective measurements are presented in figure 3.26 and display the expected symmetry. As expected, the data for the angles 0° and 60°, as well as 30° and 90° show the same features: opposite to the first two 0° and 60°, for 30° and 90° only one dominant mode is found. The SEM pictures in the insets illustrate the drop in the internal field around the antidots.

By rotation of the sample, the overlap between neighboring antidots changes. In the schematic inset, it can be seen that as the overlap in the 30° and 90° is larger, the areas of localization come closer. This results in the observation of a higher Fourier power intensity of the localized, non-dispersive modes and goes with a reduction of the Kittel amplitude for both spectra at angles 30° and 90°, respectively. Only one dominating mode is observed all up to $\mu_0 H_{\text{ext,x}} = 150\,\text{mT}$. Saturation fields of the films are not changed by structuring; they still

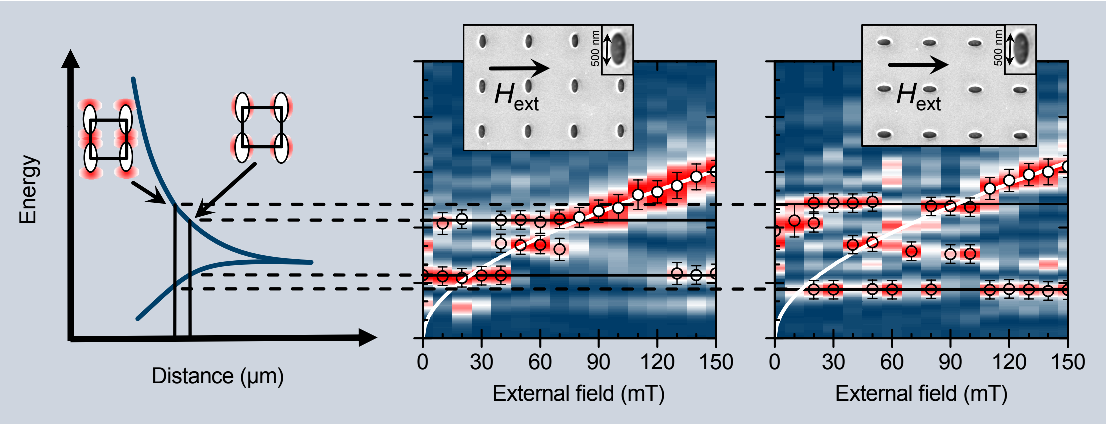

**Figure 3.27 – Effect of the form factor in elliptical hole structures in a square lattice.** Tuning of the interplay between magnetic modes localized at adjacent elliptical antidots can be achieved by making use of the structure's anisotropy. Aligning the larger semi-axis with the external field increases the inter-antidot coupling which in turn yields a larger localization. The frequency width is found to increase. This effect is schematically drawn on the left. Semi-axes are 250 nm and 500 nm, the square lattice has a periodicity of 3.5 µm.

remain at around $\mu_0 H_{\text{ext,x}} = 10\text{-}15\,\text{mT}$. Simulations for a Py honeycomb lattice have been presented [TMG+10]. These reveal the effect of the strong interaction between next-neighbor dots that is responsible for the formation of spin-wave channels through the structure. The dynamic modes map the inhomogeneities of the internal field – which means that they have a dominantly localized nature.

The effects of a changing overlap and crystal symmetry can also be controlled through use of elliptical holes instead of circular antidots. The ellipses have an anisotropic dipolar field extending into the film for fields applied along the short axis as compared to fields applied along the long axis. For the modes localized at the field inhomogeneities around the antidots, this means a different extension to the next unit cells, then 'feeling' the periodic potential and symmetry created by the structure. This overlap is responsible for the considerable changes in the relative Fourier power of the localized and uniform modes in figure 3.27, depending on the orientation of the external field.

The structure consists of elliptical holes with semi-axes of 250 nm and 500 nm, respectively, arranged on a square lattice with a periodicity of 3.5 µm. First, one observes a change in relative amplitude of the Kittel mode with the angle between external field and lattice. Second, two branches of constant frequency occur in figure 3.27. They are separated by several GHz and can be shifted by the angle of the applied field. The separation of the modes is large for the magnetic field applied along the long axis of the ellipse. Bearing in mind the localized character,

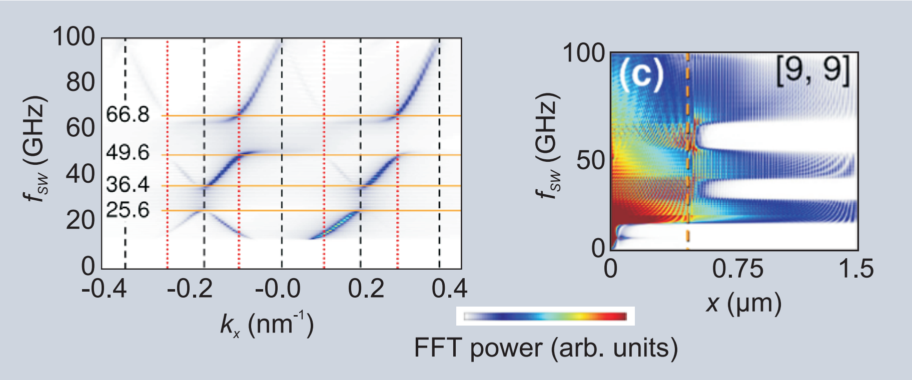

**Figure 3.28 – Micromagnetic simulation of a one-dimensional magnonic crystal: Py stripe with alternating width.** Forbidden region (magnonic gaps) in frequency result in a frequency-filter effect for transmitted waves. The transmission into the structured region is not allowed and the intensity in the gap region drops down very rapidly (adapted from reference [LHK09]).

this behavior can be understood: by tilting the lattice with respect to the external field, the distance between two localization sites is reduced and the splitting of modes can be controlled. This is in close analogy to collective modes as observed in arrays of nanomagnets by Kruglyak et al. [KKN+10]. The frequency shift controlled by field direction and lattice geometry allows to deduce that also the localized modes are more than the single mode at one antidot and thus of magnetic origin. Further studies therefore need to include a local mode mapping around the antidots to investigate the nature of these modes unambiguously.

### 3.5.3 Bloch modes in magnonic crystals

If one wants to study spin-wave materials closer to the 'free-electron' case, two preconditions must be fulfilled: first, the propagation length of the spin waves must extend across multiple unit cells. In terms of a resonance this leads to the formation of a narrow band of states in $k$-space. Gubbiotti et al. demonstrated in their recent work a magnonic band-gap spectrum in 2D magnonic crystals with submicrometer periods [GTM+10]. In general, the formation of a band depends on the spin-wave propagation. For Ni, with a Gilbert damping parameter of $\alpha = 0.02$, the propagation length from phase velocity can be estimated to approximately 10 µm. CoFeB has a low damping with $\alpha = 0.006$. Thus, the spin-wave propagation length is larger than 100 µm. For YIG, with $\alpha = 6 \times 10^{-5}$ even millimeters can be reached. The second precondition concerns the scattering potential, which must be weak. Already a filling fraction of 0.1 means that the holes in the film make 10% of the material. However, the distortion in the internal field is much larger. It will extend a factor two in radius; this variation of the internal field

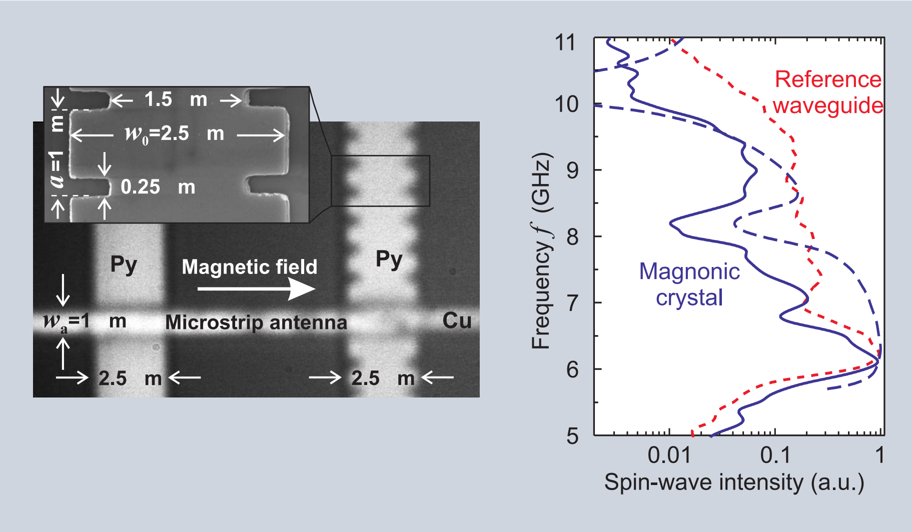

**Figure 3.29 – Experimentally measured transmission of a one-dimensional magnonic crystal: Py stripe with alternating width.** A breakdown of the transmitted intensity by more than a factor of 10 is observed at 8.4 GHz (adapted from reference [CPS+09]).

being different from the homogeneous case results in an effective filling fraction which is much larger.

Very nice examples can be found for spin waves propagating in one-dimensional stripes: strong rejection bands are formed. The influence of a zig-zag configuration of the magnetization results in a periodically alternating magnetization. Topp et al. showed that spin-wave confinements are also found [TPHG08]. Magnonic gaps in the band structure have been impressively demonstrated in a one-dimensional magnonic material by Chumak et al. [CPS+09, CSW+09]. Periodic grooves were mechanically drilled into a ferrite-based wave guide. The transmission shows certain frequency bands determined by their periodicity, while the groove depth in the material determines the transmitted power leading to rejection efficiencies of 30 dB (contrast of 1/1000). Even in a standard ferromagnet such as permalloy, by simply increasing the width of the wave guide, thus changing the contrast in the periodic energy landscape, a gradual opening of a magnonic gap was realized.

In the case of one-dimensional systems, the filtering effects in width-modulated stripes have been simulated by Kim [LHK09, Kim10] and subsequently measured by Chumak [CPS+09]. Both are reprinted in figures 3.28 and 3.29. The distance is in the nanometer range. Clearly, this falls into the exchange dominated spin-wave dispersion. It can be nicely seen, that the bands calculated in the micromagnetic mode, show a quadratic dispersion which is very similar to a free-electron dispersion. Due to the periodic modification of the width, the gaps opening up span

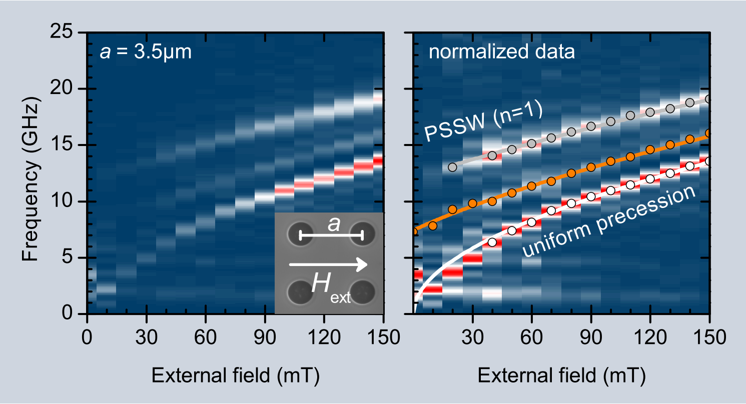

**Figure 3.30 – Bloch modes in a CoFeB antidot lattice.** In a continuous film (not shown), only the mode of uniform precession and a first order standing spin wave (PSSW) can be found. In a structured film, an additional mode appears (orange line and points), whose wavelength is determined by the wave vector at the Brillouin zone boundary, $k = \pi/a$.

multiple GHz. The transmission into the structured region is not allowed. In figure 3.29, experimental results from Chumak et al. are displayed for a permalloy wave guide. Clearly, a drop in transmission not as high as in YIG, but also by a factor of 1/10, is observed.

The effect of two-dimensional structures on propagating modes was studied by Neusser by vector network analyzer-FMR [NBG08]. We will present a study here as well, using all-optical spin-wave excitation and detection in a low damped CoFeB film. Figure 3.30 shows spectra of a structured CoFeB film (thickness $t = 50\,\text{nm}$), measured by means of TRMOKE. In an unstructured film with the same thickness, one can identify two modes which are the uniform precession mode and the first order standing spin wave. The structure (square antidot lattice with lattice constant $a = 3.5$ µm, field applied along lattice side) alters the dispersion, and introduces band gaps at the zone boundary which is at $k = \pm\pi/a$.

Due to a diminished slope of the dispersion at this point, one here finds an increased density of states. The fingerprint of this effect can be seen in the measured spectrum in figure 3.30, where a new mode appears which obeys the dispersion of a Damon-Eshbach-mode with $k = \pm\pi/a$. Since for $t \ll a$ the mode profiles for both directions (±90° with respect to the field) are essentially constant and the dispersion is degenerate with regard to this directions, a superposition of both spin waves yielding a standing wave is most likely. When the field is applied in an angle of 45° with respect to the antidot lattice (see figure 3.31), the appropriate dispersion for the same propagation direction with respect to lattice yields again $k = \pm\pi/a$, and is now fourfold degenerate (±45°, ±135° with respect to

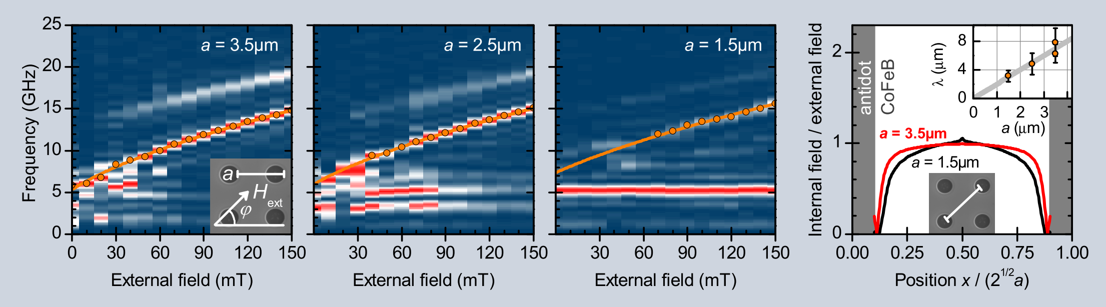

**Figure 3.31 – Dominant Bloch modes under 45°.** For a magnetic field applied under 45°, Bloch modes in a CoFeB antidot lattice by the wave vector at the Brillouin zone boundary $k = \pi/a$ dominate the spectrum. The antidot lattice is varied as a function of the lattice distance for the same filling fraction. Upon reduction of the lattice constant, a mode appears that hardly depends on the magnetic field.

the field). The degeneracy accompanied by an increase of the density of states results in the observation that only the Damon-Eshbach modes are populated after optical excitation.

These modes are examples for delocalized, extended Bloch-modes, whose excitation and detection in non-frequency and non-$k$-selective experiments become possible due the artificially altered band structure.

### 3.5.4 Magnonic wave guides

We have discussed the possibility of completely different behavior of photons in a photonic wave guide. So called “slow photons” may emerge that propagate in the way of the religious procession of Echternach, i.e., three steps forward and two steps backwards, similar to pictures drawn in a Krauss article [Kra07]. Effectively, the propagation is slowed down which ultimately is a signature of the periodic potential. Other features like band-gap formation allow for the achievement of photonic resonators with highest $Q$-factors. Moreover, wave guides embedded in a structured material allow to facilitate the guidance of photons around corners or the splitting of wave packages into two. In the introduction, we have already discussed the differences between optical and spin-wave guides: in the latter, the internal field may result in a localization of the spin-wave modes. This can be very different for magnonic wave guides.

Mapping the ideas from photonics to magnonics is not straightforward. Strong differences are found in the anisotropy of the band structure. A Bloch state with the period of the lattice will be a standing wave at the zone boundary. However, the mode perpendicular to it will not feel the same confinement. By removing one row of the holes, the localized state may propagate along this defect, while

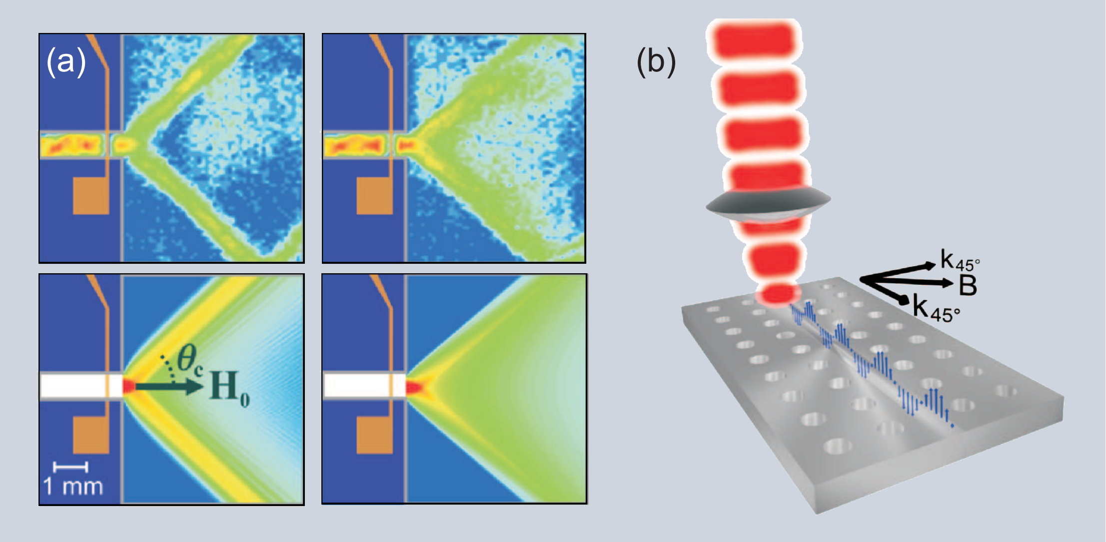

**Figure 3.32 – Spin-wave caustics.** (a) Observed with BLS is a beam-like propagation (from reference [SSC+10]). (b) An artist's view of a magnonic spin-wave guide: femtosecond laser pulses allow to seed spin waves freely by moving the laser spot, hence "photo-magnonics". Depicted is the situation for the external field applied under an angle of 45° with respect to the antidot lattice.

for the perpendicular state the situation remains unchanged. A solution is to apply the field under 45° with respect to the defect, as depicted in an artist's view in figure 3.32(b). Then the states perpendicular and parallel to the channel will have the same dispersion and thus show the same standing-wave behavior of modes with $\boldsymbol{k}$ at the zone boundary (in close analogy to figure 3.31).

Simpler wave guides have been discussed in the beginning (figure 3.1) and even beam-like propagation can be realized by spin-wave caustics as reproduced in figure 3.32(a) [SSC+10, DDB+09]. We have performed experiments on a 'line defect' which means one missing line in the magnonic crystal. First experiments of this kind are shown in figure 3.33. Scanning the probe beam across the defect shows magnetic modes inside the magnonic wave guide that are otherwise lower in intensity in the structured material. While this reveals the feasibility of the experiments, future approaches probing the modes propagating in the wave guides need to take into account the anisotropic magnon dispersion with respect to the external field. Especially, the mode velocity and propagation length as well as the scattering between modes with $\boldsymbol{k}$ parallel or antiparallel to $\boldsymbol{M}$ and $\boldsymbol{H}_{\text{ext}}$ will be a focus aim. An absolute advantage of photo-excitation and detection of spin waves becomes evident here: excitation and detection can be freely moved in the structure by moving the two laser spots (in the experiment 60 µm for the pump pulses and 14 µm for the detection were used here).

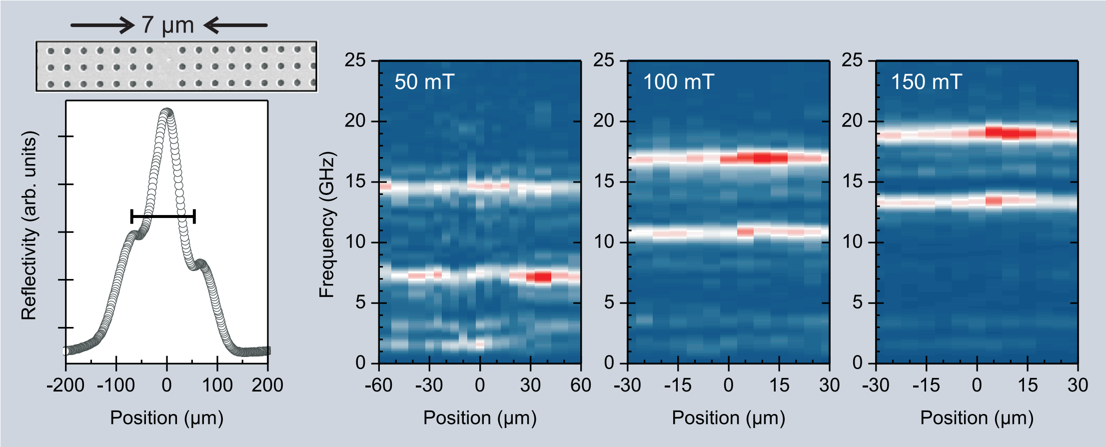

**Figure 3.33 – Magnonic spin-wave guide.** Prepared by FIB: a 'line defect'. Below: position of the wave guide scanning with the pump beam in the reflectivity data. Right: magnetic spectra for different field values scanning the position of the probe beam.

## 3.6 Outlook: controlled spin-wave localization

We have described in our review the possibilities of spin waves in artificially structured media: thereby, we started with novel concepts of spin-wave computing; we described the peculiarities of spin-wave guides compared to optical wave guides; and then, we switched to the effect of structuring materials – what are the conditions and solution of forming novel states. To develop grounds for different types of spin-wave materials, we repeated basic concepts of solid state physics of band formation of electrons, and clearly distinguished between the case of a small perturbation – starting from a freely propagating wave – and the tight binding case. We show that similar concepts can be applied to magnonic crystals. Experimentally, one finds both localization effects and wave vectors that correspond to a Bloch mode at the zone boundary originating from the periodicity of the antidot lattice.

What kind of development may be projected into the future? One major difference compared to photonics is that the peculiar shape of the magnetic potential forming at each antidot has a rich complexity. While for the photonic case, the index of refraction is given by the alternating material itself and can be changed only in small fractions, the filling fraction in the magnonic case extends the inter-material border since it is given by the dipolar interaction distorting the internal fields around the antidot which even can be changed by rotating the applied magnetic field. The minima in internal fields, where spin waves localize, can be designed by the antidot shape, as we have demonstrated for elliptical antidots.

By changing the applied field, the potential landscape can be rotated: the overlap of the localized states is changed. One can compare this situation with the tight binding approach. Each ‘atom’ is defined by the shape of the dipolar fields which allows certain solutions of the spin-wave function. These ‘atomic’ spin functions can then be used as a basis set to model the interactions of the emerging localized spin-wave crystal, which may have interesting features, to model correlation effects in correlated materials.

Similar ideas have been successfully applied to lattices of single atoms in atomic physics. It would be interesting to see if such concepts could apply here, as well. For example, the external applied field could gradually change the overlap, e.g. ‘hopping’ between the localized spin-wave orbital wave functions. However, such ideas are more farsighted. Current experiments will have to show that low damping materials will improve the quality of spin-wave crystals and formation of Bloch states. Furthermore, different material combinations need to be explored to go beyond the antidot lattice case. Spin-wave computation and spin-wave data transmission have to be developed to go beyond the proof of principle and to show that indeed a high data throughput may be an advantage of spin-wave based computation in the future.

## Chapter 4

# Spin-wave modes and band structure of rectangular CoFeB antidot lattices

B. Lenk, N. Abeling, J. Panke, and M. Münzenberg

Journal of Applied Physics **112**, 083921 (2012)
DOI: 10.1063/1.4759142

**Abstract.** We present an investigation of rectangular antidot lattices in a CoFeB film. Magnonic band structures are numerically calculated, and band gaps are predicted which shift in frequency by 0.9 GHz when rotating the external field from the long to the short axis of the unit cell. We demonstrate by time-resolved experiments that magnonic dipolar surface modes are split in frequency by 0.6 GHz which agrees well with the theoretical prediction. These findings provide the basis for directional spin-wave filtering with magnonic devices.

## 4.1 Introduction

The use of spin waves opens up routes to new computing devices with advantages over today's CMOS-based technology. Although magnetic damping is comparably high (requiring small-scale devices), Joule's heating caused by electron currents is avoided [KBW10b]. Much research has been devoted to interferometer-like structures [SSL+08], inspired by the possibility of (local) spin-wave phase manipulation by Oersted fields [KSS+05]. On the other hand, effective spin-wave filters can be designed on the basis of ferromagnetic stripes with modulated widths [LHK09, CPS+09, CCG+12]. One concept of spin-wave excitation and detection is based on rf-antennas which, however, cannot be put in arbitrary proximity, due to inductive coupling. If, instead, the excitation was achieved by intense light pulses as implemented in heat-assisted recording in modern hard disc drives [KGM+08, SSP+10], only one antenna would be needed for detection. Hence, effective mechanisms for spin-wave selection from the broad-band (laser) excitation are required. It has been shown that magnonic crystals inhibit the necessary features [NTT01, KDG10, GTM+12, LUGM11]: two-dimensional antidot lattices show Bloch-like modes with a distinct wave vector, which is in turn tunable by the magnonic lattice parameter [ULM10]. These modes propagate in the Damon-Eshbach (DE) geometry, i.e., with the wave vector $k_{\mathrm{DE}}$ perpendicular to the external magnetic field $H_{\mathrm{ext}}$ [DE61]. They have for example been used for spin-wave imaging [MTM+12].

A transition between different magnonic crystals may allow the scattering of one magnonic mode into another. In particular, when propagation takes place across a (one-dimensional) interface, spin-wave tuning or filtering is viable, if the magnonic lattices in question are of similar character. This can be achieved in rectangular lattices, i.e., if the orthogonal unit vectors of the antidot lattice $a_1$ and $a_2$ differ in length. In such magnonic materials we demonstrate experimentally how the lattice anisotropy can be employed to change the spin-wave characteristics. A rotation of the magnetic field from along the long axis of the rectangular lattice to the short axis allows to decrease the spin-wave frequency by $\approx 0.6\,\mathrm{GHz}$ rerouting the spin wave by 90°. Namely, we observe spin-wave splitting at the Brillouin zone boundary which opens routes to magnonic spin-wave filter devices tunable by rotating the magnetic field.

## 4.2 Simulations

In order to develop a theoretical understanding, band structure calculations are performed, the numerical formalism of which has been presented in detail in reference. [LUGM11]. In brief, the Landau-Lifshitz-Gilbert (LLG) equation of motion is solved by a plane-wave method as developed by Puszkarski and co-workers [VDDRP96, KP08]. For the case of a thin ferromagnetic film, dynamic magnetic modes can be – under neglection of the exchange interaction – assumed to be uniform across the film thickness [HP95]. In the lateral direction, the periodic modulation of the sample's magnetization between film and antidots is achieved by a Fourier synthesis [VDDRP96],

$$M_{\mathrm{S}}(\boldsymbol{r}) = \sum_{\boldsymbol{G}} M_{\mathrm{S}}(\boldsymbol{G}) e^{i\boldsymbol{G}\boldsymbol{r}}, \tag{4.1}$$

where $\boldsymbol{G}$ is a two-dimensional vector of the reciprocal lattice. The profile of $M_{\mathrm{S}}$ which has been used in the calculations is plotted as a black line in figure 4.1(a). The constituting reciprocal lattice vectors are shown in figure 4.1(b). These provide a compromise between a desirably well approximation of the stepwise magnetization profile on the one hand, yet fulfilling the initial assumption of mode uniformity ($\lambda \gg t$, with spin-wave length $\lambda$ and thickness $t$) on the other hand.

Other parameters in the calculations were $\mu_0 M_{\mathrm{S}} = 1.6\,\mathrm{T}$, $\mu_0 H_{\mathrm{ext}} = 130\,\mathrm{mT}$, and $g = 2.04$. An antidot lattice with $a_1 = 3.5\,\mu\mathrm{m}$ and $a_2 = 2.5\,\mu\mathrm{m}$ was the basis for both the calculations as well as the experiments to be discussed later in this

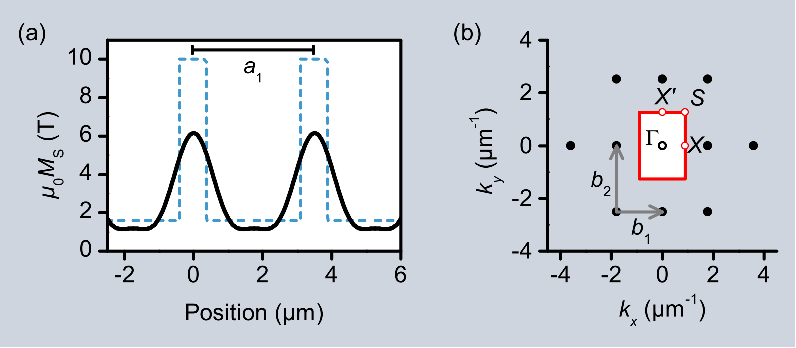

**Figure 4.1 – Uniform mode analysis in rectangular antidot lattices.** (a) Calculated magnetization profile using equation (4.1) along a high-symmetry direction (solid black line). The lattice parameter $a_1 = 3.5\,\mu\text{m}$ is depicted as well as the idealized profile (blue dashed line). In (b), the respective reciprocal lattice vectors in Fourier space are plotted (black points). The Brillouin zone boundary is given by the solid red line, high symmetry points $\Gamma$, $X$, $S$, and $X'$ are marked in white. Reciprocal lattice unit vectors (gray arrows) are $b_1 = 2\pi/a_1$ and $b_2 = 2\pi/a_2$, respectively.

manuscript. Plotted in figure 4.2 are the numerically obtained results of the band structure calculations. In (a), the band structure of a continuous film is presented which is modeled in the limit of antidot radius $R \to 0$, with unchanged lattice parameters $a_i$. The external field was applied parallel to $a_2$ and a folding of the Damon-Eshbach dispersion into the first Brillouin zone is found as expected from solid state theory (orange line).

A finite antidot radius of $R = 400\,\text{nm}$ leads to the magnonic band structures shown in figures 4.2(b) and (c). For the two plots, the external field was applied along either of the unit vector directions of the antidot lattice. The paths to the $X$- and $X'$-points in reciprocal space hence correspond to DE surface waves propagating perpendicular to $H_{\text{ext}}$ and $M_{\text{S}}$. When approaching the Brillouin zone boundary, the bands for these modes flatten out and culminate in band gaps at $X$ and $X'$ as marked by the black ellipses in the graph. By means of the aspect ratio of the rectangular lattice vectors, also the energy (i.e., frequency) of the Bloch-like modes at $X$ and $X'$ can be shifted: given the condition $k_{\text{DE}} = \pi/a_i$ the DE-frequency will change when changing $a_i$, i.e., when propagation of the DE modes is along either of the two lattice unit vectors. Namely, a frequency shift of 0.9 GHz is calculated.

## 4.3 Experiments

In the following we will describe an experimental evaluation of the numerical results using femtosecond laser pulses. An all-optical approach was utilized, where one can make use of the very broad band, neither frequency- nor $k$-selective excita-

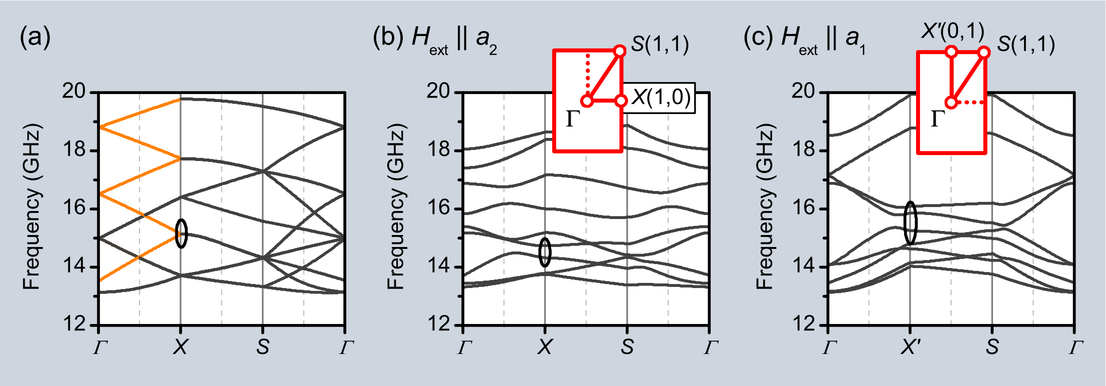

**Figure 4.2 – Numerically calculated band structures for rectangular magnonic crystals in a CoFeB matrix.** In (a), the continuous film is presented with a vanishing antidot radius $R = 0$, maintaining the periodicities $a_1 = 3.5\,\mu\mathrm{m}$ and $a_2 = 2.5\,\mu\mathrm{m}$. The external field is applied parallel to $a_2$ and a folding of the Damon-Eshbach dispersion into the first Brillouin zone is observed (orange line). Plots in (b) and (c) show the band structures for a non-vanishing radius $R$ =400 nm and $H_{ext}$ applied along $a_2$ and $a_1$, respectively. The insets illustrate the geometry, where the dotted red lines depict the direction of $H_{ext}$. For spin-wave propagation perpendicular to $H_{ext}$ and $M_S$, i.e. in the Damon-Eshbach geometry, band gaps open up at the $X$- and $X'$-points (black ellipses). These shift in frequency by 0.9 GHz.

tion of spin waves [KH06, BWM⁺06, WDL⁺08]. In principle, such an experiment will show those spin-wave modes with the highest density of states (DOS). According to general solid state theory, the flattened bands found above should lead to an increased DOS and should therefore resemble the rectangular anisotropy. Since the bands shift in figure 4.2, a change of the DOS should be experimentally observed in an altered population of spin-wave modes. For the experiments, a $Co_{20}Fe_{60}B_{20}$ film with a thickness of $t = 50\,\mathrm{nm}$ was magnetron-sputtered onto a Si(100) substrate and passivated with 3 nm of ruthenium. With a focussed beam of Ga-ions (FIB) a rectangular magnonic crystal was created using the same structural parameters $\{a_1, a_2, R\}$ as in the calculations. The overall size of the structured area was $150 \times 150\,\mu\mathrm{m}^2$, considerably larger than the pump and probe laser spot sizes in the experiment (60 µm and 15 µm, respectively). In figure 4.3(a) an SEM image of the sample is shown.

Data analysis followed a scheme as presented in reference [LEHM10]. We refrain from plotting reference data on a continuous CoFeB film here. These have already been shown in [ULM10] for an identical specimen. Plotted in figure 4.3(b) and (c) are the Fourier-analyzed TRMOKE data as recorded on a rectangular antidot lattice milled into a CoFeB film. Depicted by the SEM insets is the orientation of the external magnetic field $H_{ext}$ with respect to the two-dimensional magnonic crystal.

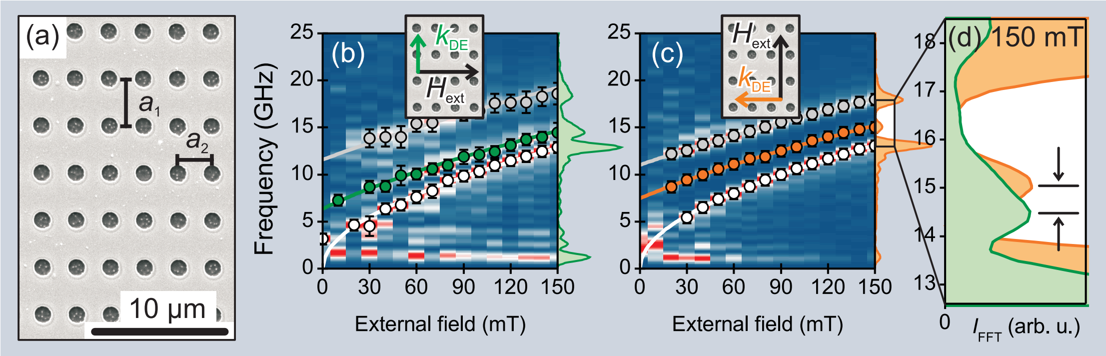

**Figure 4.3 – Experiments on magnonic spin-wave modes in rectangular antidot lattices.** In (a), an SEM image of the structured CoFeB film with $a_1 = 3.5\,\mu\mathrm{m}$, $a_2 = 2.5\,\mu\mathrm{m}$, and $R = 400\,\mathrm{nm}$ is given. The plots (b) and (c) show the Fourier power of the magnetic precession observed after optical excitation with fs-laser pulses. The peak positions have been determined and are given by the points (white: uniform precession; gray: PSSW; green and orange: magnonic Damon-Eshbach mode). The fitted dispersion curves are represented by solid lines [LEHM10]. Detailed in (d) is the frequency shift of the magnonic Damon-Eshbach mode at an applied field of $\mu_0 H_\mathrm{ext} = 150\,\mathrm{mT}$ between the cases $H_\mathrm{ext} \perp a_1$ and $H_\mathrm{ext} \perp a_2$. It accounts to $0.55 \pm 0.04\,\mathrm{GHz}$ and agrees reasonably well with the simulations from figure 4.2.

The points in figure 4.3(b) and (c) represent the peak positions and are attributed to the uniform ($k = 0$) Kittel mode (white), the exchange-dominated perpendicular standing spin waves (PSSW, gray), and the magnonic Bloch-like DE-modes exclusively excited on periodically structured samples (green: $H_\mathrm{ext} \parallel a_2$, and orange: $H_\mathrm{ext} \parallel a_1$). We would like to emphasize that while PSSW and Kittel modes are the only ones observed on a continuous film, the DE-modes originate from the magnonic crystal's periodicity in the propagation direction (perpendicular to $H_\mathrm{ext}$ and $M_\mathrm{S}$) [ULM10]. Also included as correspondingly colored solid lines are the theoretically expected dispersions [LEHM10, LUGM11]. For simplicity, here we only state the dipolar Damon-Eshbach dispersion which reads [DE61]

$$\left(\frac{2\pi f_\mathrm{DE}}{\gamma\mu_0}\right)^2 = H_x\left(H_x + M_\mathrm{S}\right) + \frac{M_\mathrm{S}^2}{4}\left(1 - e^{-2|k_\mathrm{DE}|t}\right). \tag{4.2}$$

Therein, $t$ is the thickness, $\mu_0 M_\mathrm{S} = 1.6\,\mathrm{T}$ is the saturation magnetization as stated above, and $H_x = H_\mathrm{ext}\cos\phi$ is the projection of the canted external field onto the film plane ($\phi = 30°$ for the experiments presented here). Therefore, as the only free parameter the wave vector $k_\mathrm{DE}$ remains.

Given by the solid green and orange lines is the fit of the Damon-Eshbach dispersion (4.2) to the experimentally determined dispersion $f_\mathrm{DE}(H_\mathrm{ext})$. In both cases of $H_\mathrm{ext} \perp a_i$ $(i = 1, 2)$ the fits yield the Damon-Eshbach wave vectors $k_{\mathrm{DE},1} =$

$0.87 \pm 0.07\,\mu\mathrm{m}^{-1} = 0.97 \times \pi/a_1$ and $k_{\mathrm{DE},2} = 1.23 \pm 0.07\,\mu\mathrm{m}^{-1} = 0.98 \times \pi/a_2$. Hence, not only can one single magnonic mode be defined in the structures [ULM10]. Instead, merely changing the relative orientation between external field and antidot lattice by 90° is sufficient to excite a different magnonic spin-wave mode. This is accompanied by a frequency shift further detailed in figure 4.3(d) which contains the Fourier spectra of the TRMOKE measurements performed at $\mu_0 H_{\mathrm{ext}} = 150\,\mathrm{mT}$. The shift of the magnonic mode's frequency is marked by the black arrows and accounts to $0.55 \pm 0.04\,\mathrm{GHz}$, which is similar to the value expected from the calculations in figure 4.2.

## 4.4 Discussion and conclusions

The bosonic character of spin waves becomes apparent in the condensation-like excitation in the TRMOKE experiment [DM07]. As a consequence, selected spin-wave excitation is possible and processing schemes which employ the spin-wave propagation for manipulation purposes on top of mere transport can be applied [SSL+08, KBW10b]. In view of the results presented in this manuscript, the interplay between the intrinsic anisotropy of the dipolar modes' dispersion $\omega|_{k \perp M} \neq \omega|_{k \parallel M}$ and the (rectangular) anisotropy stemming from the magnonic crystals can further be employed. Namely, frequency splitting of spin waves becomes feasible, with the direction of the applied magnetic field as the external control parameter. By means of the magnetic field, the propagation direction of the spin waves is changed, accompanied by the frequency shift described above.

In conclusion, we expect from numerical calculations the opening of magnonic band gaps in the Damon-Eshbach geometry and verify this with TRMOKE results that show the optical excitation of dynamic modes with wave vectors at the Brillouin zone boundary. Thus, a controlled excitation of selected spin waves can be achieved by rotation of the external field. In a more farsighted view, interfaces between respective magnonic crystals provide interesting perspectives: a reflection of spin waves may be observed due to an abrupt change of the magnonic index of refraction [KBW+10a, NBD+11]. Similarly, the spin-wave splitting observed here hints towards directional switching devices for spin waves defined by rectangular (i.e., anisotropic) magnonic crystals.

## Chapter 5

# General discussion

The present thesis elusively discusses the excitation, detection, and manipulation of spin waves. Chapter 2 is dedicated to the principle processes of spin-wave excitation with laser pulses and the mechanisms leading to the population of selected spin-wave modes. In contrast to other experimental approaches, the neither $k$- nor frequency-selective optical excitation allows to gain an insight into the spin-wave density of states. This quantity can then be tailored in magnetic metamaterials, as described in chapter 3.

Depending on the investigated material, magnonic crystals show a variety of effects. These include analogies to atomic physics, namely the splitting of energy/frequency levels as well as band-formation and Bloch states known from solid state physics. All of these effects can be investigated with light (i.e., laser pulses) which demonstrates the versatility of the sub-field called *photo*-magnonics.

Remaining challenges and possible applications are already discussed in detail in section 3.5.2 and shall not be repeated here. Instead, from the findings in chapter 4, an important point can be made: while the complicated structure of the internal magnetic field imposes a complication at first glance, the additional degree(s) of freedom yield extra possibilities for (spin-)wave manipulation. In particular, the interplay between external field, anisotropic lattice and possibly asymmetric antidots allows for the tuning of metamaterial properties on any of the respective hierarchies.

While the spin-wave filter discussed in section 4.4 is an example rather aiming at applications, the tunable mode splitting presented in figure 3.27 is a more fundamental example of physical effects in magnonic crystals. Hence, on the one hand, novel concepts like spin-wave metamaterials head towards new devices with yet unseen properties. On the other hand, they can be used to approach generic physical principles from a new point of view. In any case, experimental challenges in terms of spatial resolution and sensitivity need to be met in order to observe predicted effects like topological spin-wave insulation [HMM+11].

In summary, over the course of only one decade, mere magnonic ideas have evolved to feasible concepts and realizations of spin-wave manipulation. In particular, the young research field of magnonics displays the necessity for close interaction between theoretical and experimental works. The outlook on the possibilities of spin-wave manipulation with magnonic crystals given in section 3.6 already included the intrinsic anisotropy of the free-magnon dispersion. Herein lies a fundamental difference to electronics and photonics: a magnetic field applied externally or locally via an Oersted scheme can vastly change the sample or device characteristics. If, in the future, magnonic devices make use of this feature – as briefly exemplified in chapter 4 – considerable technological progress in terms of processing and transport of information is possible.

# Bibliography

**ACFW$^+$10** U. Atxitia, O. Chubykalo-Fesenko, J. Walowski, A. Mann, and M. Münzenberg, *Evidence for thermal mechanisms in laser-induced femtosecond spin dynamics*, Physical Review B **81** (2010), 174401. Cited on p. 10, 12, 58, 103.

**Ada88** J. D. Adam, *Analog signal processing with microwave magnetics*, Proceedings of the IEEE **76** (1988), 159. Cited on p. 26.

**Bab08** T. Baba, *Slow light in photonic crystals*, Nature Photonics **2** (2008), 465. Cited on p. 37.

**BH05** J. A. C. Bland and B. Heinrich (eds.), *Ultrathin Magnetic Structures*, Springer Berlin / Heidelberg, 2005. Cited on p. 2.

**BMC85** J. Blackman, T. Morgan, and J. F. Cooke, *Prediction of high-energy spin-wave excitation in iron*, Physical Review Letters **55** (1985), 2814. Cited on p. 41.

**BMDB96** E. Beaurepaire, J.-C. Merle, A. Daunois, and J.-Y. Bigot, *Ultrafast spin dynamics in ferromagnetic nickel*, Physical Review Letters **76** (1996), 4250. Cited on p. 12, 104.

**BOT$^+$09** D. R. Birt, B. O'Gorman, M. Tsoi, X. Li, V. E. Demidov, and S. O. Demokritov, *Diffraction of spin waves from a submicrometer-size defect in a microwaveguide*, Applied Physics Letters **95** (2009), 122510. Cited on p. 6, 52.

**BWM$^+$06** A. Barman, S. Wang, J. D. Maas, A. R. Hawkins, S. Kwon, A. Liddle, J. Bokor, and H. Schmidt, *Magneto-optical observation of picosecond dynamics of single nanomagnets*, Nano Letters **6** (2006), 2939. Cited on p. 78.

**CBF$^+$98** C. Chappert, H. Bernas, J. Ferré, V. Kottler, J.-P. Jamet, Y. Chen, E. Cambril, T. Devolder, F. Rousseaux, V. Mathet, and H. Launois, *Planar patterned magnetic media obtained by ion irradiation*, Science **280** (1998), 1919. Cited on p. 51, 52.

**CCG$^+$12** F. Ciubotaru, A. V. Chumak, N. Y. Grigoryeva, A. A. Serga, and B. Hillebrands, *Magnonic band gap design by the edge modulation of micro-sized waveguides*, Journal of Physics D: Applied Physics **45** (2012), 255002.

Cited on p. 6, 75.

**CLD80** J. F. Cooke, J. Lynn, and H. Davis, *Calculations of the dynamic susceptibility of nickel and iron*, Physical Review B **21** (1980), 4118. Cited on p. 41.

**CMM04** A. T. Costa, R. B. Muniz, and D. L. Mills, *Theory of spin waves in ultrathin ferromagnetic films: The case of Co on Cu(100)*, Physical Review B **69** (2004), 064413. Cited on p. 41, 58, 59.

**CNS$^+$09** A. V. Chumak, T. Neumann, A. A. Serga, B. Hillebrands, and M. P. Kostylev, *A current-controlled, dynamic magnonic crystal*, Journal of Physics D: Applied Physics **42** (2009), 205005. Cited on p. 51.

**Com07** FEI Company, *xT Nova NanoLab User's Manual*, 2007. Cited on p. 113, 114.

**CPS$^+$09** A. V. Chumak, P. Pirro, A. A. Serga, M. P. Kostylev, R. L. Stamps, H. Schultheiss, K. Vogt, S. J. Hermsdoerfer, B. Laegel, P. A. Beck, and B. Hillebrands, *Spin-wave propagation in a microstructured magnonic crystal*, Applied Physics Letters **95** (2009), 262508. Cited on p. 69, 75.

**CSW$^+$09** A. V. Chumak, A. A. Serga, S. Wolff, B. Hillebrands, and M. P. Kostylev, *Design and optimization of one-dimensional ferrite-film based magnonic crystals*, Journal of Applied Physics **105** (2009), 083906. Cited on p. 69.

**DDB$^+$08** V. E. Demidov, O. Dzyapko, M. Buchmeier, T. Stockhoff, G. Schmitz, G. A. Melkov, and S. O. Demokritov, *Magnon kinetics and Bose-Einstein condensation studied in phase space*, Physical Review Letters **101** (2008), 257201. Cited on p. 60.

**DDB$^+$09** V. E. Demidov, S. O. Demokritov, D. R. Birt, B. O'Gorman, M. Tsoi, and X. Li, *Radiation of spin waves from the open end of a microscopic magnetic-film waveguide*, Physical Review B **80** (2009), 14429. Cited on p. 26, 72.

**DDD$^+$06** S. O. Demokritov, V. E. Demidov, O. Dzyapko, G. A. Melkov, A. A. Serga, B. Hillebrands, and A. N. Slavin, *Bose-Einstein condensation of quasi-equilibrium magnons at room temperature under pumping*, Nature **443** (2006), 430. Cited on p. 55, 60.

**DDD$^+$08** V. E. Demidov, O. Dzyapko, S. O. Demokritov, G. A. Melkov, and A. N. Slavin, *Observation of spontaneous coherence in Bose-Einstein condensate of magnons*, Physical Review Letters **100** (2008), 47204. Cited on p. 10, 55.

**DE61** R. W. Damon and J. R. Eshbach, *Magnetostatic modes of a ferromagnet slab*, Journal of Physics and Chemistry of Solids **19** (1961), 308. Cited on p. 3, 39, 76, 79, 102.

**DEP$^+$06** M. Djordjevic, G. Eilers, A. Parge, M. Münzenberg, and J. S. Moodera, *Intrinsic and nonlocal Gilbert damping parameter in all optical pump-probe experiments*, Journal of Applied Physics **99** (2006), 08F308. Cited on p. 12, 56, 60, 103, 104.

**DJD+09** V. E. Demidov, J. Jersch, S. O. Demokritov, K. Rott, P. Krzysteczko, and G. Reiss, *Transformation of propagating spin-wave modes in microscopic waveguides with variable width*, Physical Review B **79** (2009), 54417. Cited on p. 26, 27.

**DLM+06** M. Djordjevic, M. Lüttich, P. Moschkau, P. Guderian, T. Kampfrath, R. G. Ulbrich, M. Münzenberg, W. Felsch, and J. S. Moodera, *Comprehensive view on ultrafast dynamics of ferromagnetic films*, physica status solidi (c) **3** (2006), 134. Cited on p. 63.

**DM07** M. Djordjevic and M. Münzenberg, *Connecting the timescales in picosecond remagnetization experiments*, Physical Review B **75** (2007), 12404. Cited on p. 10, 12, 14, 19, 41, 57, 58, 59, 80, 101, 104.

**DP99** M. J. Donahue and D. G. Porter, *OOMMF User's Guide*, 1999. Cited on p. 48.

**DSA+04** S. O. Demokritov, A. A. Serga, A. André, V. E. Demidov, M. P. Kostylev, B. Hillebrands, and A. N. Slavin, *Tunneling of dipolar spin waves through a region of inhomogeneous magnetic field*, Physical Review Letters **93** (2004), 47201. Cited on p. 9.

**EAT+05** M. Etzkorn, P. S. Anil Kumar, W. Tang, Y. Zhang, and J. Kirschner, *High-wave-vector spin waves in ultrathin Co films on W(110)*, Physical Review B **72** (2005), 184420. Cited on p. 58.

**Ell54** R. J. Elliott, *Theory of the effect of spin-orbit coupling on magnetic resonance in some semiconductors*, Physical Review **96** (1954), 266. Cited on p. 59.

**ELM06** G. Eilers, M. Lüttich, and M. Münzenberg, *Giant nonlocal damping by spin-wave emission: Micromagnetic simulations*, Physical Review B **74** (2006), 054411. Cited on p. 58.

**EUM+09** G. Eilers, H. Ulrichs, M. Münzenberg, A. Thomas, K. Thiel, and M. Seibt, *Long-range order on the atomic scale induced at CoFeB/MgO interfaces*, Journal of Applied Physics **105** (2009), 073701. Cited on p. 103.

**Far98** M. Farle, *Ferromagnetic resonance of ultrathin metallic layers*, Reports on Progress in Physics **61** (1998), 755. Cited on p. 11.

**FFBF07** T. Fischbacher, M. Franchin, G. Bordignon, and H. Fangohr, *A systematic approach to multiphysics extensions of finite-element-based micromagnetic simulations: Nmag*, IEEE Transactions On Magnetics **43** (2007), 2896. Cited on p. 48.

**FLL+06** L. Feng, X.-P. Liu, M.-H. Lu, Y.-B. Chen, Y.-F. Chen, Y.-W. Mao, J. Zi, Y.-Y. Zhu, S.N. Zhu, and N.-B. Ming, *Acoustic backward-wave negative refractions in the second band of a sonic crystal*, Physical Review Letters **96** (2006), 014301. Cited on p. 32.

**GCXC05** A. Gentils, J. N. Chapman, G. Xiong, and R. P. Cowburn, *Variation of domain-wall structures and magnetization ripple spectra in permalloy films with controlled uniaxial anisotropy*, Journal of Applied Physics **98** (2005), 053905. Cited on p. 15, 16.

**Gla88** H. L. Glass, *Ferrite films for microwave and millimeter-wave devices*, Proceedings of the IEEE **76** (1988), 151. Cited on p. 26.

**GM96** A. G. Gurevich and G. A. Melkov, *Magnetization oscillations and waves*, CRC Press, 1996. Cited on p. 2.

**GMVG82** P. Grünberg, C. Mayr, W. Vach, and M. Grimsditch, *Determination of magnetic parameters by means of brillouinscattering. Examples: Fe, Ni,* $Ni_{0.8}Fe_{0.2}$, Journal of Magnetism and Magnetic Materials **28** (1982), 319. Cited on p. 13.

**GNZ$^+$03** Y. V. Gulyaev, S. A. Nikitov, L. V. Zhivotovskii, A. A. Klimov, P. Tailhades, L. Presmanes, C. Bonningue, C. S. Tsai, S. L. Vysotskii, and Y. A. Filimonov, *Ferromagnetic films with magnon bandgap periodic structures: Magnon crystals*, Journal of Experimental and Theoretical Physics Letters **77** (2003), 567. Cited on p. 53.

**GTM$^+$10** G. Gubbiotti, S. Tacchi, M. Madami, G. Carlotti, A. O. Adeyeye, and M. P. Kostylev, *Brillouin light scattering studies of planar metallic magnonic crystals*, Journal of Physics D: Applied Physics **43** (2010), 264003. Cited on p. 68.

**GTM$^+$12** G. Gubbiotti, S. Tacchi, M. Madami, G. Carlotti, S. Jain, A. O. Adeyeye, and M. P. Kostylev, *Collective spin waves in a bicomponent two-dimensional magnonic crystal*, Applied Physics Letters **100** (2012), 162407. Cited on p. 75.

**HC05** X. Hu and C. Chan, *Refraction of water waves by periodic cylinder arrays*, Physical Review Letters **95** (2005), 154501. Cited on p. 4, 32.

**HE73** J. A. Hertz and D. M. Edwards, *Electron-magnon interactions in itinerant ferromagnetism. I. Formal theory*, Journal of Physics F: Metal Physics **3** (1973), 2174. Cited on p. 41, 59.

**HK51** C. Herring and C. Kittel, *On the theory of spin waves in ferromagnetic media*, Physical Review **81** (1951), 869. Cited on p. 103.

**HMM$^+$11** D. Hsieh, F. Mahmood, J. W. McIver, D. R. Gardner, Y. S. Lee, and N. Gedik, *Selective probing of photoinduced charge and spin dynamics in the bulk and surface of a topological insulator*, Physical Review Letters **107** (2011), 077401. Cited on p. 81.

**HP95** M. J. Hurben and C. E. Patton, *Theory of magnetostatic waves for in-plane magnetized isotropic films*, Journal of Magnetism and Magnetic Materials **139** (1995), 263. Cited on p. 43, 76, 108.

**HPH+10** J. Hamrle, J. Pištora, B. Hillebrands, B. Lenk, and M. Münzenberg, *Analytical expression of the magneto-optical Kerr effect and Brillouin light scattering intensity arising from dynamic magnetization*, Journal of Physics D: Applied Physics **43** (2010), 325004. Cited on p. 14, 58.

**Hsu11** J-C. Hsu, *Local resonances-induced low-frequency band gaps in two-dimensional phononic crystal slabs with periodic stepped resonators*, Journal of Physics D: Applied Physics **44** (2011), 055401. Cited on p. 4, 5.

**Hun07** S. Hunklinger, *Festkörperphysik*, Oldenbourg Verlag, 2007. Cited on p. 34, 35.

**HWK04** R. Hertel, W. Wulfhekel, and J. Kirschner, *Domain-wall induced phase shifts in spin waves*, Physical Review Letters **93** (2004), 257202. Cited on p. 29.

**Ish88** W. S. Ishak, *Magnetostatic wave technology: a review*, Proceedings of the IEEE **76** (1988), 171. Cited on p. 26.

**JDF+10** J. Jersch, V. E. Demidov, H. Fuchs, K. Rott, P. Krzysteczko, J. Münchenberger, G. Reiss, and S. O. Demokritov, *Mapping of localized spin-wave excitations by near-field Brillouin light scattering*, Applied Physics Letters **97** (2010), 152502. Cited on p. 56.

**JDM+99** J. Jorzick, S. O. Demokritov, C. Mathieu, B. Hillebrands, B. Bartenlian, C. Chappert, F. Rousseaux, and A. N. Slavin, *Brillouin light scattering from quantized spin waves in micron-size magnetic wires*, Physical Review B **60** (1999), 15194. Cited on p. 10.

**JJWM08** J. D. Joannopoulos, S. G. Johnson, J. N. Winn, and R. D. Meade, *Photonic crystals*, 2nd ed., Princeton University Press, 2008. Cited on p. 5, 36, 37.

**JNF+99** G. Ju, A. V. Nurmikko, R. F. C. Farrow, R. F. Marks, M. J. Carey, and B. A. Gurney, *Ultrafast time resolved photoinduced magnetization rotation in a ferromagnetic/antiferromagnetic exchange coupled system*, Physical Review Letters **82** (1999), 3705. Cited on p. 60.

**JVN+98** G. Ju, A. Vertikov, A. V. Nurmikko, C. Canady, G. Xiao, R. F. C. Farrow, and A. Cebollada, *Ultrafast nonequilibrium spin dynamics in a ferromagnetic thin film*, Physical Review B **57** (1998), R700. Cited on p. 12, 60.

**Kü00** J. Kübler, *Theory of itinerant magnetism*, Oxford Science Publication, Oxford, 2000. Cited on p. 34, 35.

**KBKK09** T. Kampfrath, D. M. Beggs, T. F. Krauss, and L. Kuipers, *Complete response characterization of ultrafast linear photonic devices*, Optics Letters **34** (2009), 3418. Cited on p. 37.

**KBW+09** T. Kampfrath, D. M. Beggs, T. P. White, M. Burresi, D. van Oosten, T. F. Krauss, and L. Kuipers, *Ultrafast rerouting of light via slow modes in a nanophotonic directional coupler*, Applied Physics Letters **94** (2009), 241119. Cited on p. 37.

**KBW+10a** T. Kampfrath, D. M. Beggs, T. P. White, A. Melloni, T. F. Krauss, and L. Kuipers, *Ultrafast adiabatic manipulation of slow light in a photonic crystal*, Physical Review A **81** (2010), 043837. Cited on p. 80.

**KBW10b** A. Khitun, M. Bao, and K. L. Wang, *Magnonic logic circuits*, Journal of Physics D: Applied Physics **43** (2010), 264005. Cited on p. 26, 28, 31, 75, 80.

**KDG10** V. V. Kruglyak, S. O. Demokritov, and D. Grundler, *Magnonics*, Journal of Physics D: Applied Physics **43** (2010), 260301. Cited on p. 23, 75, 101.

**Ker77** J. Kerr, *On the rotation of the plane of polarization by reflection from the pole of a magnet*, The London, Edingburgh, and Dublin Philosophical Magazine and Journal of Science **3** (1877), 321. Cited on p. 3.

**KGM+08** M. H. Kryder, E. C. Gage, T. W. McDaniel, W. A. Challener, R. E. Rottmayer, and M. F. Erden, *Heat Assisted Magnetic Recording*, Proceedings of the IEEE **96** (2008), 1810. Cited on p. 75.

**KH50** C. Kittel and C. Herring, *Effect of exchange interaction on ferromagnetic microwave resonance absorption*, Physical Review **77** (1950), 725. Cited on p. 3.

**KH06** V. V. Kruglyak and R. J. Hicken, *Magnonics: Experiment to prove the concept*, Journal of Magnetism and Magnetic Materials **306** (2006), 191. Cited on p. 51, 60, 78.

**KHN+07** N. Kazantseva, D. Hinzke, U. Nowak, R. W. Chantrell, and O. Chubykalo-Fesenko, *Atomistic models of ultrafast reversal*, physica status solidi (b) **244** (2007), 4389. Cited on p. 58.

**Kim10** S.-K. Kim, *Micromagnetic computer simulations of spin waves in nanometre-scale patterned magnetic elements*, Journal of Physics D: Applied Physics **43** (2010), 264004. Cited on p. 47, 60, 69.

**KJRZ11** T. Kao, S. Jenkins, J. Ruostekoski, and N. Zheludev, *Coherent control of nanoscale light localization in metamaterial: Creating and positioning isolated subwavelength energy hot spots*, Physical Review Letters **106** (2011), 85501. Cited on p. 5.

**KKN+10** V. V. Kruglyak, P. S. Keatley, A. Neudert, R. J. Hicken, J. R. Childress, and J. A. Katine, *Imaging collective magnonic modes in 2D arrays of magnetic nanoelements*, Physical Review Letters **104** (2010), 027201. Cited on p. 68.

**KKR10** A. Kirilyuk, A. Kimel, and T. Rasing, *Ultrafast optical manipulation of* *magnetic order*, Reviews of Modern Physics **82** (2010), 2731. Cited on p. 55.

**KLH09** S.-K. Kim, K.-S. Lee, and D.-S. Han, *A gigahertz-range spin-wave filter composed of width-modulated nanostrip magnonic-crystal waveguides*, Applied Physics Letters **95** (2009), 082507. Cited on p. 41.

**KMD$^+$10** B. Koopmans, G. Malinowski, F. Dalla Longa, D. Steiauf, M. Fähnle, T. Roth, M. Cinchetti, and M. Aeschlimann, *Explaining the paradoxical diversity of ultrafast laser-induced demagnetization*, Nature Materials **9** (2010), 259. Cited on p. 12, 58.

**KNB$^+$07** A. Khitun, D. E. Nikonov, M. Bao, K. Galatsis, and K. L. Wang, *Feasibility study of logic circuits with a spin wave bus*, Nanotechnology **18** (2007), 465202. Cited on p. 28, 29.

**KP08** M. Krawczyk and H. Puszkarski, *Plane-wave theory of three-dimensional magnonic crystals*, Physical Review B **77** (2008), 54413. Cited on p. 42, 47, 76, 108, 109.

**KPR$^+$05** S. Kaka, M. Pufall, W. H. Rippard, T. J. Silva, S. E. Russek, and J. A. Katine, *Mutual phase-locking of microwave spin torque nano-oscillators*, Nature **437** (2005), 389. Cited on p. 9, 17.

**Kra07** T.F. Krauss, *Slow light in photonic crystal waveguides*, Journal of Physics D: Applied Physics **40** (2007), 2666–2670. Cited on p. 5, 38, 71.

**Kra08** T. F. Krauss, *Why do we need slow light?*, Nature Photonics **2** (2008), 448. Cited on p. 37.

**KRLdJ05** B. Koopmans, J. Ruigrok, F. Longa, and W. J. M. de Jonge, *Unifying ultrafast magnetization dynamics*, Physical Review Letters **95** (2005), 267207. Cited on p. 59.

**KS86** B. A. Kalinikos and A. N. Slavin, *Theory of dipole-exchange spin wave spectrum for ferromagnetic films with mixed exchange boundary conditions*, Journal of Physics C: Solid State Physics **19** (1986), 7013. Cited on p. 3, 11, 39, 40, 43, 102, 107, 108.

**KSS$^+$05** M. P. Kostylev, A. A. Serga, T. Schneider, B. Leven, and B. Hillebrands, *Spin-wave logical gates*, Applied Physics Letters **87** (2005), 153501. Cited on p. 75.

**KW05** A. Khitun and K. L. Wang, *Nano scale computational architectures with spin wave bus*, Superlattices and Microstructures **38** (2005), 184. Cited on p. 28, 29.

**LAPM12** B. Lenk, N. Abeling, J. Panke, and M. Münzenberg, *Spin-wave modes and band structure of rectangular CoFeB antidot lattices*, Journal of Applied Physics **112** (2012), 083921. Cited on p. 6, 117.

**LEHM10** B. Lenk, G. Eilers, J. Hamrle, and M. Münzenberg, *Spin-wave population* *in nickel after femtosecond laser pulse excitation*, Physical Review B **82** (2010), 134443. Cited on p. 3, 13, 39, 59, 60, 78, 79, 97, 102, 105, 117.

**LGU+13** B. Lenk, F. Garbs, H. Ulrichs, N. Abeling, and M. Münzenberg, *Photo-Magnonics*, Magnonics (S. O. Demokritov and A. N. Slavin, eds.), Topics in Applied Physics, vol. 125, Springer Berlin / Heidelberg, 2013, pp. 71–81. Cited on p. 117.

**LHK09** K.-S. Lee, D.-S. Han, and S.-K. Kim, *Physical origin and generic control of magnonic band gaps of dipole-exchange spin waves in width-modulated nanostrip waveguides*, Physical Review Letters **102** (2009), 127202. Cited on p. 6, 68, 69, 75.

**LMC+09** C. Liu, C. K. A. Mewes, M. Chshiev, T. Mewes, and W. H. Butler, *Origin of low Gilbert damping in half metals*, Applied Physics Letters **95** (2009), 022509. Cited on p. 31.

**LRK+10** K.-D. Lee, K.-S. Ryu, J.-W. Kim, H.-S. Song, J.-W. Jeong, and S.-C. Shin, *Dephasing in photoinduced large-angle spin precession of confined ferromagnetic structures*, Physical Review B **82** (2010), 140401(R). Cited on p. 60.

**LSK+07** Y. Liu, L. R. Shelford, V. V. Kruglyak, R. J. Hicken, Y. Sakuraba, M. Oogane, Y. Ando, and T. Miyazaki, *Ultrafast optical modification of magnetic anisotropy and stimulated precession in an epitaxial* $Co_2MnAl$ *thin film*, Journal of Applied Physics, vol. 101, 2007, p. 09C106. Cited on p. 12, 20.

**LSKH10** Y. Liu, L. R. Shelford, V. V. Kruglyak, and R. J. Hicken, *Optically induced magnetization dynamics and variation of damping parameter in epitaxial* $Co_2MnSi$ *Heusler alloy films*, Physical Review B **81** (2010), 094402. Cited on p. 60.

**LUGM11** B. Lenk, H. Ulrichs, F. Garbs, and M. Münzenberg, *The building blocks of magnonics*, Physics Reports **507** (2011), 107. Cited on p. 5, 75, 76, 79, 101, 108, 109, 110, 117.

**MÏ0** M. Münzenberg, *Magnetization dynamics: Ferromagnets stirred up*, Nature Materials **9** (2010), 184. Cited on p. 58.

**MANG09** S. Martens, O. Albrecht, K. Nielsch, and D. Görlitz, *Local modes and two magnon scattering in ordered permalloy antidot arrays*, Journal of Applied Physics **105** (2009), 07C113. Cited on p. 51, 52.

**MEW+08** G. M. Müller, G. Eilers, Z. Wang, M. Scherff, R. Ji, K. Nielsch, C. A. Ross, and M. Münzenberg, *Magnetization dynamics in optically excited nanostructured nickel films*, New Journal of Physics **10** (2008), 123004. Cited on p. 63, 64.

**MMMG08** G. M. Müller, M. Münzenberg, G.-X. Miao, and A. Gupta, *Activation of additional energy dissipation processes in the magnetization dynamics of* *epitaxial chromium dioxide films*, Physical Review B **77** (2008), 020412(R). Cited on p. 60.

**MRET05** F. B. Mancoff, N. D. Rizzo, B. N. Engel, and S. Tehrani, *Phase-locking in double-point-contact spin-transfer devices*, Nature **437** (2005), 393. Cited on p. 9, 17.

**MTM+12** S. Mansfeld, J. Topp, K. Martens, J. N. Toedt, W. Hansen, D. Heitmann, and S. Mendach, *Spin wave diffraction and perfect imaging of a grating*, Physical Review Letters **108** (2012), 047204. Cited on p. 76.

**MWD+09** G. M. Müller, J. Walowski, M. Djordjevic, G.-X. Miao, A. Gupta, A. V. Ramos, K. Gehrke, V. Moshnyaga, K. Samwer, J. Schmalhorst, A. Thomas, A. Hütten, G. Reiss, J. S. Moodera, and M. Münzenberg, *Spin polarization in half-metals probed by femtosecond spin excitation*, Nature Materials **8** (2009), 56. Cited on p. 31.

**NBD+11** S. Neusser, H. Bauer, G. Duerr, R. Huber, S. Mamica, G. Woltersdorf, M. Krawczyk, C. Back, and D. Grundler, *Tunable metamaterial response of a $Ni_{80}Fe_{20}$ antidot lattice for spin waves*, Physical Review B **84** (2011), 184411. Cited on p. 80.

**NBG08** S. Neusser, B. Botters, and D. Grundler, *Localization, confinement, and field-controlled propagation of spin waves in $Ni_{80}Fe_{20}$ antidot lattices*, Physical Review B **78** (2008), 54406. Cited on p. 10, 61, 62, 70.

**NDB+10** S. Neusser, G. Duerr, H. Bauer, S. Tacchi, M. Madami, G. Woltersdorf, G. Gubbiotti, C. Back, and D. Grundler, *Anisotropic propagation and damping of spin waves in a nanopatterned antidot lattice*, Physical Review Letters **105** (2010), 067208. Cited on p. 54, 61, 101.

**NG09** S. Neusser and D. Grundler, *Magnonics: Spin waves on the nanoscale*, Advanced Materials **21** (2009), 2927. Cited on p. 51.

**NH92** A. Neubrand and P. Hess, *Laser generation and detection of surface acoustic waves: Elastic properties of surface layers*, Journal of Applied Physics **71** (1992), 227–238. Cited on p. 14.

**NMW+05** U. Nowak, O. Mryasov, R. Wieser, K. Y. Guslienko, and R. W. Chantrell, *Spin dynamics of magnetic nanoparticles: Beyond Brown's theory*, Physical Review B **72** (2005), 172410. Cited on p. 58.

**NTT01** S. A. Nikitov, P. Tailhades, and C. S. Tsai, *Spin waves in periodic magnetic structures - magnonic crystals*, Journal of Magnetism and Magnetic Materials **236** (2001), 320. Cited on p. 6, 75.

**OnRKK+09** C. Ordóñez Romero, B. A. Kalinikos, P. Krivosik, W. Tong, P. Kabos, and C. E. Patton, *Three-magnon splitting and confluence processes for spin-wave excitations in yttrium iron garnet films: Wave vector selective Brillouin light scattering measurements and analysis*, Physical Review B **79** (2009), 144428. Cited on p. 54.

**PGG06** J. Podbielski, F. Giesen, and D. Grundler, *Spin-wave interference in microscopic rings*, Physical Review Letters **96** (2006), 167207. Cited on p. 53, 101.

**PMMS88** D. Paul, P. W. Mitchell, H. A. Mook, and U. Steigenberger, *Observation of itinerant-electron effects on the magnetic excitations of iron*, Physical Review B **38** (1988), 580. Cited on p. 41, 58.

**Pru12** *Doctoral Degree Regulations (RerNat-O)*, Georg-August University School of Science (GAUSS), 2012. Cited on p. 117.

**PYC$^+$05** M. J. Pechan, C. Yu, R. L. Compton, J. P. Park, and P. A. Crowell, *Direct measurement of spatially localized ferromagnetic-resonance modes in an antidot lattice*, Journal of Applied Physics **97** (2005), no. 10, 10J903. Cited on p. 10, 53, 55, 61, 62, 110.

**RKBS08** A. A. Rzhevsky, B. B. Krichevtsov, D. E. Bürgler, and C. M. Schneider, *Interface and bulk magnetization dynamics in biaxial Fe/Cr structures induced by ultrashort optical pulses*, Journal of Applied Physics **104** (2008), 083918. Cited on p. 60.

**Rod88** G. P. Rodrigue, *A generation of microwave ferrite devices*, Proceedings of the IEEE **76** (1988), 121. Cited on p. 26.

**RRRV$^+$08** G. Rodríguez-Rodríguez, H. Rubio, M. Vélez, A. Pérez-Junquera, J. Anguita, J. Martín, and J. Alameda, *Closure magnetization configuration around a single hole in a magnetic film*, Physical Review B **78** (2008), 174417. Cited on p. 51.

**RSdLK07** K. Rivkin, W. Saslow, L. E. de Long, and J. B. Ketterson, *Dynamic magnetic response of infinite arrays of ferromagnetic particles*, Physical Review B **75** (2007), 174408. Cited on p. 48.

**SAC76** C. G. Sykes, J. D. Adam, and J. H. Collins, *Magnetostatic wave propagation in a periodic structure*, Applied Physics Letters **29** (1976), 388. Cited on p. 6, 26.

**Sch88** E. F. Schloemann, *Circulators for microwave and millimeter-wave integrated circuits*, Proceedings of the IEEE **76** (1988), 188. Cited on p. 26.

**SCH10** A. A. Serga, A. V. Chumak, and B. Hillebrands, *YIG magnonics*, Journal of Physics D: Applied Physics **43** (2010), 264002. Cited on p. 2, 51.

**SDJ$^+$07** S. Schnittger, S. Dreyer, C. Jooss, S. Sievers, and U. Siegner, *Magnetostatic interactions in patterned CoPt films embedded in a permalloy matrix*, Applied Physics Letters **90** (2007), 042506. Cited on p. 51, 52.

**Sem09** *International Semiconductor Roadmap*, 2009. Cited on p. 25.

**SF09** D. Steiauf and M. Fähnle, *Elliott-Yafet mechanism and the discussion of femtosecond magnetization dynamics*, Physical Review B **79** (2009), 140401(R). Cited on p. 59.

**SIF10** D. Steiauf, C. Illg, and M. Fähnle, *Demagnetization on the fs time-scale by the Elliott-Yafet mechanism*, Journal of Physics: Conference Series **200** (2010), 042024. Cited on p. 59.

**SJV$^+$10** C. W. Sandweg, M. B. Jungfleisch, V. I. Vasyuchka, A. A. Serga, P. Clausen, H. Schultheiss, B. Hillebrands, A. Kreisel, and P. Kopietz, *Wide-range wavevector selectivity of magnon gases in Brillouin light scattering spectroscopy*, The Review of Scientific Instruments **81** (2010), 73902. Cited on p. 54, 101.

**SLCR99** T. J. Silva, C. S. Lee, T. M. Crawford, and C. T. Rogers, *Inductive measurement of ultrafast magnetization dynamics in thin-film Permalloy*, Journal of Applied Physics **85** (1999), 7849. Cited on p. 53, 54.

**SPD$^+$10** A. B. Schmidt, M. Pickel, M. Donath, P. Buczek, A. Ernst, V. P. Zhukov, P. M. Echenique, L. M. Sandratskii, E. V. Chulkov, and M. Weinelt, *Ultrafast magnon generation in an Fe film on Cu(100)*, Physical Review Letters **105** (2010), 197401. Cited on p. 59.

**SPW04** D. R. Smith, J. B. Pendry, and M. C. K. Wiltshire, *Metamaterials and negative refractive index*, Science **305** (2004), 788. Cited on p. 32.

**SSC$^+$10** T. Schneider, A. A. Serga, A. V. Chumak, C. W. Sandweg, S. Trudel, S. Wolff, M. P. Kostylev, V. S. Tiberkevich, A. N. Slavin, and B. Hillebrands, *Nondiffractive subwavelength wave beams in a medium with externally controlled anisotropy*, Physical Review Letters **104** (2010), 197203. Cited on p. 72.

**SSHK08** T. Schneider, A. A. Serga, B. Hillebrands, and M. P. Kostylev, *Spin-wave ferromagnetic film combiner as a NOT logic gate*, Journal of Nanoelectronics and Optoelectronics **3** (2008), 69. Cited on p. 2, 30.

**SSL$^+$08** T. Schneider, A. A. Serga, B. Leven, B. Hillebrands, R. L. Stamps, and M. P. Kostylev, *Realization of spin-wave logic gates*, Applied Physics Letters **92** (2008), 022505. Cited on p. 9, 29, 30, 75, 80.

**SSP$^+$10** B. C. Stipe, T. C. Strand, C. C. Poon, H. Balamane, T. D. Boone, J. A. Katine, J.-L. Li, V. Rawat, H. Nemoto, A. Hirotsune, O. Hellwig, R. Ruiz, E. Dobisz, D. S. Kercher, N. Robertson, T. R. Albrecht, and B. D. Terris, *Magnetic recording at 1.5 Pb $m^{-2}$ using an integrated plasmonic antenna*, Nature Photonics **4** (2010), 484. Cited on p. 75.

**ST58** M. H. Seavey and P. E. Tannenwald, *Direct observation of spin-wave resonance*, Physical Review Letters **1** (1958), 168. Cited on p. 13, 16.

**ST06** A. N. Slavin and V. S. Tiberkevich, *Theory of mutual phase locking of spin-torque nanosized oscillators*, Physical Review B **74** (2006), 104401. Cited on p. 9, 17.

**Sup74** P. Suppes, *Aristotle's concept of matter and its relation to modern concepts of matter*, Synthese **28** (1974), 27. Cited on p. 4.

**TMG⁺10** S. Tacchi, M. Madami, G. Gubbiotti, G. Carlotti, A. O. Adeyeye, S. Neusser, B. Botters, and D. Grundler, *Angular dependence of magnetic normal modes in NiFe antidot lattices with different lattice symmetry*, IEEE Transactions On Magnetics **46** (2010), 1440. Cited on p. 67.

**TMM⁺11** S. Tacchi, F. Montoncello, M. Madami, G. Gubbiotti, G. Carlotti, L. Giovannini, R. Zivieri, F. Nizzoli, S. Jain, A. O. Adeyeye, and N. Singh, *Band diagram of spin waves in a two-dimensional magnonic crystal*, Physical Review Letters **107** (2011), 127204. Cited on p. 101.

**TPHG08** J. Topp, J. Podbielski, D. Heitmann, and D. Grundler, *Internal spin-wave confinement in magnetic nanowires due to zig-zag shaped magnetization*, Physical Review B **78** (2008), 024431. Cited on p. 69.

**ULM10** H. Ulrichs, B. Lenk, and M. Münzenberg, *Magnonic spin-wave modes in CoFeB antidot lattices*, Applied Physics Letters **97** (2010), 092506. Cited on p. 6, 9, 51, 75, 78, 79, 80, 105, 110.

**Ulr10** H. Ulrichs, *Magnonische Metamaterialien aus CoFeB*, Diploma thesis, Georg-August-University of Göttingen, 2010. Cited on p. 48.

**VAG⁺05** M. Vomir, L. Andrade, L. Guidoni, E. Beaurepaire, and J.-Y. Bigot, *Real space trajectory of the ultrafast magnetization dynamics in ferromagnetic metals*, Physical Review Letters **94** (2005), 237601. Cited on p. 60.

**VB10** V. Vlaminck and M. Bailleul, *Spin-wave transduction at the submicrometer scale: Experiment and modeling*, Physical Review B **81** (2010), 014425. Cited on p. 51.

**VDDRP96** J. Vasseur, L. Dobrzynski, B. Djafari-Rouhani, and H. Puszkarski, *Magnon band structure of periodic composites*, Physical Review B **54** (1996), 1043. Cited on p. 6, 42, 44, 47, 76, 108.

**VEA⁺04** R. Vollmer, M. Etzkorn, P. S. Anil Kumar, H. Ibach, and J. Kirschner, *Spin-wave excitation in ultrathin Co and Fe films on Cu(001) by spin-polarized electron energy loss spectroscopy (invited)*, Journal of Applied Physics **95** (2004), 7435. Cited on p. 58.

**Ves68** V. G. Veselago, *The electrodynamics of substances with simultaneously negative values of $\epsilon$ and $\mu$*, Soviet Physics Uspekhi **10** (1968), 509. Cited on p. 31.

**vKJK⁺02** M. van Kampen, C. Jozsa, J. T. Kohlhepp, P. LeClair, L. Lagae, W. J. M. de Jonge, and B. Koopmans, *All-optical probe of coherent spin waves*, Physical Review Letters **88** (2002), 227201. Cited on p. 3, 12, 60.

**VSH⁺09** K. Vogt, H. Schultheiss, S. J. Hermsdoerfer, P. Pirro, A. A. Serga, and B. Hillebrands, *All-optical detection of phase fronts of propagating spin waves in a $Ni_{81}Fe_{19}$ microstripe*, Applied Physics Letters **95** (2009), 182508. Cited on p. 54.

**WAS06** C. C. Wang, A. O. Adeyeye, and N. Singh, *Magnetic antidot nanostructures: Effect of lattice geometry*, Nanotechnology **17** (2006), 1629. Cited on p. 65.

**WDL⁺08** J. Walowski, M. Djordjevic, B. Lenk, C. Hamann, J. McCord, and M. Münzenberg, *Intrinsic and non-local Gilbert damping in polycrystalline nickel studied by Ti:sapphire laser fs spectroscopy*, Journal of Physics D: Applied Physics **41** (2008), 164016. Cited on p. 56, 78.

**WKS⁺04** M. Wu, M. A. Kraemer, M. M. Scott, C. E. Patton, and B. A. Kalinikos, *Spatial evolution of multipeaked microwave magnetic envelope solitons in yttrium iron garnet thin films*, Physical Review B **70** (2004), 54402. Cited on p. 53.

**WMD⁺08** J. Walowski, G. M. Müller, M. Djordjevic, M. Münzenberg, M. Kläui, C. Vaz, and J. A. C. Bland, *Energy equilibration processes of electrons, magnons, and phonons at the femtosecond time scale*, Physical Review Letters **101** (2008), 237401. Cited on p. 59.

**WTK⁺98** E. F. Wassermann, M. Thielen, S. Kirsch, A. Pollmann, H. Weinforth, and A. Carl, *Fabrication of large scale periodic magnetic nanostructures*, Journal of Applied Physics **83** (1998), 1753. Cited on p. 6.

**WZL⁺10** Z. K. Wang, V. L. Zhang, H. S. Lim, S. C. Ng, M. H. Kuok, S. Jain, and A. O. Adeyeye, *Nanostructured magnonic crystals with size-tunable bandgaps*, ACS nano **4** (2010), 643. Cited on p. 46.

**YTO⁺09** J. Yang, Y. F. Tang, C. F. Ouyang, X. H. Liu, X. H. Hu, and J. Zi, *Observation of the focusing of liquid surface waves*, Applied Physics Letters **95** (2009), 094106. Cited on p. 4, 5.

Appendix A

# Supplemental material of PRB 82, 134443 (2010)

The supplemental material from reference [LEHM10] may also be accessed at `http://link.aps.org/supplemental/10.1103/PhysRevB.82.134443`.

## A.1 Time-resolved data

In the following, additional data are presented. Figure A.1 contains two data sets recorded on 100 nm of nickel. The applied field of 150 mT (right plot) is higher-than-critical for the thickness and thus, only the uniform precession (Kittel mode) is excited by the pump pulses. The selection of the magnetic eigen mode happens in the first few tens of picoseconds. More precisely, no classical synchronization over time of two modes is found, but a selective population from the initial state of disorder.

For $\mu_0 H_{\text{ext}} = 70\,\text{mT}$ (left plot) a beating of two modes can be observed. Here, the external field is lower-than-critical and no coupling takes place. Accordingly, the Fourier analysis presented in figure 2.4 of the manuscript yields two peaks separated by 2 GHz.

## A.2 Angle of the external field

For the experiments the external field was applied under angle of 30° with respect to the sample plane due to reasons discussed in the paper. A variation of this angle yields the FFT power spectra as presented in figure A.2 (nickel thickness $t = 150\,\text{nm}$). With increasing angle, the deviation from the Damon-Eshbach mode dispersion sets in earlier. However, in all data sets the excitation of the Kittel mode above the critical field is apparent, with no significant change of the critical field.

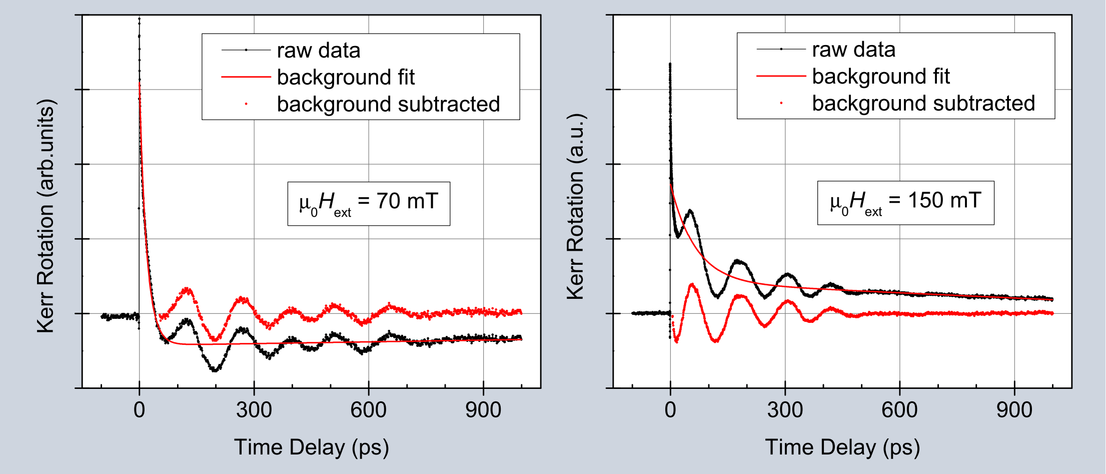

**Figure A.1 – Time-resolved pump-induced change of the Kerr rotation at $t = 100$ nm.** For $\mu_0 H_{\text{ext}} = 70$ mT and $\mu_0 H_{\text{ext}} = 150$ mT, respectively. The red solid lines are an exponential fit to the incoherent background and the subtracted data sets (red points) reveal the magnetic modes of precession. Below the critical field two modes are populated, whereas above the critical field only one mode of magnetic precession occurs, namely the Kittel mode.

## A.3 Hysteresis

For completeness, please find below the hysteresis curves recorded on various thicknesses of the wedge-shaped nickel sample (figure A.3(a)). The measurements were performed with the external field applied under an angle of 30° which was also used in the TRMOKE experiments. Added in figure A.3(b) and (c) is the respective analysis of the saturation field $H_{\text{sat}}$ and the coercivity $H_{\text{coerc}}$. The saturation field is given by the point, at which the Kerr rotation is equal for the two ramping directions of the external field (curvatures of the two branches are mostly slowly approaching, resulting in comparably high values). The coercive field is always smaller than 20 mT which excludes an influence on the effects discussed in the paper.

On the other hand, $H_{\text{sat}}$ shows a step-like behaviour similar to the one observed for the critical field above which the Kittel mode is excited (gray points in figure A.3(b)). It is highest for a thickness of 120 nm there taking a value of approximately 76 mT. Nevertheless, the critical field at which the Damon-Eshbach mode merges into the Kittel mode is well above – at field values around 115 mT.

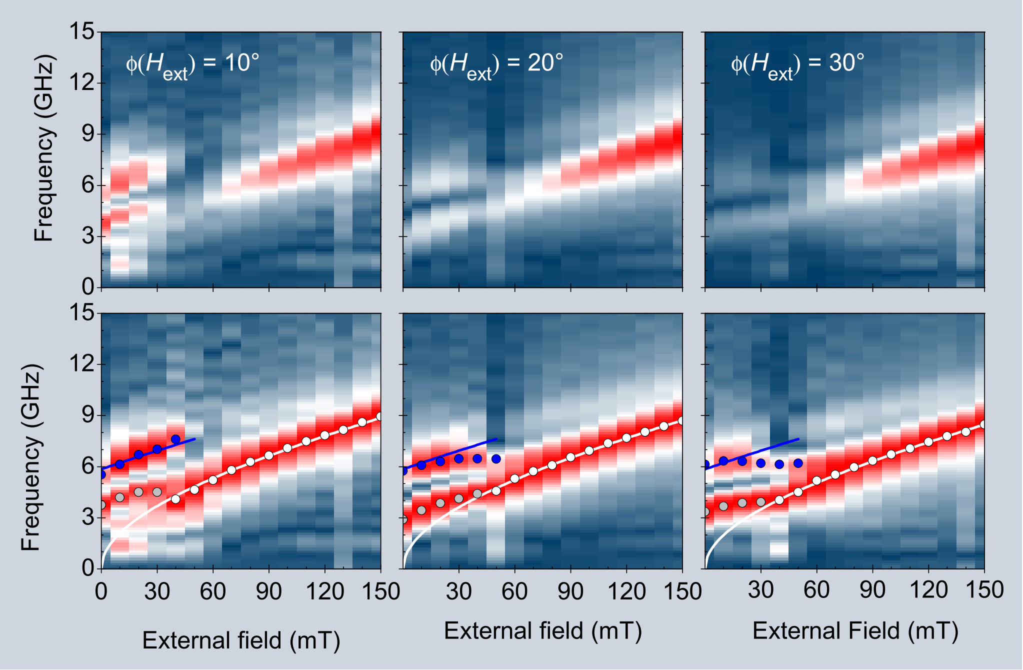

**Figure A.2 – Influence of the canting angle of the external field.** Nickel thickness was 150 nm.

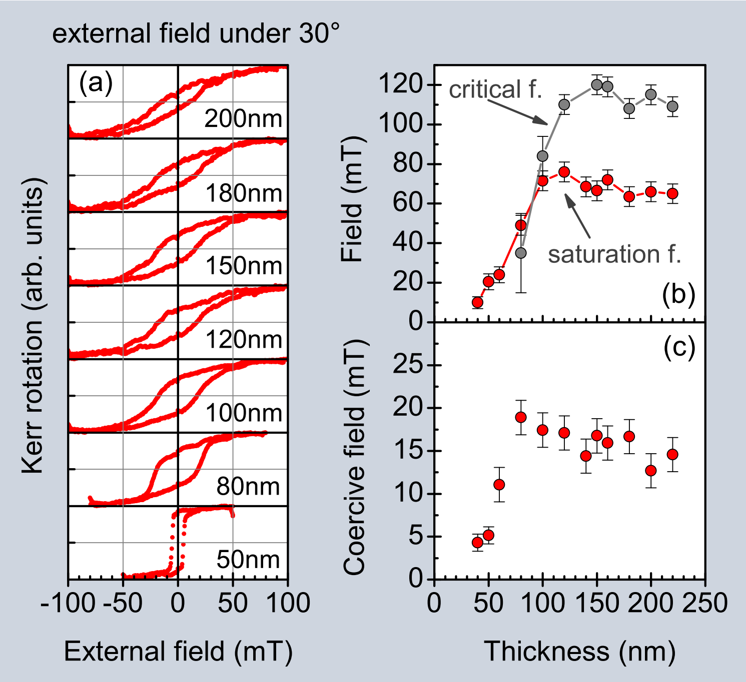

**Figure A.3 – Hysteresis.** Curves recorded on different thicknesses of the ferromagnetic nickel layer (a) and the respective analysis of the saturation field (b) as well as the coercive field (c). The gray points in (b) represent the critical field as described in the manuscript. Both physical quantities are well separated and should therefore be independent.

## Appendix B

# Photo-magnonics

B. Lenk, F. Garbs, H. Ulrichs, N. Abeling, and M. Münzenberg
in *Magnonics: From Fundamentals to Applications* (pp. 71–81)
S. O. Demokritov and A. N. Slavin (Editors)
Springer Berlin / Heidelberg, 2013
DOI: 10.1007/978-3-642-30247-3_6

**Abstract.** In the framework of magnonics all-optical femtosecond laser experiments are used to study spin waves and their relaxation paths. Magnonic crystal structures based on antidots allow the control over the spin-wave modes. In these two-dimensional magnetic metamaterials with periodicities in the wave-length range of dipolar spin waves the spin-wave bands and dispersion are modified. Hence, a specific selection of spin-wave modes excited by laser pulses is possible. Different to photonics, the modes depend strongly on the strength of the magneto-static potential at around each antidot site – the dipolar field. While this may lead to a mode localization, also for filling fractions around or below 10%, Bloch states are found in low damping ferromagnetic metals. In this chapter, an overview of these mechanisms is given and the connection to spin-wave band spectra calculated from an analytical model is established. Namely, the plane-wave method yields flattened bands as well as band gaps at the antidot lattice Brillouin zone boundary.

## B.1 Introduction

Being a quickly evolving research field, magnonics and magnonic materials have been investigated with different approaches [LUGM11, KDG10]. These can be in the time or frequency domain, as well as with very high spatial resolution down to nanometers or averaging over wider areas, then giving more general information on the system in question. For example, the spin-wave dispersion $\omega(k)$ can precisely be measured using a vector network analyzer (VNA) [PGG06, NDB$^+$10] or Brillouin light scattering (BLS) setup [TMM$^+$11, SJV$^+$10]. In such experiments, the selection of the excitation frequency or wave vector $k$, respectively, enables a detailed study of the magnetic mode spectrum in Fourier space.

In contrast, all-optical pump-probe techniques are neither $k$- nor frequency-selective. Instead, a broad continuum of spin-wave modes is populated on ultrafast time scales in the femto- to picosecond range by absorption of an intense laser pulse [DM07]. The heat-induced disorder can be modeled by high-$k$ spin-wave modes that subsequently relax into energetically lower-lying states. A population of respective spin-wave modes leads to a spatial distribution of energy by spin-wave propagation away from the spot of (optical) excitation [LEHM10]. The underlying processes for excitation, relaxation, and propagation span a large range of interaction energies (i.e. time scales). Connected transient dynamics have an effect on the dielectric tensor and thus can be optically investigated. Herein lies the large potential of (laser-) pulsed experiments: femto-, pico- and nanosecond characteristics can be resolved in a fast and non-destructive manner.

Concerning optically excited spin waves, these condensate-like modes are intrinsically dependent on the matrix material properties. However, the reverse process is also possible: In a magnonic structure, i.e. a spin-wave metamaterial, the material properties can be tailored to produce spin-wave modes whose characteristic properties are decoupled from the ferromagnetic matrix. In the present chapter of this book, we shall restrict the discussion to two-dimensional systems. First, in section B.1.1 the continuous thin film case will be briefly described, while section B.2 introduces all-optical experiments are. The final sections B.3 – B.5 are dedicated to structured media for which the manipulation of the spin-wave spectrum will be exemplified. Finally, an outlook on possible devices based on spin-wave computing is presented.

## B.1.1 Spin-wave modes in a thin ferromagnetic film

For the case of a continuous film of thickness $t$, the Landau-Lifshitz-Gilbert equation of motion can be solved analytically [DE61, KS86]. On sufficiently large length scales, the exchange interaction may be neglected. The resulting spin-wave modes are of dipolar character and have theoretically been studied by Damon and Eshbach (DE) in the 1960s. In the geometry of propagation perpendicular to the applied magnetic field (wave vector $k_{\mathrm{DE}} \perp H_{\mathrm{ext}}$) the dispersion takes the form [DE61]

$$\left(\frac{\omega_{\mathrm{DE}}}{\gamma\mu_0}\right)^2 = H_x\left(H_x + M_{\mathrm{S}} - \frac{2K_z}{\mu_0 M_{\mathrm{S}}}\right) + \frac{M_{\mathrm{S}}^2}{4}\left(1 - e^{-2|k_{\mathrm{DE}}|t}\right), \tag{B.1}$$

where $\omega_{\mathrm{DE}}$ is the spin-wave frequency, $M_{\mathrm{S}}$ is the material's saturation magnetization, $H_x$ is the in-plane component of the external field, and $K_z$ accounts for an effective out-of-plane anisotropy. Respective wavelengths $\lambda_{\mathrm{DE}} = 2\pi/k_{\mathrm{DE}}$ are in the micron range. On much smaller length scales, the exchange interaction has to be considered, while the dipolar interaction can then be neglected. The dispersion for exchange-dominated spin waves reads

$$\left(\frac{\omega_\perp}{\gamma\mu_0}\right)^2 = \left(H_x + \frac{2A}{M_\mathrm{S}}\,k_\perp^2\right)\left(H_x + M_\mathrm{S} - \frac{2K_z}{\mu_0 M_\mathrm{S}} + \frac{2A}{M_\mathrm{S}}\,k_\perp^2\right) , \tag{B.2}$$

where $A$ is the exchange constant. In equation (B.2), it has already been considered that respective spin-wave lengths are only relevant in the direction perpendicular to the film plane. Standing spin waves of the order $n$ can be excited where the wave vector is then quantized according to $k_\perp = n\pi/t$ – hence the naming perpendicular standing spin waves (PSSW). The geometric confinement of thin films with thickness in the nanometer range implies the possibility to independently study exchange and dipolar spin waves. In the lateral directions, the exchange interaction does not play a significant role, whereas in the direction perpendicular to the film plane it determines the spin waves potentially excited. From equations (B.1) and (B.2), another precessional mode can be deduced: An in-phase precession of all spins, i.e., the uniform mode of ferromagnetic resonance (Kittel mode [HK51]), will have the dispersion $\omega_\mathrm{K} = \omega_\mathrm{DE}|_{k=0} = \omega_\perp|_{k=0}$. Equations (B.1) and (B.2) together with the Kittel mode, constitute the basic possibilities of magnetic excitations in thin ferromagnetic films. In the following section B.2 a brief example of a continuous film investigated all-optically is given.

## B.2 Samples and experiments

Ferromagnetic thin films made of nickel or cobalt-iron-boron (CoFeB) are produced by electron-beam evaporation or magnetron sputtering [EUM+09]. The magnonic metamaterials' properties cannot be simply derived from the independent properties of continuous film and (periodically arranged) constituents. Instead, effects emerge that are intrinsic to the newly created material, i.e., the observed collective effects themselves define the respective system as being a metamaterial. Consequently, different periodic structures on a continuous film with otherwise identical properties yield different magnonic materials.

In photo-magnonics, all-optical experiments are performed using ultrashort laser pulses to both excite and detect spin-waves. A schematic drawing of the experiment is given in figure B.1(a). It includes the intense optical pump pulses with a central wavelength of 800 nm and a temporal duration of 40 fs. Probe pulses with 5% of the intensity at a variable time delay $\Delta\tau$ yield the electron or magnetization dynamics [DEP+06]. The excitation by the pump pulses takes place within picoseconds, including the ultrafast demagnetization ($\approx$ 100 fs) [ACFW+10] and the relaxation of the highly damped high-$k$ spin-wave modes to longer-lived ones

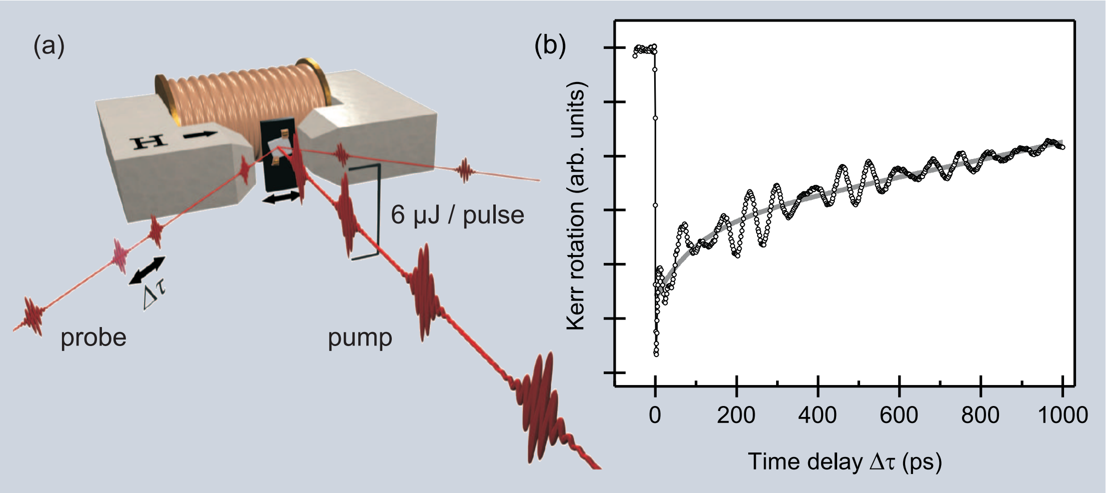

**Figure B.1 – Experiment and reference data.** A schematic of the time-resolved all-optical experiments is given in (a). Pump pulses with a high intensity excite the magnetization dynamics and probe pulses that are time-delayed by $\varDelta\tau$ measure the pump-induced change in the Kerr rotation. A reference data set recorded on a 50 nm CoFeB film at $\mu_0 H_{\mathrm{ext}} = 150\,\mathrm{mT}$ is shown in (b). The solid gray line represents an exponential fit to the background which is subtracted prior to further analysis.

($\approx 20\,\mathrm{ps}$) [DM07]. The respective processes can be experimentally accessed making use of the time-resolved magneto-optical Kerr effect (TRMOKE). Shown in figure B.1(b) are the precessional modes observed with probe pulses that are time-delayed by $\varDelta\tau$ with respect to the pump pulses. The observed modes have frequencies in the GHz range, thus oscillate on timescales up to nanoseconds. In consequence, the non-selectivity in terms of wave vector or frequency of the optical pump can be compared to a delta-like excitation of a classical oscillator which then will swing with its intrinsic eigen-frequency.

### B.2.1 Thin-film magnetization dynamics

The reference data set in figure B.1(b) was recorded on a continuous CoFeB film of thickness $t = 50\,\mathrm{nm}$ for $\mu_0 H_{\mathrm{ext}} = 150\,\mathrm{mT}$. It shows the fast demagnetization [BMDB96] upon absorption of the pump pulse (time delay $\varDelta\tau = 0$) and the subsequent magnetization dynamics which are a superposition of at least two precessional modes [DEP$^+$06]. The particular trace $M(\varDelta\tau)$ from figure B.1(b) is further analyzed in figure B.2(a) by a Fourier transformation. The two modes' frequencies can then be determined. By changing the external field, these frequencies shift and the resulting experimental dispersions $\omega_i(H_{\mathrm{ext}})$ can be fitted by equation (B.2) as seen in figure B.2(b). All data presented in this chapter are plotted in a gray scale, where the (meta)material's response (i.e., the excited spin-wave mode's Fourier power) is indicated by a black peak as a function of externally

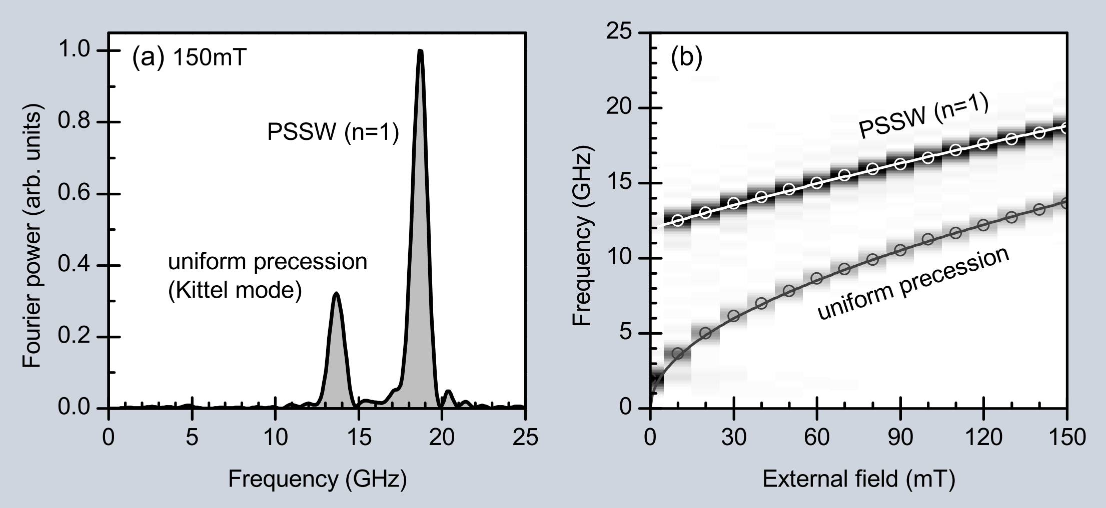

**Figure B.2 – Fourier analysis of the time-resolved magnetization dynamics of a continuous CoFeB film.** In (a) the Fourier spectrum of the single measurement already shown in figure B.1 is displayed ($\mu_0 H_{\mathrm{ext}} = 150\,\mathrm{mT}$). Two precessional modes are observed the frequency of which is dependent on the external magnetic field (b). Circles represent experimentally determined peak positions, the gray and white solid lines are fits of equation (B.2) for the case of $k_\perp = 0$ and $k_\perp \neq 0$, respectively.

applied magnetic field and frequency in Fourier space. The maximum time delay between pump and probe pulses of 1 ns consequently limits the resolution to be $(1\,\mathrm{ns})^{-1} = 1\,\mathrm{GHz}$, in the plots represented by the peak line width.

On the reference film, two modes of precession are observed. These are the uniform Kittel mode (white circles and line) as well as the first order perpendicular standing spin wave (PSSW, gray circles and line). Due to the intriguingly low Gilbert damping in ferromagnetic CoFeB, standing spin waves up to high orders $n \leq 5$ are observed in continuous films. While the spin-wave modes carry information on the structural properties of the film material [LEHM10], we will in the following focus on periodically structured materials.

## B.3 Bloch-like modes in CoFeB antidot lattices

As described earlier, a metamaterial cannot simply be defined by a relation between the wavelengths and the parameters of the imprinted periodic structure. Instead, it is the emerging effects that make the name metamaterial necessary. For example, in a structured CoFeB film a new – magnonic – spin-wave mode is observed [ULM10]. An SEM image of the two-dimensional square lattice of antidots in an otherwise continuous film is included in the inset of figure B.3(b). It depicts the antidot diameter $d$ and the lattice parameter $a$. Compared to the ref-

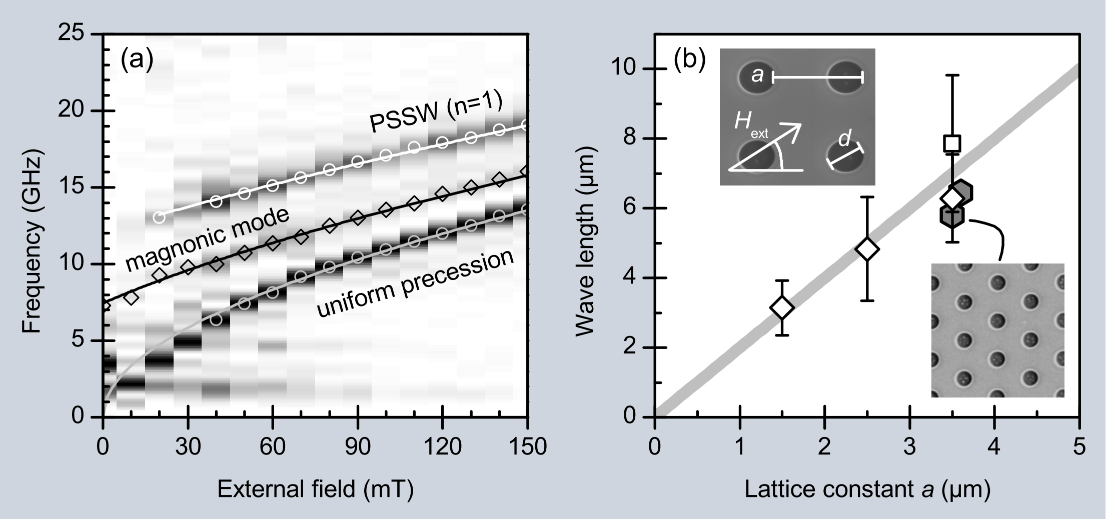

**Figure B.3 – Magnetization dynamics on structured CoFeB films.** The Fourier spectrum in (a) shows an optically excited magnonic mode (black diamonds) additional to the modes also observed on a continuous film (gray and white circles and lines, see figure B.2). The solid black line is a fit of equation (B.1) which yields the magnonic mode's wave vector $k$ further detailed in (b): A change in the antidots' periodicity $a$ shifts the Bloch-like resonance according to $k = \pi/a$ (gray line). Included are points for propagation along different directions with respect to $H_{\text{ext}}$, namely 90° (□) and 45° (◇) in a square lattice, as well as 30° and 60° in a hexagonal lattice (⬡). The insets of (b) show SEM images of a square and hexagonal antidot-lattice unit cell, respectively.

erence data set from figure B.2, the data recorded on a structured film which are plotted in figure B.3(a) reveal another precessional mode not previously observed (black diamonds and line). With the Damon-Eshbach dispersion $\omega_{\mathrm{DE}}(H_{\mathrm{ext}})$ the magnonic character is verified: fitting equation (B.1) to the experimental peak positions yields (as the only fitting parameter) the wave vector to be $k_{\mathrm{DE}} = \pi/a$. From that value and the observed frequency, the spin-wave propagation length can be approximated via the phase velocity: together with the damping time constant determined in the TRMOKE data, one calculates length scales of about 100 µm which equal approximately 30 magnonic unit cells. This leads to an instructive picture on Bloch-mode excitation in real space: the periodic modulation of the spin-wave potential landscape (i.e., the effective internal magnetic field) imposes its periodicity as a condition on the spin waves propagating away from the spot of excitation.

In other words, prerequisites for the observation of spin-wave Bloch states are the low damping in CoFeB and the resulting large propagation length of the spin waves. By changing the periodicity $a$ of the antidot lattice per definition, a new metamaterial is created, in the sense that the magnonic properties are changed. Namely, the DE wave vector can be tuned according to the above-stated relation over a range of $1.5\,\mu\mathrm{m} \leq a \leq 3.5\,\mu\mathrm{m}$. For the measurements in figure B.3(b), the filling fraction $f = \pi d^2/(4a^2) = 12\%$ has been held constant. For small antidot separations, an additional effect comes into play: besides the Bloch-like extended modes, also localized ones are excited. These will be further detailed in section B.5.

### B.3.1 Effects of antidot-lattice symmetry

Included in figure B.3(b) are the experimental results obtained in configurations deviating from $k_{\mathrm{DE}} \perp H_{\mathrm{ext}}$. For example, the antidot lattice can be rotated by 45° around the film normal. In that case, the Damon-Eshbach dispersion (B.1) cannot be fitted to satisfyingly represent the experimentally observed magnonic mode dispersion. This deviation can be accounted for by choosing the angle between propagating surface waves and $H_{\mathrm{ext}}$ to match 45°. The dispersion then reads [KS86]

$$\left(\frac{\omega_{45}}{\gamma\mu_0}\right)^2 = H_x^2 + \frac{H_x M_{\mathrm{S}}}{2}\left[1 + \frac{1}{k_{45}t}\left(1 - e^{-k_{45}t}\right)\right] + \\ + \frac{M_{\mathrm{S}}^2}{2k_{45}t}\left(1 - e^{-k_{45}t}\right)\left[1 - \frac{1}{k_{45}t}\left(1 - e^{-k_{45}t}\right)\right] .$$

Respective fitting results for $k_{45}$ are included in figure B.3(b) as white diamonds. One finds the relation $k_{45} = \pi/a$ to be satisfied. This means that by rotation of the sample the propagation direction of the Bloch-like surface waves is not changed – they still preferably propagate along the nearest-neighbor directions of the antidot lattice.

This remains true for lattices with other than square symmetry. Also in films structured with hexagonal lattices magnonic spin-wave modes are observed. Here, the application of the external field along a high-symmetry axis and assuming a propagation direction in the nearest-neighbor direction (under 30° and 60°, respectively) yields the wave vector $k_{\mathrm{hex}} = \pi/a$. Respective data points are represented in figure B.3(b) by the large filled hexagons.

The population of the magnonic modes suggests the creation of flattened bands that increase the spin-wave density of states (DOS). For spin-waves, the situation is analogous to electrons in a crystal, where a periodic potential is created by the atoms. More precisely, the spin-wave spectrum is modified by the antidots such that band gaps at the Brillouin zone boundary are introduced. Simultaneously, a flattening of bands takes place which in turn leads to an increase of the density of states. Keeping in mind the condensation-like excitation of precessional modes after optical excitation, this increase of the spin-wave DOS can be considered the reason for the observation of the Bloch-like modes. The broad-band excitation by the pump pulses provides the range of spin waves initially necessary to populate the modes discussed here. The close analogy to electronic crystals will be extended in section B.4 where a calculation of the spin-wave spectrum is performed via the plane-wave method.

## B.4 Spin-wave spectra from plane-wave calculations

An analytical approach to theoretically access the creation of band gaps and the flattening of bands is via the plane-wave method (PWM). It has been developed by Puszkarski et al. and can be used to study the appearance of spin-wave band gaps in two-dimensional [VDDRP96], as well as three-dimensional systems [KP08]. For the present case of a thin film with thickness $t = 50\,\mathrm{nm}$ and wavelengths $\lambda$ in the micron range, the assumption $\lambda \gg t$ holds. Thus, the lower modes' profiles can be assumed to be uniform in the $z$-direction, i.e., perpendicular to the thin film. As opposed to the full theory in [KS86], the exchange interaction can then be neglected for sufficiently small $k$ and the uniform-mode analysis applied [HP95]. The respective spin waves are confined in a periodic potential which is constructed by a periodic modulation of the magnetization in terms of a Fourier synthesis:

$$M_{\mathrm{S}}(\boldsymbol{r}) = \sum_{\boldsymbol{G}} M_{\mathrm{S}}(\boldsymbol{G}) e^{i\boldsymbol{G}\boldsymbol{r}} \,,$$

where $\boldsymbol{G}$ is a two-dimensional vector of the reciprocal lattice. Using this formulation, the linearized Landau-Lifshitz-Gilbert equation can be solved. Namely, plane waves of a given wave vector are used to solve the eigenvalue problem stemming from the dynamic field and $M_{\mathrm{S}}(\boldsymbol{r})$ [LUGM11]. The resulting frequency for each mode depends on the position and direction in the reciprocal space of the antidot lattice. This ansatz is similar to the Bloch theorem applied to electrons and photons and yields the magnonic band structure of a periodic ferromagnetic system.

Respective results are plotted in figure B.4. Therein, a calculation for a continuous CoFeB film is compared to a structured film[2]. In the continuous film, the folding of the spin-wave bands at the Brillouin zone boundary is introduced to illustrate the difference when compared to the structured film. For the latter, at the point $X'$ in reciprocal space, a band gap as marked by the dashed ellipsis opens up around a frequency of 15 GHz. This corresponds well to the experimentally

---

[2] continuous means $d \to 0$ while $a = 3.5\,\mu\mathrm{m}$ is held constant

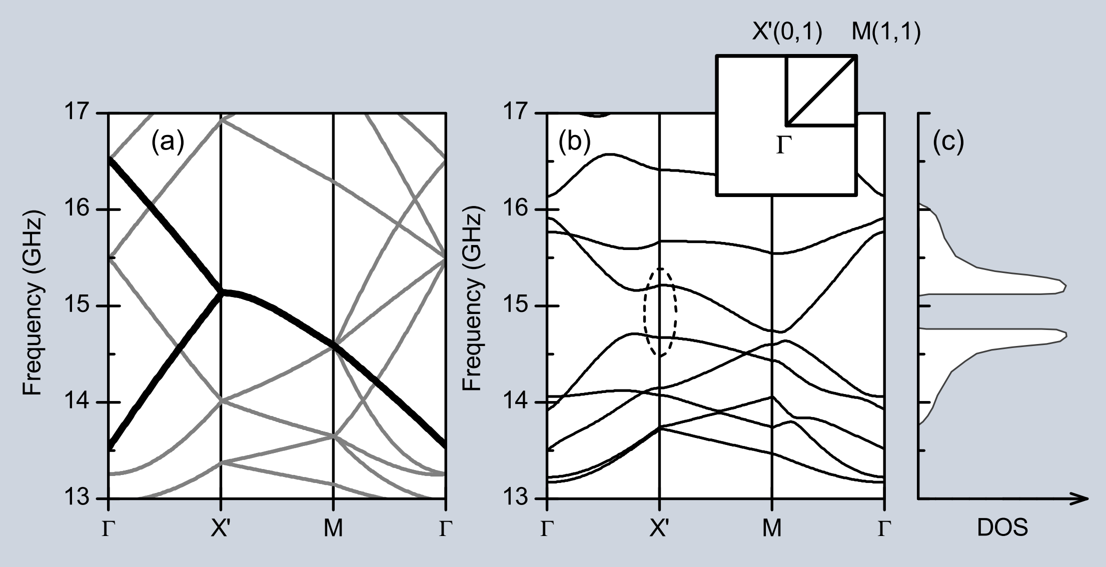

**Figure B.4 – Numerically calculated spin-wave band structures.** Spin-wave band structures of (a) a continuous CoFeB film and (b) an antidot lattice with $a = 3.5\,\mu\text{m}$ and $d = 1\,\mu\text{m}$ in a CoFeB matrix ($\mu_0 H_{\text{ext}} = 130\,\text{mT}$). In (a), the first and second band are marked by the thicker black lines. In (b), the band gap created by the periodic structure is highlighted by the dashed black ellipsis. In the inset, the first Brillouin zone of the square lattice is depicted. The reciprocal directions along $X'$ correspond to $k \perp H_{\text{ext}}$ in real space. Schematically depicted in (c) is the spin-wave density of states (DOS) for the 1st and 2nd band in this direction, which is populated by the laser pump pulses.

observed magnonic mode in figure B.3(b). Hence, there is a close relation between the flattening of the spin-wave band at the zone boundary and the experimental finding of the wave vector being equal to $\pi/a$. The situation is further illustrated in figure B.4(c). Therein, the density of states as a function of the spin-wave frequency is schematically depicted for the 1st and 2nd band in the $\Gamma - X'$ direction. The peaks introduced by the periodic structure correspond to the experimentally observed spin-wave modes.

Details on the calculations and the application to different ferromagnets can be found in [LUGM11]. Concerning size and position of the band gap, tuning is possible by the material parameters of the constituent materials [KP08].

## B.5 Localized modes in nickel antidot lattices

TRMOKE experiments on magnonic crystals with a nickel matrix do not show any Bloch modes as observed in CoFeB in section B.3. Instead, a field-independent mode occurs as shown in figure B.5. Its frequency is independent of $H_{\text{ext}}$ and remains constant up to $\mu_0 H_{\text{ext}} = 150\,\text{mT}$. Moreover, its amplitude is larger than the one of the uniform mode. Only if the external field is large enough, the excitation

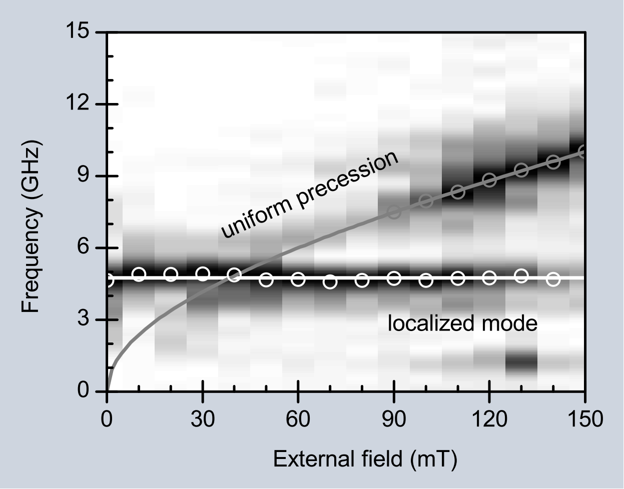

**Figure B.5 – Magnetization dynamics on a structured nickel film with $a = 3.5\,\mu\text{m}$ and $d = 1\,\mu\text{m}$.** The strong intrinsic damping leads to the observation of only a localized magnetic mode (white circles and line). Its amplitude is largest around the antidot edges, and its frequency does not depend on the external field. Only at high $\mu_0 H_{\text{ext}} \geq 130\,\text{mT}$, the uniform precession is excited by the pump pulses (gray circles and line).

efficiency for the Kittel mode is high. This already points to an inhomogeneity of the internal field: If $H_{\text{ext}}$ is sufficiently high, regions of constant internal field exist, where the Kittel mode can be populated. Below the critical field, the internal field undergoes strong spatial changes and localization sites for spin waves are formed [PYC$^+$05]. This is consistent with the experimental finding that the filling fraction $f$ merely changes the amplitude of the localized mode, but does not alter its field-independence.

It has to be considered that the observed effects remain a combination of matrix material and superimposed periodic structure. In ferromagnetic nickel, the intrinsic Gilbert damping is by a factor of 4 larger than in CoFeB. This leads to a strongly decreased propagation length of spin waves, which is not more than 10 µm in nickel (as opposed to 100 µm in CoFeB, see section B.3). Consequently, the spin waves excited by laser pulses do not propagate far enough to largely interact with the periodic structure of antidots. However, also in CoFeB localized modes are observed, if the periodic distortion becomes too strong. For an antidot separation in the order of the internal field inhomogeneity, additional to the propagating magnonic mode a non-dispersive localized mode appears [ULM10].

The frequency of the localized modes can be shifted by virtue of the antidots' separation. This points to a dipolar coupling of individual locations, i.e., regions of strong field inhomogeneity. The same effect can be achieved by rotation of the external field with respect to the antidot lattice. The dipolar coupling between neighboring localization sites changes and hence, the field-independent modes' frequency is shifted, see figure 27 in reference [LUGM11].

## B.6 Outlook: Magnonic control over spin waves

The different effects of a periodic antidot structure in two dimensions have been described. The respective metamaterial(s) illustrate the large potential of artificially structured media in general and magnonics in particular. Namely, they allow the control over spin waves in that the two rivalling effects of localization and Bloch-like extension can be tuned. The selective excitation of magnonic states from a broader continuum of spin waves carries information on the spin-wave density of states. In that respect, the applicability of basic concepts of solid state physics to magnonic crystals has been shown.

Relevant parameters that determine the metamaterials' properties are not only the constituting material, but very importantly the structural parameters of the antidot lattice inside. If, for example, the intrinsic spin-wave propagation length is long enough, information may be carried across multiple unit cells in form of a Bloch-like spin wave. On the other hand, if the intrinsic damping is larger or the filling fraction is too high, localized edge modes are observed that may be used to collect information on the structures' internal field. In combination with other approaches described in the present book, e.g., different material combinations, the perspectives are promising: if taken beyond the proof of principle, spin-wave computation and spin-wave data transmission may be combined to provide a high data throughput and energy efficiency in such devices. One example for a distinct modification of the magnonic periodic structure is a line defect that can function as a wave guide for spin-wave frequencies inside the magnonic gap region, to be functionalized in the future.

**Acknowledgement.** We would like to thank Jakob Walowski for the contribution of the experiment's schematic shown in figure B.1(a) and Georg Herink for careful proof-reading of the manuscript.

## Appendix C

# FIB preparation

In section 3.5 starting on page 51 the structuring of continuous thin films has been briefly described. The present part of the appendix aims to describe the technical details of sample preparation using a beam of focused ions (FIB) which results in structures with fine resolution and near-to-perfect long range order (see for example SEM picture in figure 3.15). The apparatus used was the *xT Nova NanoLab* from *FEI Company* and all information contained in the following are meant to augment the information given in the documentation [Com07].

During the process of ion milling, high-energy $Ga^+$-ions (30 keV @ 0.3 nA throughout this thesis) are focused to a diameter of approximately 20 nm and locally sputter off the film material. In the controlling firmware the definition of arbitrary patterns to be milled is possible via ASCII stream files. An excerpt of an example file is given in listing C.1. Besides the three header lines described in the caption it shows the first and last four pixels of the elliptical dot shown in figure C.2(b). In the figure, the respective pixels are also highlighted.

```
s16
50
617
200 55  60
200 55  65
200 55  70
200 55  75
...
200 145 125
200 145 130
200 145 135
200 145 140
```

**Listing C.1 – Contents of a streamfile.** Truncated streamfile that was used to mill the elliptical dot also shown in figure C.2(b). The first three lines name the number of bits used ($2^{16}$), the number of milling cycles (50) and the total number of addressed pixels (617), respectively. The column preceeding the pixels' $x$- and $y$-coordinates is the dwelltime in units of 0.1 µs (200 in this case). The reader may note that only every fifth pixel is Ga-exposed.

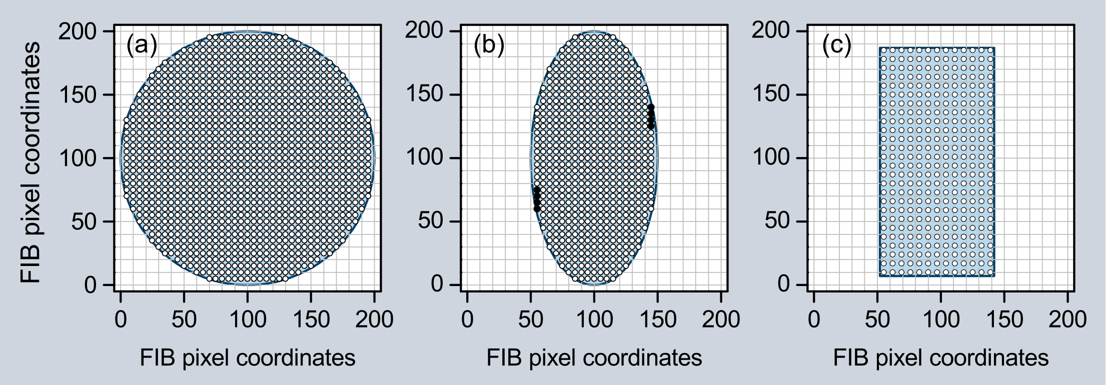

**Figure C.2 – Singular (anti-)dot examples.** (a) Circular antidot with a radius of 90 pixels. Not every technically accessible pixel is unblanked (= exposed to $Ga^+$-beam) to reduce memory usage. (b) Singular elliptical antidot with an aspect ratio of 2 : 1, here defined by 617 pixels. The pixels also given in listing C.1 are shown by filled black dots. (c) Even though not presented in this thesis, squares and rectangular dots may also be defined by the author's software for stream-file creation.

The stream files define the coordinates (pixels), to which the Ga-beam is moved and unblanked in analogy to electron-beam lithography. The firmware can address either a 12- or 16-bit DAC, dividing the field of view in $2^{12} = 4096$ or $2^{16} = 65536$ steps, respectively. By virtue of the instrument's magnification $\Gamma$ the range of pixels is mapped to a distance on the specimen.

According to the instrument's documentation it is recommended not to use the complete range of pixels to prevent "round and jaggy" edges [Com07]. This is achieved by only addressing a fraction $\leq 0.7$ of the $2^{12/16}$ pixels. Together with the overall size of the structured area (typically 150 to 300 µm) the necessary magnification can be calibrated:

$$\Gamma = \text{const} \times \frac{\text{fraction}}{\text{size}} = 1.48 \times 10^5 \times \frac{\text{fraction}}{\text{size (µm)}}. \tag{C.1}$$

This relation holds as of firmware version 3.8.8, while a 5% change in the proportionality constant has been observed after firmware updates. In figure C.3 a few examples of structures are presented. Therein, the red boxes with an edge length of $0.7 \times 2^{16}$ pixels correspond to desired structure sizes of 150 µm, leading to a magnification of $\Gamma = 691$. The lattices have different underlying symmetries which have been investigated in section 3.5.2. These can be square or honeycomb-like, contain additional (line-)defects as introduced in section 3.5.4, or show a wave-guide like appendix as in figure C.3(a).

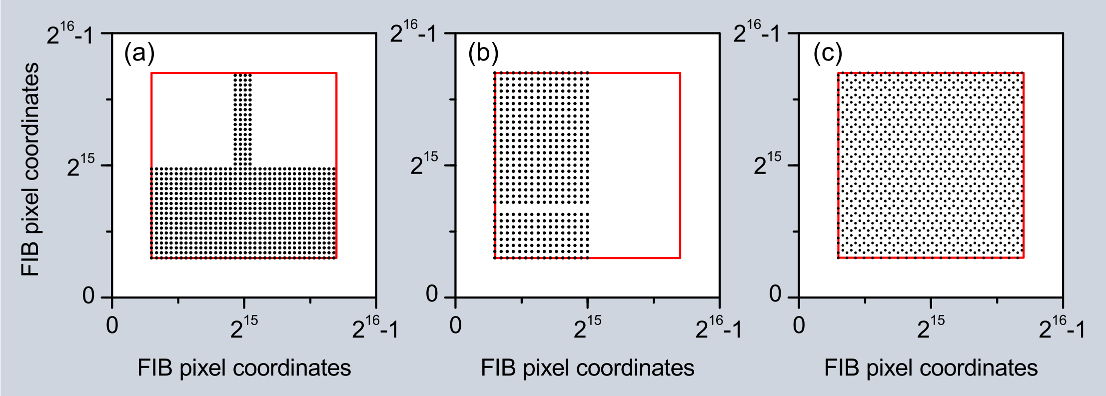

**Figure C.3 – Example lattices.** Overview of different antidot lattices, each composed of single antidots. Red boxes mark the overall structured area, which accounts to 70% of the total range of $2^{16} = 65536$ pixels in $x$- and $y$-direction, respectively. The actual length, to which the pixel coordinates are mapped, is adjusted by the magnification in the controller software (see Eq. (C.1)).

# Software for streamfile creation

Streamfiles for all of the aforementioned lattices and antidots were created with the program shown in figure C.4. It was written in *LabVIEW* and can be obtained from the author or the author's supervisor M. Münzenberg (mmuenze@gwdg.de). In the following, a brief description of parameters is given.

In the top left part of the front panel the singular antidots are defined. This includes the *dot shape* (circular or square), the corresponding size (antidot *diameter* or *height*), as well as the *aspect ratio* to yield elliptical or rectangular shapes, respectively. The lattice, on which the antidots are distributed, is defined in the top center of the front panel. Its *symmetry* may be chosen between several values. Possible values include 'square', 'hexagonal' or 'honeycomb' with periodicities as defined in parameters $P_x$ and $P_y$. The reader may note, that $P_y$ is only relevant for a square lattice, but ignored in all other cases. Additionally, the *lattice symmetry* may be set to 'random', yielding a statistical distribution of antidots without overlap (the total number of antidots is unchanged in comparison to a square lattice). Also, a square lattice rotated by 45° can be created (*lattice symmetry*='square-45'). The bounding box of the structure remains unchanged, thus giving a (1,1)-interface to the unstructured region of the sample. Finally, an externally created lattice may be loaded via the setting 'load file'. The ASCII file to be loaded should then contain the mere lattice points (in the intervals of $x, y \in [0, 2^{12}$ or $2^{16}]$, respectively) to be populated with antidots.

The parameter *size* gives the edge length of the structured area in microns. It is mapped to the total pixel range of the 12- or 16-bit DAC multiplied by *fraction*

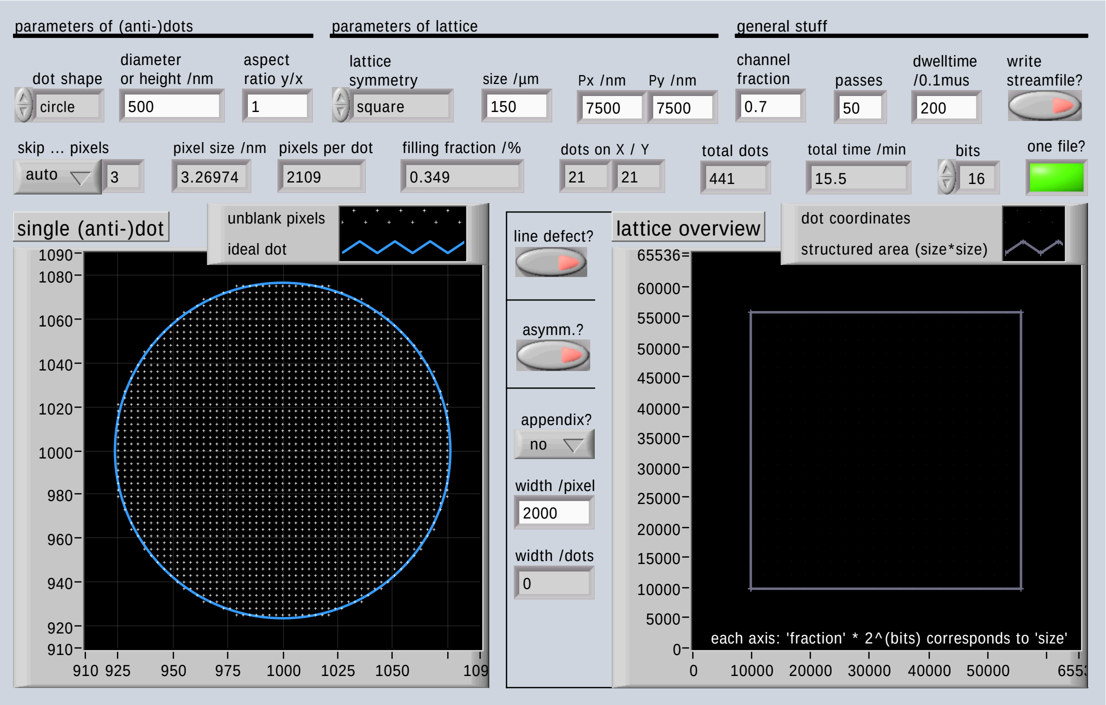

| | |
|---|---|
| parameters of (anti-)dots | |
| dot shape | circle |
| diameter or height /nm | 500 |
| aspect ratio y/x | 1 |
| parameters of lattice | |
| lattice symmetry | square |
| size /µm | 150 |
| Px /nm | 7500 |
| Py /nm | 7500 |
| general stuff | |
| channel fraction | 0.7 |
| passes | 50 |
| dwelltime /0.1mus | 200 |
| write streamfile? | |
| skip ... pixels | auto 3 |
| pixel size /nm | 3.26974 |
| pixels per dot | 2109 |
| filling fraction /% | 0.349 |
| dots on X / Y | 21 21 |
| total dots | 441 |
| total time /min | 15.5 |
| bits | 16 |
| one file? | |
| line defect? | |
| asymm.? | |
| appendix? | no |
| width /pixel | 2000 |
| width /dots | 0 |

**Figure C.4 – Screenshot of LabVIEW program for streamfile creation.** Only the front panel is displayed to give an account of the parameters described in the text.

$\in [0, 1]$ (see above for recommended values for *fraction*). On the front panel's top right the number of *passes* and each pixel's *dwell time* (per *pass*) are defined. The boolean switch *write streamfile?* is 'off' by default to control the resulting antidots and lattice in the respective plots, and is changed to 'on' to actually save a streamfile to disc.

In the second row, a number of control parameters is displayed. Most importantly, not every accessible pixel is Ga-exposed, since the focal size of the ion beam may considerably exceed the single *pixel size*. Hence, the parameter *skip... pixels* has been introduced and is automatically determined by the software by an empirical algorithm (setting 'auto', see also listing C.1 and figure C.2), but may be chosen manually in the dropdown menu. The remaining parameters are mostly self-explanatory, where the *total time* for structuring is calculated via

$$\textit{total time} = \textit{total dots} \times \textit{pixels per dot} \times \textit{dwell time per pixel} \times \textit{passes}.$$

The only parameters remaining are *line defect*, *asymmetry?*, and *appendix?*, respectively. These manipulate the lattice in terms as seen in figure C.3(a) and (b).

# Author contributions

Three publications are compiled in the chapters 2 to 4, and matching the requirements in the doctoral degree regulations [Pru12], the present chapter gives details on the author's contribution to the respective manuscripts,

(2) *Spin-wave population in nickel after femtosecond laser pulse excitation*, Physical Review B **82**, 134443 (2010) [LEHM10],

(3) *The building blocks of magnonics*, Physics Reports **507**, 107 (2011) [LUGM11],

(4) *Spin-wave modes and band structure of rectangular CoFeB antidot lattices*, Journal of Applied Physics **102**, 083921 (2012) [LAPM12].

Furthermore, appendix B reprints an (invited) book chapter which does not contain data additional to the above-listed publications, but gives a condensed overview. Please note that the respective manuscript has not been peer reviewed, as such is not significant for the evaluation of this thesis, and has been included merely for completeness,

(5) *Photo-magnonics*, Magnonics: From Fundamentals to Applications, S. O. Demokritov and A. N. Slavin (eds.), Springer Berlin / Heidelberg (2013) [LGU⁺13].

All of the listed publications present original research by the author. This concerns the sample production as well as the conduction and analysis of the (time-resolved) experiments, while the interpretation of the collected data was also contributed to by the collaborating authors.

In detail, Jaroslav Hamrle performed the scattering cross section calculations for the publication (2), Gerrit Eilers and the author prepared the samples, experiments were performed by the author; an understanding of the observed non-linear mechanisms was developed by Markus Münzenberg and the author; manuscript preparation was carried out by the author.

The numerical band-structures in (3), (4), and (5) were calculated by Henning Ulrichs and Nils Abeling, the relation to all-optical pump-probe experiments was established in conjunction with Markus Münzenberg and the author.

In the review article (3), an overview over the field of *magnonics* is given, with literature references as cited. Manuscript preparation was carried out by Markus Münzenberg and the author, with contributions from all authors. Sample conception and production as well as the measurement and interpretation of the TRMOKE datasets was performed by the author.

The experiments in (4) on rectangular antidot lattices were carried out together with Jelena Panke, manuscripts (4) and (5) were prepared by the author with revisions from Markus Münzenberg.

# Acknowledgements

Without the continuous support and help of so many people, this work could not have been done. Most importantly, this concerns **Prof. Dr. Markus Münzenberg** with his commitment and dedication to physics, paired with the strong confidence in his students. Even more so, his creative thinking and social activities with the research group were a great inspiration.

All fellow and former members of the Münzenberg group have made the past years very productive and fun. Especially this is *Marvin Walter* with whom, besides physics, sailing will always be a perfect vacation (also, without him and his critical proof reading during the past years, this thesis would never have outgone the manuscript status). The close colleagues *Gerrit Eilers*, *Jakob Walowski* and *Vlad Zbarsky* have contributed a lot, may it be the coffee breaks or endless experimental help, explanation, or sample production.

On top of that, the shorter-lived group members like *Henning Ulrichs, Andreas Mann, Fabian Garbs, Jelena Panke, Nils Abeling, Frederik Busse, Johannes Christian Leutenantsmeyer, Martin Lüttich, Niklas Roschewski, Johannes Mendil, Tim Eggebrecht*, and *Maria Mansurova* contributed each in their own fashion, in sum creating an amazing and excellent atmosphere.

This also goes for the whole staff of the I. Institute of Physics, and in particular for *Prof. Dr. Konrad Samwer* who generously gave financial support wherever needed. Not to mention the technical staff around *Hartmut Eichenberg*, realizing ideas with great hands-on manner. In this respect, *Carsten Mahn* takes an outstanding importance, coping with countless small and large requests on a weekly basis – not to forget *Uta Filippich*, never being short of an enlightening smile.

Special thanks shall be devoted to *Georg Herink* for a sensational and unforgettable time in Göttingen. This also goes for *Murat Sivis* and *Björn Hoffmann.* Outside the faculty, *Katrin Reuter* and *Sophie Winkler* had to deal with many setbacks and have made recent life in Göttingen great, funny and inspiring. Finally, without my mother and my brother no such thing as a doctoral thesis, university degree or happiness can be thought of. They are the people that I look up to.